



POLITECNICO
MILANO 1863

SCUOLA DI INGEGNERIA INDUSTRIALE
E DELL'INFORMAZIONE

A Momentum-based Relative Dynamics Model for Hardware-in- the-Loop Simulation of On-Orbit Servicing

TESI DI LAUREA MAGISTRALE IN
MECHANICAL ENGINEERING - INGEGNERIA MECCANICA

Author: **Tommaso Vicariotto**

Student ID: 970243

Advisor: Prof. Francesco Braghin

Co-advisors: Hrishik Mishra (DLR)

Academic Year: 2022-23

Abstract

Due to the increasing amount of debris orbiting the Earth, on-orbit proximity operations have become an increasingly critical research topic. This type of maneuvers generally involves a chaser spacecraft docking with a target, to ultimately perform life-extension or deorbiting operations. As a result, these technological advancements aim to contribute to a more cost-effective and sustainable approach to space missions.

This thesis focuses on the development of a novel control formulation for floating-base robotic systems, such as satellites, which is optimized for the context of on-orbit servicing. Specifically, the proposed dynamics representation allows the control of the motion of multiple systems both synchronously and independently, eliminating the need for acceleration measurements of the bodies. This capability can be effectively exploited to achieve docking in a wide range of configurations. In parallel, the work provides a relative dynamics notation that is utilized to successfully overcome the problem of reduced experimental workspace, intrinsically possessed by the robotic simulators employed during the on-ground testing.

This work was entirely developed at the Robotics and Mechatronics Institute of the German Aerospace Center (DLR). Accordingly, the validation phase was conducted on the On-Orbit Servicing Simulator (OOS-SIM): a cutting-edge Hardware-in-the-Loop (HIL) facility for micro-gravity conditions. Therefore, the outcome of this thesis is a novel concept for on-ground validations, which effectively ensures physical consistency with the real mission scenario. In particular, the HIL simulator replicates only the relative motion between the two spacecraft, while their real total behavior is visualized in real-time through dedicated software.

Keywords: On-orbit servicing, multibody dynamics, hardware-in-the-loop simulation, space robotics, motion control, inertia decoupling

Abstract in lingua italiana

A causa della crescente quantità di detriti orbitanti intorno alla Terra, le operazioni di prossimità in orbita sono diventate un argomento di ricerca sempre più cruciale. Questo tipo di manovre prevede generalmente l'aggancio di un veicolo spaziale con un bersaglio, per eseguire operazioni di estensione della vita o di deorbitamento di quest'ultimo. Di conseguenza, questi progressi tecnologici mirano a contribuire a un approccio più economico e sostenibile alle missioni spaziali.

Questa tesi si incentra sullo sviluppo di una nuova formulazione di controllo per sistemi robotici a base flottante, come i satelliti, ottimizzata per il contesto del servizio in orbita. In particolare, la rappresentazione matematica della dinamica, proposta in questa tesi, consente di controllare il moto di più sistemi sia in modo sincrono che indipendente, eliminando la necessità di misurare l'accelerazione dei corpi. Questa capacità può essere efficacemente sfruttata per ottenere il loro aggancio in un'ampia gamma di configurazioni. Parallelamente, il lavoro fornisce una notazione di dinamica relativa che viene utilizzata per superare con successo il problema del ridotto spazio di lavoro sperimentale, intrinsecamente posseduto dai simulatori robotici impiegati durante i test a terra.

Questo lavoro è stato interamente sviluppato presso l'Istituto di Robotica e Meccatronica del Centro Aerospaziale Tedesco (DLR). Di conseguenza, la fase di validazione è stata condotta sul On-Orbit Servicing Simulator (OOS-SIM): un simulatore Hardware-in-the-Loop (HIL) all'avanguardia di condizioni di microgravità. Quindi, il risultato di questa tesi è un concetto innovativo per le convalide a terra, che assicura la coerenza fisica con lo scenario reale della missione. In particolare, il simulatore HIL replica solo il movimento relativo tra i due veicoli spaziali, mentre il loro comportamento totale è visualizzato in tempo reale attraverso un software di simulazione dedicato.

Parole chiave: Assistenza in orbita, dinamica multicorpo, simulazione hardware-in-the-loop, robotica spaziale, controllo del movimento, disaccoppiamento dell'inerzia

Contents

Abstract	i
Abstract in lingua italiana	ii
Contents	iii
1 Introduction	1
1.1 Motivation	1
1.2 Thesis outline	3
2 State of the Art	5
2.1 On-ground micro-gravity testing	5
2.1.1 Robotic HIL facilities	6
2.1.2 DLR On-Orbit Servicing Simulator	8
2.2 Modeling of satellites dynamics	9
3 Mathematical representation of a simplified on-orbit operation	12
3.1 Fundamentals of rigid body dynamics	12
3.1.1 Implementation of the model	16
3.2 Fundamentals of rigid body control	17
3.3 Stability of the rigid body	18
3.3.1 Stability proof with quaternions	19
3.3.2 Stability proof with a compact formulation	21
3.4 Satellites actuation	23
3.4.1 On-board sensors	23
3.4.2 Actuators for on-orbit motion	24
3.4.3 Proposed model of thrusters	25
3.4.4 Proposed model of reaction wheels	27
3.5 Results of the docking simulation	31

4 Absolute dynamics control of orbital multibody systems	33
4.1 Novel dynamics formulation of an orbital multibody system	33
4.2 Stability of the multibody system	36
4.2.1 Free-floating control	37
4.2.2 Inertia shaping on reaction wheels	38
4.2.3 Free-flying control	41
4.2.4 Hierarchical control	42
4.2.5 Comparison between the proposed control methods	46
5 Relative dynamics control of orbital multibody systems	48
5.1 Introduction to the simulation scenario	48
5.2 Main concept of the proposed dynamics formulation	48
5.3 Novel inertia-decoupled relative dynamics formulation	50
5.4 Stability of the locked and shape systems	53
5.4.1 Coordinated control	55
5.4.2 Comments on the proposed control methods	57
5.5 Formation flying principles	61
6 HIL experimental validation on the OOS-SIM	63
6.1 Validation of the absolute dynamics	63
6.1.1 Set-up of the experiment	63
6.1.2 Experiment development and results	65
6.2 Validation of the relative dynamics	68
6.2.1 Set-up of the experiment and model integration	68
6.2.2 Experiment development and results	70
7 Discussion and conclusion	74
7.1 Main contributions	74
7.2 Future work and research areas	76
Bibliography	78
A Appendix	82
A.1 Stability of linear systems	82
A.2 Stability of non-linear systems	82
A.3 Lyapunov stability through functional analysis	83

A.4	LaSalle's invariance principle	84
A.5	Application of LaSalle	84
A.6	Energy conservation and skew-symmetry proof of $\dot{M} - 2C$	85
	List of Abbreviations	87
	List of Symbols	88
	List of Figures	89
	List of Tables	91
	Acknowledgements	92

1 | Introduction

1.1. Motivation

According to the European Space Agency (ESA), more than 36,000 tracked space debris larger than 10 cm are orbiting the Earth, with an average impact velocity of roughly 10 km/s . Their number then skyrockets to 130 million, considering sizes larger than 1 mm . Particularly, such debris consist of pieces of no longer operating human-made systems, such as satellites, rockets, missiles, and, to a lesser extent, waste discarded by astronauts.

Since the beginning of the space era in 1957, satellites launched into orbit have a finite lifetime due to the thrusters fuel requirement and the lack of servicing abilities. Consequently, once their functionality is over, they are either disposed of through deorbiting to the atmosphere, commanded to precise graveyard orbits, or simply left tumbling indefinitely in space. Specifically, large debris, such as Envisat, whose decommissioning is analyzed in the COMRADE mission [1], are not the only objects that pose a threat to functioning orbital systems. Indeed, given the intense density of small debris floating at high speed, also cosmic bits can cause disastrous consequences upon impact. Hence, the unfortunate vision of a catastrophic chain reaction of mutual collisions is known as the Kessler syndrome [2].

A significant example of the tangible problem of space debris is provided by the current ESA's ClearSpace-1 mission. This project aims at deorbiting a secondary payload adapter, originally part of the Vega rocket, by employing a chaser vehicle equipped with a robotic four-armed claw, depicted in Figure 1.1, by 2026. However, the target was unexpectedly struck by other orbiting objects recently, leading to an increase in the overall debris cloud density.

To tackle the debris urgency, the major entities in the field not only focus on deorbiting missions but collaborate on establishing safe space guidelines and programs of On-Orbit Servicing (OOS) that aim at minimizing their growth. In this regard, current technology enables robotic systems to play a crucial role. In fact, their employment provides



Figure 1.1: ESA ClearSpace-1 robotic mission render (*Credits: ClearSpace*).

significant benefits in terms of costs and crew safety, compared to traditional manned operations [3]. For instance, the hazardous repair and maintenance missions of the Hubble Space Telescope, conducted by astronauts through numerous spacewalks, may be entirely carried out by autonomous robots.

As a result, the development of robotic technology for OOS is becoming increasingly critical. Notably, this class of operations comprises life-extension maneuvers of currently operational spacecraft, such as maintenance, repair, upgrading, and refueling. A mission of this kind is expected from the Italian Space Agency (ASI) through a partnership with Thales Alenia Space by 2026. Furthermore, the European Union has commissioned the project ORU-BOAS (Orbital Replacement Unit - Based on Building Blocks for Advanced Assembly of Space Systems), among which one of the principal partners is DLR. This mission proposes deploying module units capable of docking with each other and with other platforms through standard connection interfaces and moving in a coordinated fashion to perform the operations mentioned above.

To accomplish OOS or deorbiting tasks, floating-base robots as autonomous satellites and module units are equipped with a Guidance Navigation and Control (GN&C) system. Hence, prior to their launch in orbit, such robots and their GN&C units are subjected to rigorous testing phases that possibly ensure their reliability. In this regard, most space companies and agencies rely on HIL simulators that replicate micro-gravity conditions for accurate and cost-effective on-ground testing. In parallel, the Astrobee system, consisting



Figure 1.2: The Astrobee system concept (*Credits: NASA*).

of three cube-shaped free-flying robots denoted as Astrobees and a docking port, serves as a robotic testbed in a real space scenario [4]. In fact, these robots, shown in Figure 1.2, float within the International Space Station (ISS) exploiting the propulsion exerted by electric fans. Thus, they create a set-up that ensures pure zero-gravity (0-g) conditions for refining and validating control algorithms.

Considering the foregoing reasons, the development of effective dynamics representations, coupled with robust relative and coordinated control formulations, and their extensive experimental validation through HIL experiments are a research topic of primary importance and interest in the space robotics community.

1.2. Thesis outline

The thesis is organized as follows. Chapter 1 introduces the motivation behind the research in the field of on-orbit operations. Following, Chapter 2 outlines the current approaches utilized towards the validation of orbital robots. Notably, it analyzes the most acknowledged on-ground simulators and dynamics formulations, eventually leading to the main problem statement addressed in this work.

Chapter 3 first gathers the mathematical basis for describing the dynamics of a rigid body in space and controlling its pose. Following, it defines the choice and use of satellite sensors and actuators for OOS missions., proposing a realistic model of the latter. Moreover, it shows their effectiveness through a simplified docking simulation, where a chaser satellite,

known as the *servicer*, undertakes the task of approaching and docking toward a second satellite, called *client*, which remains stationary in space.

Afterward, Chapter 4 expands the control problem to a multibody scenario. Particularly, a new inertially decoupled dynamics is derived for a system consisting of a spacecraft and its reaction wheels (RWs). The stability analysis of this system is addressed through the development of three different control approaches. Namely, the free-floating control, involving only the actuation of the RWs, and the free-flying, and hierarchical controls, including both RWs and thrusters. Lastly, a comparison of the data obtained from the integration of the proposed control methods in a simulation environment is presented.

Chapter 5 introduces more systems in the definition of the dynamics, tackling the relative control problem. Specifically, it contains a novel relative formulation for two multibodies, based on the creation of two artificial systems, called *locked* and *shape*, representing the total and relative dynamics, respectively. Initially, the concept is explained through a simple example, then developed in its full complexity. The stability problem is once again solved using three different control methods. It additionally includes a discussion on the advantages the proposed formulation holds.

Furthermore, Chapter 6 provides the results obtained from the experimental analysis conducted on the OOS-SIM. Specifically, these experiments allowed to validate the multibody dynamics formulations discussed in the previous chapters and gather relevant data for the conclusion of the work. This chapter starts with the implementation of the absolute multibody dynamics model, tested in its stability and robustness under external forces. Following, it addresses the relative dynamics problem. Thus, it presents in detail the relevance of the proposed work toward HIL simulations.

Finally, Chapter 7 exposes the scientific contributions achieved with this letter. Moreover, it proposes a linear continuation of the work, supporting some research areas in which the developed dynamics and control formulations find application.

2 | State of the Art

2.1. On-ground micro-gravity testing

Considering the challenging conditions and significant costs associated with space operations, space robotic systems are subjected to rigorous on-ground verification and validation phases before their mission deployment. Consequently, over the past decades, various testing facilities have been developed. Flores-Abad et al. explore the principal approaches over a detailed survey [5]. One possibility involves the utilization of water pools to achieve neutral buoyancy, which creates a micro-gravity environment. However, this method introduces unwanted drag forces in the system's dynamics. Moreover, the robotic systems under verification require sealing and waterproof characteristics, which are typically not a space constraint. Thus, such facilities are primarily used for astronaut training. Parabolic flight represents another option for testing robots in a limited workspace and for an extremely brief duration: generally from 10 to 30 seconds. The time constraint of the experiment is even more demanding in the case of free fall, which also possesses some intrinsic hazardous characteristics. Another explored alternative is the implementation of a force compensation mechanism. This balancing is usually achieved with a cables-controlled structure, which, however, reduces the dexterity of the robot, and often introduces extra tension in the dynamics. For instance, an Atwood machine based on two high-tensile wires was employed as a testbed for the Hedgehog robot developed by NASA JPL and Stanford University [6]. This environment resulted particularly suitable for assessing the hopping and tumbling behavior of the robot, designed for autonomous exploration of comets and asteroids.

One of the most widely adopted approaches involves the development of a low-friction flat-floor facility where vehicles float. Generally, these systems achieve free-body motion through the use of air-bearings. This configuration allows for the simulation of a 2D space low-gravity environment. Hence, a considerably large workspace with contact dynamics can be simulated, at the cost of reducing the 0-g degrees of freedom (dof) of the simulated scenario to 1 dof in rotation and 2 dof in translations. Since many agents can be integrated in the environment, this technology is often exploited to test the formation flying of robots.

This concept is evaluated in [7], through the use of a single 6 dof air-cushion based system. However, the proposed HIL facility splits the hardware into two parts, one for translation and the other for rotation, preventing a straightforward combined visual feedback. NASA JPL created a larger facility called Formation Control Testbed (FCT), constituted of two 6 dof air-bearings supported systems, to recreate formation flight and robotic manipulation missions [8]. Moreover, [9] investigated the use of small mobile robots to reach the satellite formation, thus eliminating the need for a frictionless surface through a proper actuation of the rovers.

The flat-floor scenario has also been considered in combination with fixed-base robots. For instance, the ORION facility of the Florida Institute of Technology integrated a cartesian robot with the flat-floor set-up [10]. Similarly, ESA coupled a small robotic arm, mounted on a 33-meter long track, with the ORBIT facility [11]. The latter consists of a pressurized flat floor area that can interact with free-floating platforms. This multiple validation environment is utilized for conducting testing campaigns regarding approach and docking operations, as well as for optimizing descend and landing trajectories.

Considering the limitations that the technologies listed above possess, the most reliable solution for micro-gravity verification and validation of space robots are arguably HIL robotic systems. As a consequence, numerous types of such simulators have been developed. Following, some of the most influential examples are presented.

2.1.1. Robotic HIL facilities

Fully robotic HIL facilities for free-body simulation are typically constituted by fixed-base robotic arms, arranged in a dual configuration. Notably, they represent a class of adaptable, resilient, and reliable simulators that allow the achievement of micro-gravity conditions in all six dof in space. For instance, NASA MSFC developed an automated long-range rendez-vous and capture system (AR&C) [12]. The 30-meter long facility was used to simulate docking operations with a target stabilized in attitude, representing the ISS. Similarly, the U.S. Naval Research Laboratory designed a simulator made of two independent 6 dof robotic arms to test GN&C algorithms and approach phases toward a quasi-static target satellite [13]. Aterward, a testbed comprising a commercial manipulator and a parallel robot platform was built at NASA GSFC, to replicate the robotic capture of a satellite [14]. Another large-scale testing environment for rendez-vous and docking maneuvers is the Loockhed Martin Space Operations Simulation Center (SOSC) [15]. This 60-meter long simulator features two 6 dof robots which can integrate many realistic mock-ups, among which one is constituted by three modules of the ISS.

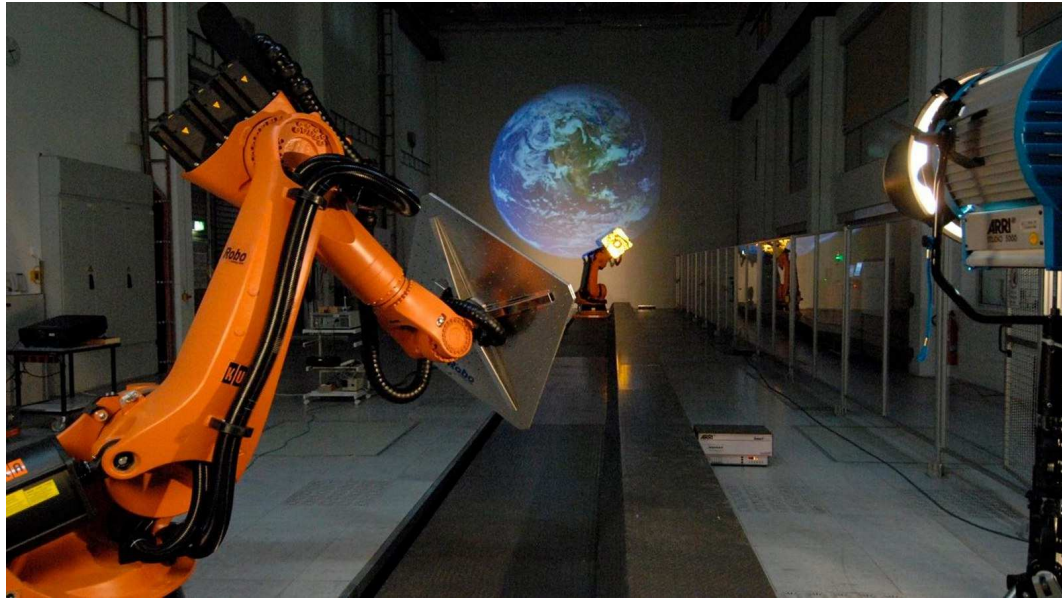


Figure 2.1: EPOS 2.0 robotic facility (*Credits:* DLR).

Experiments of these types are also carried out in more compact facilities, such as those at the University of Luxembourg and at the Stanford University SLAB. The former developed the Zero-G Lab: a lightweight floating platform with two robots, each mounted on a rail [16]. The latter exploits their TRON simulator, composed of two medium-size robots, one of which is mounted on the ceiling and moves along a linear track [17].

DLR's support for on-orbit missions has been consistent since the construction of the first rendez-vous facility, the European Proximity Operations Simulator (EPOS), which was later upgraded to EPOS 2.0, shown in Figure 2.1. The latest version of this facility served as a testbed for the DEOS (Deutsche Orbitale Servicing Mission), aimed at the execution of on-orbit maintenance tasks. In particular, this environment is equipped with two 6 dof robots with a maximum distance of 25 meters. Specifically, the robot representing the chaser satellite can move linearly along a rail toward the second, simulating the target satellite [18]. Particularly, this facility is coupled with the OOS-SIM to create a validation system known as RICADOS (Rendezvous, Inspection, CApturing and Detumbling by Orbital Servicing), that allows to perform full satellite rendezvous-and-docking maneuvers [19].

Specifically, the OOS-SIM represents the facility exploited during the validation and testing phases of the thesis work. Thus, a detailed description is provided in the following section.



Figure 2.2: OOS-SIM robotic facility (*Credits: DLR RMC*).

2.1.2. DLR On-Orbit Servicing Simulator

The OOS-SIM is a state-of-the-art simulator composed of two industrial, position-controlled robots manufactured by KUKA. These two 6 dof robots are equipped with satellite mock-ups positioned at their end-effectors. As depicted in Figure 2.2, the robot on the left replicates the behavior of the so-called servicer satellite and features a light-weight robot mounted in series, a gripper, and a set of cameras and LIDARs, for performing grasping maneuvers. Accordingly, the robot on the right-hand side of the figure generally simulates a tumbling target satellite, denoted as the client.

Thus, the OOS-SIM accurately replicate free-body and contact dynamics through precise gravity compensation and the integration of contact forces, which are measured by the force-torque sensor (FTS) placed on the client's end-effector. Moreover, in contrast to EPOS, OOS-SIM integrates a passivity-based approach that circumvents intrinsic transmission delays and discrete integration effects [20].

These features ultimately enable the testing of momentum-based controls for on-ground simulations of docking and berthing maneuvers [21]-[22]. Particularly, berthing operations comprehend tracking, grasping and stabilization of the client, through manipulation of the servicer. Furthermore, the OOS-SIM can operate autonomously, through telepresence, or in a combined control mode. Thus, an operator can remotely control the robot via a

haptic device, relying on camera images and direct force feedback [23].

2.2. Modeling of satellites dynamics

To faithfully assess the reliability of systems intended for space missions, a model describing their dynamics needs to be integrated and validated in an on-ground facility. In the context of on-orbit operations, the motion of two satellites is generally simulated, primarily replicating their relative dynamics. This is due to the fact that, in most cases, testing absolute dynamics would rapidly saturate the robotic facility’s operational space, preventing the completion of the entire simulation.

A practical example supporting this concept is offered by De Stefano and Mishra, who developed a relative dynamics formulation for testing the mission COMRADE (COntrol and Management of Robotics Active DEbris removal) on the OOS-SIM facility [1]. This mission required testing the grasping of the large debris Envisat, tumbling with a significant angular rate. Specifically, its geometry caused the center of mass (CoM) to be located a few meters away from the initial position of the simulator’s industrial robot. Hence, simulating its absolute spinning would have resulted in substantial rotations of the on-ground robot, which could be handled only for 12 s, before exceeding the robot’s dexterity.

However, deriving a relative dynamics formulation that satisfies the geometric, kinematics, and dynamics scaling properties of such motions involves elevated complexities. Consequently, HIL simulations are frequently conducted following an absolute dynamics approach, or by assuming quasi-static conditions for one of the two systems involved. However, these solutions ultimately reduce the accuracy of the overall validation phase.

In [13], the target spacecraft dynamic was modeled with null velocities, considering only small external disturbances. Instead, the Canadian Space Agency achieves complete on-ground physical consistency in [24] by implementing an impedance controller. Particularly, they were able to match the motion (kinematics) and reaction to external forces (dynamics) of the real-mission satellite with those of the simulation mock-up, scaled in dimensions (geometry). However, the dynamics holds only for a single body and does not tackle the relative formulation problem. The article [25] proposes a relative dynamics for the simulation of on-orbit operations, performed by a dual-arm robot, and collision experiments. Particularly, the motion is replicated by employing the 14 dof robot and a spin motion table. Nevertheless, the representation is based on the difference between the systems states, not accounting for the effects of the Coriolis forces. As a result, the physical consistency of the simulation with respect to a real scenario is not achieved.

The letter [26] developed a relative formulation for replicating the ISS motion and testing long-distance maneuvers. However, the model is integrated over an air-cushion based simulation environment, which has some intrinsic limitations. Specifically, the orbital relative changes computed by the dynamics were reflected through an orientation control of the flat surface. In addition, the proposed formulation needs acceleration measurements for computing the systems' states, remarkably increasing the complexity and verification requirements for the overall space system.

Hence, an advanced relative formulation applied to the HIL environment is presented in the article [1], cited above. Prior to this work, the OOS-SIM robots were commanded in an absolute motion fashion, where the inertial frame coincided with the chaser body frame in its initial configuration [22]. In their letter, they propose to command the hardware robot a relative motion calculated as the difference between a simulated trajectory, which coincides with the motion that the satellite acquires when it is controlled, and a nominal trajectory, i.e. the uncontrolled motion. However, in this novel formulation, the second system is not actively considered in the dynamics computation. Therefore, this derivation holds only in case of small velocities of the second agent. Additionally, the proposed control is accelerations dependent.

Considering single rigid body formations, Lee and Li propose a mathematical representation of the systems that eliminates the need for acceleration measurement in the control design [27]. In particular, they exploit the passive decomposition approach to remove the inertia dependence between the relative dynamics and the single rigid body motions. To this end, a new system that describes the motion of all the agents involved, as a total group, is introduced. Notably, this velocity is computed by considering the sum of their momenta. Consequently, the proposed method allows the synchronization of linear and angular motions among the single agents, while commanding specific relative arrangements within the group. Evidently, this concept finds application in on-orbit maneuvers requiring total and relative motions, such as specific docking configurations, collision avoidance operations, and the coordinated movement of orbital modules.

Indeed, Garofalo et al. in [28] and Mishra et al. in [29] present an application of the locked system definition to floating-base space robots, i.e. spacecraft equipped with a robotic arm mounted on top. Specifically, their main concept was to replace the floating-base velocity with a momentum-based parameter, in order to remove the inertia dependencies between the base and the 6 dof robot. As pointed out by the authors, this approach is particularly effective in a space scenario because the generalized momentum is zero or at least constant along most of the lifetime of orbital operations. Moreover, this condition leads to a beneficial orthogonality relationship between the off-diagonal terms of the multibody

system dynamics matrices. However, in their work, a passive-decomposition-like method is only exploited within a single system representation.

Therefore, the lack of connection between the current formulations of spacecraft formation for HIL experiments, which are primarily focused on absolute dynamics or reduced relative methods with acceleration dependence, and the passive decomposition approach, leads to the problem statement investigated in this thesis.

3 | Mathematical representation of a simplified on-orbit operation

3.1. Fundamentals of rigid body dynamics

Although orbiting satellites are partially made of flexible parts, such as solar panels, antennas, booms, and further extensions, their dynamics can be described conveniently, and with sufficient accuracy, following the model of a six dof rigid body moving freely in space. Thus, by employing Newton-Euler's equations of motion (EoM).

In particular, in the course of the work, the dynamics proposed by Kim in [30] is exploited, which, via a Lie group formulation, couples the Newton equation $f = ma$ and Euler equation $\tau = \dot{h}$, for the description of translational and rotational motion respectively, in a single set of equation. As described by the same authors, the main benefit of this formulation can be identified when it is required to solve the dynamics of articulated rigid body systems, such as robots. In fact, deriving the EoM of such systems would require extreme complexity if done separately for translational and rotational motions. Therefore, it is important to introduce the main quantities used for this purpose.

In order for a body to be described in space, a notation that defines its position and ori-

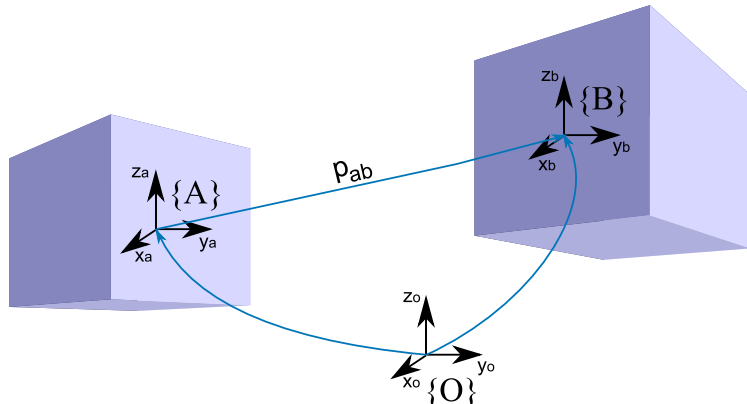


Figure 3.1: Transformation of a rigid body's velocity in different reference frames.

entation with respect to a reference point is required. Considering $\{B\}$ as the coordinate frame of the body, and $\{A\}$ as the arbitrary reference frame, the position of the rigid body is defined by the position vector $p_{ab} \in \mathbb{R}^3$. Similarly, its orientation is described by the 3×3 rotation matrix R_{ab} , denoted by the Special Orthogonal group in three dimensions $SO(3)$, and that satisfies the following properties of orthogonality and unitary constraint:

$$RR^T = R^T R = I$$

$$\det R = 1.$$

Therefore, the full configuration is represented with the pair (R, p) , denoted as the Lie group of the Special Euclidean group in three dimensions $SE(3)$, representing a vector's group of simultaneous rotations and translations, relative to an inertial frame. Hence, their possible parametrization is described by the homogeneous representation of $g = (R, p)$:

$$g = \begin{bmatrix} R & p \\ 0 & 1 \end{bmatrix} \quad (3.1)$$

such that:

$$g^{-1} = \begin{bmatrix} R^T & -R^T p \\ 0 & 1 \end{bmatrix}.$$

Moreover, in order to exploit the dynamics proposed in [30], it is important to introduce the concept of Lie algebra of $SE(3)$, represented by the generalized velocity vector $V = (\mathbf{v}, \boldsymbol{\omega}) \in se(3)$, containing the linear velocity \mathbf{v} , and the angular velocity $\boldsymbol{\omega} \in so(3)$, where $so(3)$ is the Lie algebra of $SO(3)$. Similarly, the generalized velocity can be expressed as a 4×4 matrix, through the following isomorphism:

$$V = g^{-1} \dot{g} = \begin{bmatrix} [\boldsymbol{\omega}]_x & \mathbf{v} \\ 0 & 0 \end{bmatrix} \quad (3.2)$$

where the $[.]_x$ operator defines a skew-symmetric matrix, such that:

$$[\boldsymbol{\omega}]_x = \begin{bmatrix} 0 & -\omega_3 & \omega_2 \\ \omega_3 & 0 & -\omega_1 \\ -\omega_2 & \omega_1 & 0 \end{bmatrix} \in \mathbb{R}^{3 \times 3}.$$

Hence, the singular velocities are expressed in the body coordinate frame as

$$\begin{cases} \mathbf{v} = R^T \dot{p} \\ \boldsymbol{\omega} = R^T \dot{R}. \end{cases}$$

Secondly, the analysis includes the derivation of the Euler's equation. The angular momentum of a mass m can be written as

$$\delta h = p \times (\delta m \cdot v)$$

Consequently, the derivation of the previous equation leads to a comprehensive formulation for the angular momentum of a rigid body:

$$h = \int_{vol} (p \times v) \delta m.$$

More in particular, in the case where the body is rotating around its CoM, the linear velocity becomes:

$$v = \omega \times p$$

Thus, the integration performed over the volume of the body is only a function of its mass distribution, leading to the compact definition:

$$h = I_\omega \omega$$

where I_ω is the inertia matrix, representing the inertia tensor in each axis of the rigid body:

$$I_\omega = \begin{bmatrix} I_x & -I_{xy} & -I_{xz} \\ -I_{xy} & I_y & -I_{yz} \\ -I_{xz} & -I_{yz} & I_z \end{bmatrix}.$$

Specifically, for every rigid body there always exists a reference frame, defined by three axes passing through the CoM of the body and called principal axes of inertia, such that the inertia matrix is diagonal. Thus, when the body is aligned with its principal axes, the eigenvalues of the inertia matrix are the principal moments of inertia (I_x, I_y, I_z). This implies that the moment of inertia is not transferred to other axes outside the principal axes of inertia.

Furthermore, through the concept of the inertia matrix of a rigid body, it is possible to define the generalized inertia, describing the body mass value and its distribution with respect to the body frame. Particularly, the kinetic energy of a rigid body is observed in its general form as

$$e = \int_{vol} \frac{1}{2} ||v||^2 \delta m.$$

This can be rewritten as an explicit function of the generalized inertia M , in the form:

$$e = \frac{1}{2}V^T MV.$$

Normally, the generalized inertia is expressed in the body frame, assuming the following form:

$$M = \begin{bmatrix} m & \int_{vol}[r]\delta m \\ \int_{vol}[r]^T\delta m & \int_{vol}[r]^T[r]\delta m \end{bmatrix}$$

where $r \in \mathbb{R}^3$ describes the position of a body point with respect to its body frame. This matrix can be rewritten as

$$M = \begin{bmatrix} m & m[p] \\ m[p]^T & RI_c R^T + m[p]^T[p] \end{bmatrix}$$

where I_c represents the inertia of the body at its CoM. Therefore, the generalized momentum $H \in dse(3)$ assumes the form:

$$H = MV.$$

Finally, the Newton-Euler's EoM is expressed as

$$F = \frac{d}{dt}H$$

being $F \in dse(3)$ the vector containing forces and torques acting on the rigid body. Hence, the derivation of the previous equation is conducted by exploiting the lemma of Lie group algebra quantities, presented in [30], stating:

$$\frac{d}{dt}Y = \dot{Y} - ad_v^*Y.$$

Specifically, the adjoint operator of a generalized velocity $V \in se(3)$, or small adjoint, is defined as following:

$$ad_v = \begin{bmatrix} [\omega]_x & [\mathbf{v}]_x \\ 0 & [\omega]_x \end{bmatrix} \quad (3.3)$$

being $ad_v^* = ad_v^T$ the small coadjoint, such that:

$$\begin{cases} ad_v : se(3) \rightarrow se(3) \\ ad_v^* : dse(3) \rightarrow dse(3). \end{cases}$$

Moreover, the small adjoint can be expressed as

$$ad_{v_{ab}} = Ad_{g_{ab}}^{-1} \frac{d}{dt} Ad_{g_{ab}} \quad (3.4)$$

where the adjoint action Ad_g of a transformation matrix $g \in SE(3)$ defined in (3.1), or big adjoint, is an operator that allows the simultaneous change of reference frame for both the linear and angular part of a velocity $V \in se(3)$. Whereas the big coadjoint $Ad_g^* = Ad_g^T$ performs the same linear transformation on a force $F \in dse(3)$. Such that,

$$\begin{cases} Ad_g : se(3) \rightarrow se(3) \\ Ad_g^* : dse(3) \rightarrow dse(3). \end{cases}$$

Particularly, the big adjoint is defined as

$$Ad_{g_{ab}} = Ad_{g_a}^{-1} Ad_{g_b} = \begin{bmatrix} R_{ab} & [p_{ab}]_x R_{ab} \\ 0 & R_{ab} \end{bmatrix}. \quad (3.5)$$

Therefore, by substituting the value $Y \in dse(3)$ with the generalized momentum L , the final form of the rigid body dynamics is obtained:

$$F = M\dot{V} - ad_v^* MV. \quad (3.6)$$

The current formulation of the rigid body's EoM offers also the benefit of being coordinate invariant, allowing to derive the dynamics with respect to a reference frame at will. Indeed, being $\{A\}$ and $\{B\}$ two different coordinate frames, both the following equations hold, and truthfully describe the dynamics of the system:

$$\begin{cases} F_a = M_a \dot{V}_a - ad_{v_a}^* M_a V_a \\ F_b = M_b \dot{V}_b - ad_{v_b}^* M_b V_b. \end{cases}$$

3.1.1. Implementation of the model

The model defining the dynamics of the servicer satellite is implemented in Matlab/Simulink, by following the equations presented in the previous section. In particular, its correct implementation is verified through the conservation of the generalized momentum in the inertial frame and of the kinetic energy, under the absence of external forces and torques. Figure 3.2 shows the relevant parameters remaining constant throughout the given simulation time, thus validating the integrated dynamics.

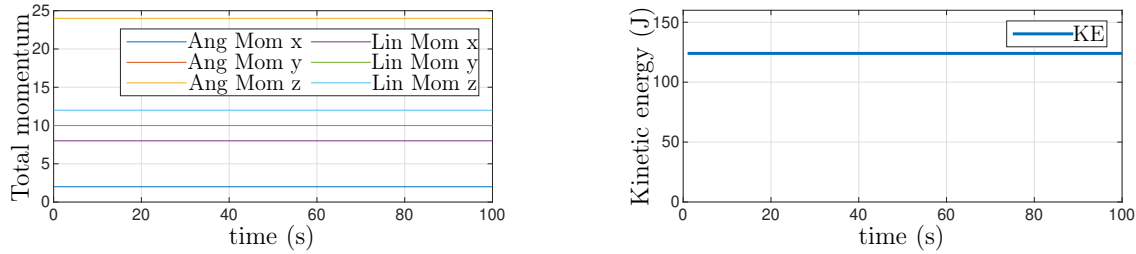


Figure 3.2: Conservation of the momentum in the inertial frame (left) and of the kinetic energy (right), over time.

3.2. Fundamentals of rigid body control

The problem of an actuated satellite performing a correct and stable docking to a second satellite stationary in space necessarily requires a tracking controller for the first system. In particular, the controller needs to be defined in the group of rotations $SO(3)$ and in the group of rigid motions $SE(3)$. To this end, the formulation presented by Bullo and Murray in [31] is exploited. Isolating the translational motion of the rigid body, a proportional derivative (PD) controller is designed as

$$\begin{aligned} u_f &= -K_p \Delta x - K_d \Delta \dot{x} \\ &= -K_p \Delta x - K_d R \mathbf{v}_b \end{aligned} \tag{3.7}$$

where Δx defines the difference between the actual and desired position in the three coordinates, R is the rotation matrix to change the frame with which the linear velocity is being considered: from body-fixed to inertial frame, and K_p, K_d are the proportional and derivative gains, respectively. Thus, u_f represents the force required by the system to achieve the desired position in space.

Focusing on the rotational control, the evolution in time of the rotation matrix is expressed through the following kinematic equation:

$$\dot{R} = R \boldsymbol{\omega}_b$$

where $\boldsymbol{\omega}_b$ is the angular velocity of the body, expressed in the body frame. Hence, the energy function is computed directly using the rotation matrix, to ultimately ensure the control of the satellite rotation. In particular, the error value is expressed as

$$R_e = R_d^T R$$

where R_d represents the desired rotation matrix, which, for the docking maneuver, is set

to identity. Moreover, considering a fixed reference in space, the derivative of the error is:

$$\dot{R}_e = \dot{R} - (\dot{R}R_d^T)\dot{R}_d = \dot{R}.$$

Similarly, the error functions can be expressed in terms of the angular velocity, specifically as

$$\begin{cases} \omega_e = \omega_b - R_e^T \omega_d = \omega_b \\ \dot{\omega}_e = R \cdot [\omega_e]_x \end{cases}$$

where ω_d represents the desired angular velocity, which, for the current scenario, is null. Therefore, an energy function useful to assess the system's stability is formulated as follows:

$$\Phi(R_e) = \frac{1}{2} \text{tr}(K_p(I_3 - R_e))$$

where ϕ is a scalar potential that gets a space of rotation matrices as input and returns a scalar positive quantity, $\Phi : SO(3) \rightarrow R_+$. Hence, the energy time derivative is

$$\begin{aligned} \frac{d}{dt} \Phi &= \frac{1}{2} \text{tr}(K_p(-\dot{R}_e)) \\ &= \underbrace{(\text{skew}(K_p R_e)^\vee)^T}_{\text{torque}} \cdot \omega_b \end{aligned} \tag{3.8}$$

being $\text{tr}(\cdot)$ the trace operator, $\text{skew}(\cdot)$ a function such that $\text{skew}(A) = \frac{1}{2}(A - A^T)$, and \cdot^\vee an operator that returns a 3×1 vector from a 3×3 matrix, $\cdot^\vee : \mathbb{R}^3 \rightarrow SO(3)$.

It is important to notice that the equation (3.8) highlights part of the amount of torque necessary to control the object in the desired way. Indeed, the time derivative of an energy function is a power function, constituted by the product between a force and a velocity term. Thus, the plant's subsystem needs the calculated torque as an input and gives the instantaneous value of the rotation matrix as an output, which is then used to close the control loop. In particular, the system's torque input u_t is regulated by the controller as:

$$u_t = -(\text{skew}(K_p R_e)^\vee)^T - K_d \omega_b. \tag{3.9}$$

3.3. Stability of the rigid body

To assess the stability of the non-linear system constituted by the servicer satellite, the Lyapunov direct method, extensively explained in Appendix A.2, is exploited. According to this concept, the system is said to be stable in the sense of Lyapunov when the solutions of the system that start at a finite distance from the equilibrium, remain sufficiently close

to it forever. Moreover, the system is considered asymptotically stable if it is stable in the sense of Lyapunov, and its solutions that belong to the equilibrium point's basin of attraction converge to the equilibrium, for a time that tends to infinite.

3.3.1. Stability proof with quaternions

Most of the literature concerning the attitude stability of a spatial system of the type developed in this chapter uses quaternions to define the Lyapunov candidate function. Consequently, although the control is developed with a different notation, it is worth presenting the concept of quaternions.

In fact, such quantities can be used to describe the attitude, i.e. the orientation behaviour along the course of imposed rotations, of a rigid body. Precisely, quaternion multiplication provides a precise means to define misalignment errors comprehensively. For instance, the attitude error of a body with respect to a desired reference can be expressed through the quaternion error vector $q_e = [q_0 \ q_1 \ q_2 \ q_3]^T$, which clearly represents the quaternion related to the rotation that brings the body in question to the desired orientation. Furthermore, their evolution is expressed as

$$\dot{q}_0 = -\frac{1}{2}\boldsymbol{\omega}_x \cdot \mathbf{q} \quad (3.10)$$

$$\dot{\mathbf{q}} = \frac{1}{2}(q_o\boldsymbol{\omega}_x - \boldsymbol{\omega} \times \mathbf{q}) \quad (3.11)$$

that, in the full matrix form, can be written in the following way:

$$\begin{bmatrix} \dot{q}_0 \\ \dot{q}_1 \\ \dot{q}_2 \\ \dot{q}_3 \end{bmatrix} = \frac{1}{2} \begin{bmatrix} 0 & -\omega_1 & -\omega_2 & -\omega_3 \\ \omega_1 & 0 & \omega_3 & -\omega_2 \\ \omega_2 & -\omega_3 & 0 & \omega_1 \\ \omega_3 & \omega_2 & -\omega_1 & 0 \end{bmatrix} \begin{bmatrix} q_0 \\ q_1 \\ q_2 \\ q_3 \end{bmatrix}.$$

Whereas, the unitary constraint that the quaternions' four independent parameters are subject to is the following:

$$q_0^2 + \mathbf{q} \cdot \mathbf{q} = 1.$$

Subsequently, it is necessary to reintroduce the Eulero-Lagrange formulation, previously discussed in equation (3.6), describing the dynamics of the satellite. However, here the focus is on the attitude of the satellite, therefore, the terms related to the linear velocity are discarded. Hence, the dynamics assumes the form:

$$\boldsymbol{\tau}_b = I\dot{\boldsymbol{\omega}} + \boldsymbol{\omega} \times (I\boldsymbol{\omega})$$

being τ_b the time derivative of the angular momentum of the spacecraft. Thus, it is possible to express a positive definite Lyapunov candidate function as

$$W = \frac{1}{2}\omega^T I\omega + kq^T q$$

where k is an arbitrary positive value and q the rigid body quaternion. Therefore, the derivative of the proposed Lyapunov function is:

$$\dot{W} = \omega^T I\dot{\omega} + 2kq^T \dot{q} \quad (3.12)$$

At this point, introducing the equations defining the quaternions evolution (3.10) and (3.11), into (3.12), the Lyapunov derivative is rewritten as

$$\begin{aligned} \dot{W} &= \omega^T [\tau_b - \omega \times (I\omega)] + kq^T (q_0\omega - \omega \times q) \\ &= \omega^T (\tau_b + kq_0 q) \end{aligned}$$

thanks to the presence of the skew-symmetric ω function, defined by the cross-product operator, that allows to discard two terms.

Therefore, the control torque is chosen as

$$\tau_b = -kq_0 q - K_d \omega$$

in a similar way to what is proposed for the control in section 3.3. In fact, by selecting a positive definite gain K_d , the Lyapunov candidate derivative:

$$\dot{W} = -\omega^T K_d \omega$$

is negative definite, for every condition of ω . Moreover, a Lyapunov derivative equal to zero is achieved only for a null value of ω , i.e. when the reference attitude is matched. Therefore, the control law ensures the asymptotic stability of the system. Finally, a similar analysis can be performed directly including the quaternion error vector in the Lyapunov candidate, expressed as:

$$W = \frac{1}{2}\omega^T I\omega + kq_e^T q_e$$

followed by a similar formulation of the feedback law:

$$\tau_b = -kq_e - K_d \omega.$$

3.3.2. Stability proof with a compact formulation

Afterward, following the notation utilized for describing the system dynamics and control law, a different formulation for the Lyapunov candidate is chosen. In particular, this function is proposed as the total energy of the system, i.e. the sum of its kinetic and potential energies, expressed in the following way:

$$W = \underbrace{\frac{1}{2}\mathbf{v}_b^T m\mathbf{v}_b + \frac{1}{2}\omega_b^T I\omega_b}_{Kinetic\ energy} + \underbrace{\frac{1}{2}\Delta x^T K_p \Delta x + \frac{1}{2}tr(K_p(I_3 - R_e))}_{Potential\ energy}.$$

Specifically, it is a positive definite function, and its derivative assumes the following form:

$$\begin{aligned} \dot{W} &= m\mathbf{v}_b^T \dot{\mathbf{v}}_b + I\omega_b^T \dot{\omega}_b + \Delta x^T K_p(R\mathbf{v}_b) + (skew(K_p R_e)^\vee)^T \omega_b \\ &= V^T[m\dot{\mathbf{v}}_b + I\dot{\omega}_b + R^T K_p \Delta x + skew(K_p R_e)^\vee] \\ &= V^T[F + ad_v^T M V] + V^T[R^T K_p \Delta x + skew(K_p R_e)^\vee] \\ &= -V^T K_d V + V^T(ad_v^T M)V \end{aligned} \quad (3.13)$$

which is obtained by integrating the general equation of the satellite dynamics (3.6) in the Lyapunov function. Thus, by introducing the force-torque input F , that couples equations (3.7) and (3.9) in a six-dimensional vector.

As explained in Appendix A.3, the system is stable in the sense of Lyapunov if and only if its Lyapunov candidate function is lower and upper bounded, positive definite, and its derivative is negative semi-definite. For the proposed system, all three conditions hold: the first two are trivial, while the skew-symmetry of the matrix $\dot{M} - 2C$, demonstrated as a general condition in Appendix A.6, ensures the non-positivity of the derivative of the Lyapunov function. This property is demonstrated for the rigid body system as follows.

The inertia matrix M , computed with respect to the frame attached to the CoM of the body, comprises only constant values. As a result, its derivative is null. Thus, the problem can be reduced to the prove of the skew-symmetry of the centrifugal/Coriolis (CC) matrix C only. However, such property is not evident in its standard form, derived from the proposed dynamics formulation. Specifically, C is observed as

$$C(V) = ad_v^T \cdot M = \begin{bmatrix} [\omega]_x & [\mathbf{v}]_x \\ 0 & [\omega]_x \end{bmatrix} \begin{bmatrix} m & 0 \\ 0 & I \end{bmatrix}. \quad (3.14)$$

Consequently, this matrix needs to be rewritten in a different notation, which highlights its skew-symmetry structure. This can be achieved by multiplying the current matrix C

by the generalized velocity V and by subsequently exploiting the cross-product property of vectors: $a \times b = -b \times a$. Furthermore, by recalling that the transpose of a skew-symmetric matrix is equal to its opposite, it is finally possible to express the CC matrix in a different form, called \tilde{C} , which is mathematically equal to the form expressed in equation (3.14). This is performed as follows.

$$C(V) \cdot V = \begin{bmatrix} [\omega]_x m & [v]_x I \\ 0 & [\omega]_x I \end{bmatrix} \begin{bmatrix} v \\ \omega \end{bmatrix} = \begin{bmatrix} [I\omega]_x^T & [mv]_x^T \\ 0 & [I\omega]_x^T \end{bmatrix} \begin{bmatrix} v \\ \omega \end{bmatrix} = \tilde{C}(V) \cdot V.$$

As it can be noted, the matrix \tilde{C} is entirely composed of skew-symmetric matrices, thereby making it a skew-symmetric matrix itself.

Notably, the triple product between a vector, a skew-symmetrix matrix and the same vector in its transposed form returns zero. As a result, the Lyapunov derivative observed in equation (3.13) is rewritten as

$$\dot{W} = -V^T K_d V \quad (3.15)$$

where K_d is a positive constant. Hence, the non-positivity of the Lyapunov derivative is demonstrated and it is safe to assert that the system achieves uniform stability. Particularly, this condition resembles Lyapunov stability, except for the fact that the system's rate of reduction toward the equilibrium position does not depend on the initial state t_0 anymore.

Moreover, in accordance with LaSalle's invariance principle, the system is asymptotically stable if and only if the subset where the Lyapunov derivative is null consists of the equilibrium point only, as discussed in Appendix A.4. In the proposed scenario, it can be noted that the Lyapunov derivative, shown in equation (3.15), assumes zero values ($\dot{W} = 0$) only when the generalized velocity vector is null. That is when the equilibrium on both position and orientation is achieved. Accordingly, in the context under consideration, the reference satellite remains stationary in space, causing the chaser satellite to stop its motion only when both translational and rotational errors reach zero. As a consequence, the condition required by the LaSalle's invariance principle is met. The asymptotic stability of the floating rigid body system through the Lyapunov direct method is so demonstrated.

3.4. Satellites actuation

In order to actively stabilize the satellite in the presence of external disturbances and allow for autonomous maneuvers, such as docking or changes of orbit, the satellite must be equipped with a suitable Attitude Determination and Control System (ADCS), consisting of a set of sensors and actuators. The former provide the on-board computer with the necessary information on the current pose of the satellite, and the latter enable its precise motion. In particular, the actuation accuracy of the satellite greatly depends on the measurement errors, and is generally achieved through two types of mechanical systems: the thrusters and the RWs. These systems are directly implemented in the spacecraft, making it a multibody system. It should be noted that thrusters can be used for both position and attitude control, while RWs only control the orientation of the orbiting satellite. As a result, the thrusters primarily engage in translation control, while their contribution in the spacecraft attitude stabilization, relies upon the selected control strategy, resulting from the mission constraints.

Within this section, there follows an overview of the sensors and actuators generally integrated into a mission scenario. Moreover, a realistic model of actuators is proposed and tested in a docking simulation environment.

3.4.1. On-board sensors

The type of pose sensors integrated on a satellite mainly depends on the purpose of the mission, on the orbiting bodies characteristics, thus, on the required pointing accuracy. In fact, many constraints, such as mass, power, volume, lifetime and cost, must be taken into account during their design phase. This aims at eventually ensuring the optimization of their performance.

Specifically, sensors can be divided into two main categories:

- Reference sensors: they rely on the position of the Sun, a planet, or stars, to provide a measurement value that defines the satellite's position and orientation in space.
- Inertial sensors: they provide a continuous measure of the satellite attitude.

Since the inertial measurements contain errors, these types of sensors require a systematic calibration procedure, which can be performed by exploiting the reference sensors.

In particular, the most common reference sensors in the satellite domain are:

- Sun Sensors: they are able to detect the line-of-sight of the Sun as a reference,

exploiting its brightness. Their main disadvantage is that the Sun is sometimes obscured by the Earth's shadow, especially in Low Earth Orbit (LEO) orbits. These types of sensors are divided into the Sun presence detector, the analog Sun sensor, and the digital Sun sensor.

- Star trackers: the position of a known set of stars, measured through star cameras, is constantly compared to a reference catalogue, which allows the identification of the satellite's attitude. They represent the most complex and provide the best accuracy in satellite attitude measurements. As a drawback, a significant memory and process capability is required.
- Earth/Horizon Sensors: they scan the sky through an optical system detector and sense the Earth's horizon, to determine the relative attitude of the satellite. This is possible thanks to the change in the measurement of the infrared radiation emitted by the Earth. Indeed, any radiation source coming from the Earth could be used for this scope, but the IR provides a more uniform energy signal, thanks to its range of wavelengths.

Whereas, the main inertial sensors comprehend:

- Magnometers: they are an extremely simple, robust, lightweight and low-cost type of sensor. For these reasons, they are among the most popular in the LEO satellites market. Specifically, they can map the spacecraft by measuring changes in the strength and direction of the local magnetic field, relative to a reference model of the Earth's magnetic field. They require coupling with reference sensors due to magnetic field anomalies and noise.
- Spinning gyroscopes: they measure the rate of their rotating support. A configuration of three orthogonal gyros can determine the rotational rate of the frame to which they are attached, hence of the satellite. By integrating this signal and coupling it with a reference attitude measurement, it is possible to update the latter at each instant. The classical configuration is called an inertial reference unit (IRU), and includes four gyros, where one is for redundancy reasons. Instead, when combined with accelerometers, the configuration is called inertial measurement unit (IMU), and it allows for additional information on the position and velocity.

3.4.2. Actuators for on-orbit motion

Spacecraft control actuators can be based on different physical principles. The choice of the type of actuator installed on-board the satellite greatly affects its configuration, the

resulting pointing accuracy, and even the implementation of the control laws themselves.

The control action can be delivered to the satellite in three main ways:

1. Producing a direct torque with thrusters;
2. Applying the torque via a magnetic field;
3. Exchanging angular momentum between rotating parts and the spacecraft itself.

Hence, the actuators types can be divided into inertial, which generate a torque action through a change in their angular momentum, and non-inertial, in which the rotation is not present, or is not a key aspect.

Specifically, as outlined in [32], the main inertial actuators employed in space missions are

- Momentum/Reaction wheels: they store rotational energy and exchange angular momentum with the satellite, exploiting the conservation of angular momentum for stabilizing the system or adjusting its orientation. They are typically referred to as momentum wheels when operated at nearly fixed high speeds, serving stabilization purposes and allowing variation to generate extra torque. In contrast, they are denoted as RWs when nominally set at rest and allow a wide speed range and bidirectional movement, providing more versatility in the control of the satellite's orientation.
- Control moment gyroscopes: they consist of a momentum wheel gimbaled in one or two axes, also defined as double-gimbal bias-momentum wheels.

Whereas, the non-inertial include

- Magnetic torquers: they generate a magnetic dipole moment, thus a torque, proportional to the Earth's magnetic field sensed aboard. They are constituted by magnetic coils or electromagnets.
- Thrusters: they produce chemical propulsion, hence, a one-directional force through the expulsion of propellant. Their working principle and design realization are presented in detail in the following subsection.

3.4.3. Proposed model of thrusters

Thrusters can be mounted on the spacecraft in different configurations, with the purpose of providing the necessary force or torque along each of the spacecraft axes. In fact, unlike inertial actuators, they can be utilized to control all six dof of the satellite. Their main



Figure 3.3: Hydrazine thruster 8 – 25 N (*Credits: ArianeGroup*).

disadvantage lies in their inherent propellant requirement, which is a limited source that generally determines the lifetime of a spacecraft.

In the simulation framework, the system employs a thrusters representation that receives the six-dimensional force-torque input from the controller unit and produces a discretized output representing the actuated forces. This accurate emulation of the actuators' behavior is achieved through the utilization of a black-box Simulink model of thrusters in use at DLR, provided by external partners. This model implements a Thruster Management Function which optimizes the firings to provide the required forces and torques, while adhering to their power constraints and minimizing the overall firing energy. Furthermore, numerous input parameters can be specified to tailor it to the specific requirements of the desired simulation.

In the proposed scenario, the propulsion system is designed as a set of hydrazine-propelled thrusters, such as the ones produced by ArianeGroup, illustrated in Figure 3.3. The model is configured with twenty-four thrusters, strategically positioned to allow the cancellation of torque components. In particular, they are arranged in a cubic configuration, with a set of three orthogonal thrusters at each of the eight edges of the cube. Indeed, this arrangement intrinsically possesses a straightforward mapping relative to the spacecraft reference frame, preventing the generation of unwanted torques and facilitating their exploitation for their primary purpose: translational control.

The other main parameters given as input to the black-box model, to achieve the desired actuators' behaviour, are shown in Table 3.1. In particular, the specific impulse is a metric that quantifies the engine's effectiveness in generating propulsion. It is calculated as the thrust per unit of propellant consumed, thus an elevated value maximizes the efficiency of the propellant mass utilization. The minimum impulse bit defines the minimum firing time of a single thruster, which consequently determines the minimum torque that can

Thrusters	
Force magnitude	22 N
Specific impulse	291 s
Minimum impulse bit (MIB)	0.025 s
Firing cycle (sampling time)	0.2 s
MIB on firing fraction	4 %
Quantization on firing fraction	$9.9 \cdot 10^{-5}$ %

Table 3.1: Thrusters model parameters.

be exerted. Finally, the thruster quantization determines the optimal on/off times within the current time step. A range of realistic values, from which the one implemented in the model is chosen, is presented in [33].

3.4.4. Proposed model of reaction wheels

The attitude control system of satellites often consists of three or four RWs. In both cases, three-axis control of the spacecraft is achievable with a comparable total attitude pointing accuracy. However, the three-RWs configuration fundamentally inherits a catastrophic failure in the case of a malfunctioning of one of the wheels.

Thus, there exist mainly two different configurations with which these actuators are implemented on satellites. They are:

- Standard configuration;
- Pyramid configuration.

In particular, the standard configuration consists of three orthogonal RWs, used in normal working conditions, plus a fourth RW, which is able to give a torque contribution on each of the three spacecraft axes. Hence, this fourth RW is enabled only in extraordinary conditions. Whereas, in the pyramid configuration, the four RWs are all working simultaneously, and are positioned with a constant angle off-set with respect to the base plane. This results in a less complex mathematical mapping for the case considering the standard configuration. Therefore, the design of the RWs model is performed following the standard configuration characteristics.

Moreover, it should be noted that the spacecraft has a slow dynamic with respect to the RWs, which rotate at a much faster rate. Therefore, the actuator dynamics could even be

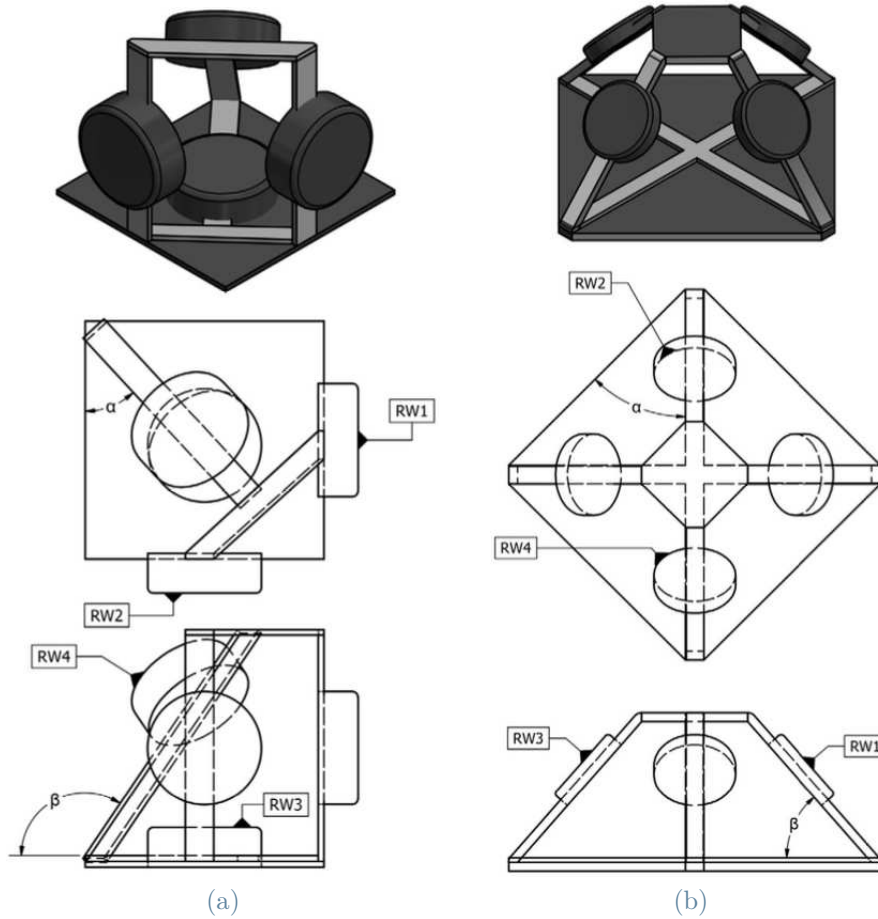


Figure 3.4: RWs main configurations: (a) standard configuration and (b) pyramid configuration [see 34].

neglected in modeling and analysis [34]. However, for high-precision attitude tracking, as in the case of space missions, the RWs dynamics is introduced in the control algorithm.

The RWs model is both mathematically implemented in Simulink and created in CoppeliaSim, as shown in Figure 3.5. Specifically, the latter is a simulation software that allows to design robotic systems and accurately recreate their dynamic motion. The model of these actuators is therefore generated utilizing realistic parameters, chosen from the RW-250 reaction wheels datasheet, produced by Astrofein. Indeed, these specific actuators are able to provide suitable power for the characteristics of the satellites targeted for the development of the docking control, involving a chaser mass of 300 kg. Hence, Table 3.2 summarizes the main RW values utilized to this end. Furthermore, the derivation of the matrix that maps the rigid body torque's need to the individual RWs torque's request, is presented.

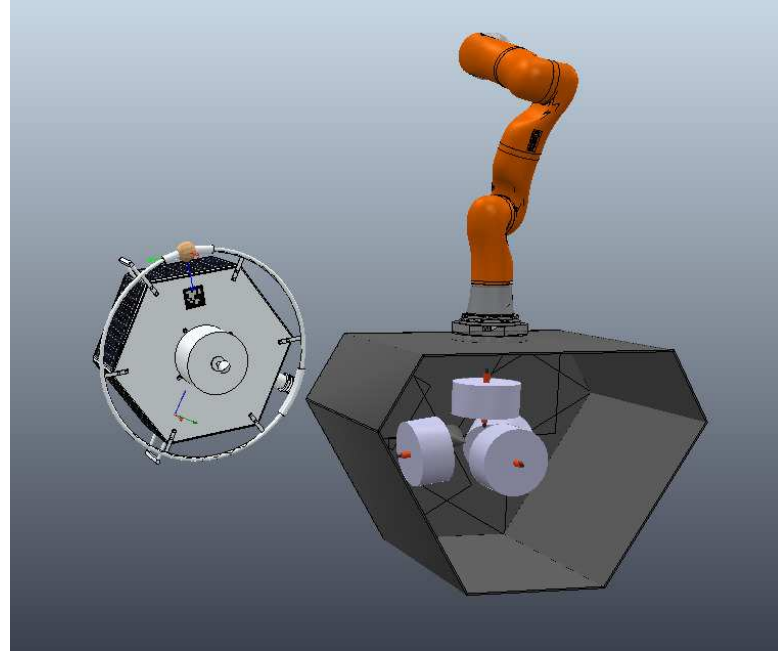


Figure 3.5: Client satellite on the left and servicer satellite, with the RW model implemented, on the right.

Astrofein RW-250	
Angular momentum	4.0 Nms @ 5000 rpm
Max. deliverable torque	0.1 Nm
Wheel mass	3 kg
Moment of inertia	$7.65 \cdot 10^{-3} \text{ kg} \cdot \text{m}^2$
Dimensions	100 mm, ϕ 200 mm
Supply voltage	23 – 34 V

Table 3.2: Reaction wheels model parameters (*Credits: Astrofein*).

In particular, the four-RWs standard configuration has two main working scenarios:

1. RWs aligned with the axis of the spacecraft;
2. RWs out of alignment with the spacecraft.

The first case is the simplest, as each of the three main RWs is aligned with an axis of the satellite, while the fourth, is arranged to have a contribution on each of the three axes. Consequently, the mapping related to the first configuration is expressed as

$$A_1 = \begin{bmatrix} 1 & 0 & 0 & -\cos \psi \sin \varphi \\ 0 & 1 & 0 & -\cos \psi \cos \varphi \\ 0 & 0 & 1 & \sin \psi \end{bmatrix}$$

being φ and ψ the in-pane and out-of-plane angles of the fourth RW, respectively.

In the second case, RWs and satellites are out of alignment, so a consistent mapping over time is required. Since the fourth RWs is activated only in the event of a malfunction of one of the other three, the new mapping is defined by a 3×3 matrix. In particular, it is obtained by solving the following equation:

$$\begin{bmatrix} \tau_x \\ \tau_y \\ \tau_z \end{bmatrix} = R_{rw1}^T \begin{bmatrix} 0 \\ 0 \\ \tau_1 \end{bmatrix} + R_{rw2}^T \begin{bmatrix} 0 \\ 0 \\ \tau_2 \end{bmatrix} + R_{rw3}^T \begin{bmatrix} 0 \\ 0 \\ \tau_3 \end{bmatrix} \quad (3.16)$$

where $R_{rw1}, R_{rw2}, R_{rw3}$ are the rotation matrices of the three RWs, with respect to the inertial frame. Particularly, each of the three matrices is defined in the following way:

$$R_{rwi} = \begin{bmatrix} (R_{11})_i & (R_{12})_i & (R_{13})_i \\ (R_{21})_i & (R_{22})_i & (R_{23})_i \\ (R_{31})_i & (R_{32})_i & (R_{33})_i \end{bmatrix}.$$

Hence, solving equation (3.16), the new mapping matrix A is derived:

$$\begin{bmatrix} \tau_x \\ \tau_y \\ \tau_z \end{bmatrix} = \underbrace{\begin{bmatrix} (R_{31})_1 & (R_{31})_2 & (R_{31})_3 \\ (R_{32})_1 & (R_{32})_2 & (R_{32})_3 \\ (R_{33})_1 & (R_{33})_2 & (R_{33})_3 \end{bmatrix}}_A \begin{bmatrix} \tau_1 \\ \tau_2 \\ \tau_3 \end{bmatrix} \quad (3.17)$$

Clearly, this mapping is valid for every type of orientation that the RWs model can have with respect to the spacecraft, thus for both the presented cases. On that account, it is

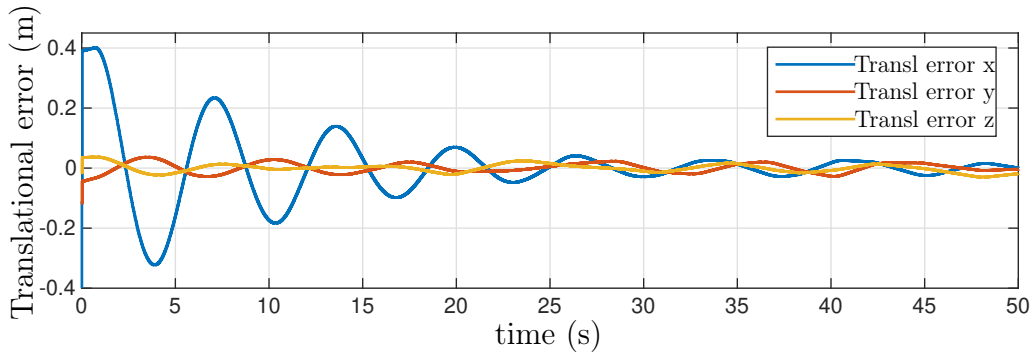


Figure 3.6: Servicer satellite translational errors over time.

the most reliable solution.

3.5. Results of the docking simulation

The model of thrusters and RWs are therefore integrated into the spacecraft's rigid body and tested alongside the controller presented in section 3.2. In particular, the simulation framework created through the synchronization of Simulink and CoppeliaSim allows the generation of high-fidelity data. Specifically, the RWs torques are obtained from the controller implemented in Simulink, and commanded to the CoppeliaSim realistic model, enabling rotational control. In parallel, discrete forces are directly commanded to the spacecraft model, to induce linear motion.

The results highlight the servicer satellite's ability to perform a successful docking operation toward a stationary reference, with stable and smooth behavior. The convergence of errors in the translation and rotation of the multibody system are presented in Figure 3.6, and Figure 3.8, respectively. Particularly, an absolute convergence of the linear error to zero is not achieved, reflecting the uncertainties voluntarily introduced through the thrusters model.

Moreover, once the desired configuration is matched, the RWs stop their rotational motion, as shown in Figure 3.9. Lastly, Figure 3.7 depicts both the theoretical and discretized values of the linear forces. The former are sent to the Simulink thrusters model, which returns the latter as an output, ultimately employed in the control task.

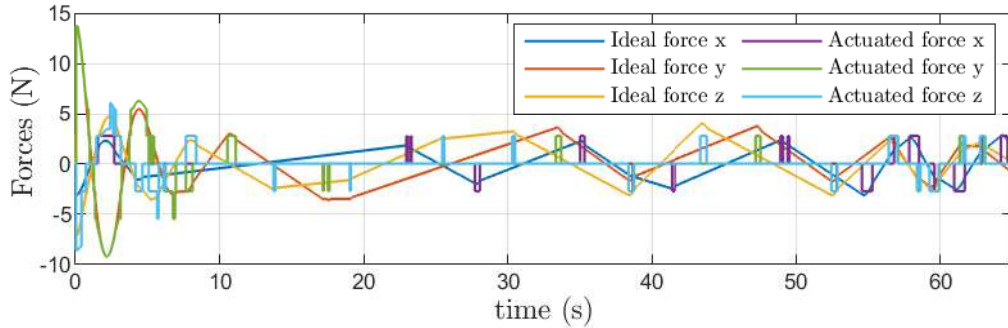


Figure 3.7: Servicer satellite ideal and actuated forces, during the docking maneuver.

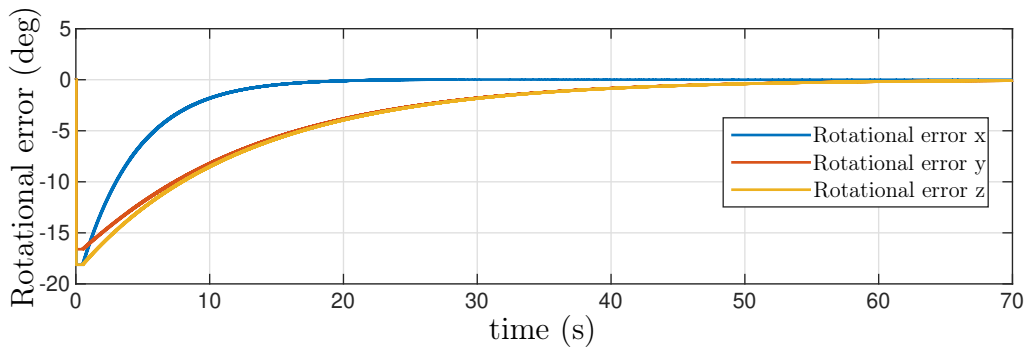


Figure 3.8: Servicer satellite rotational errors over time.

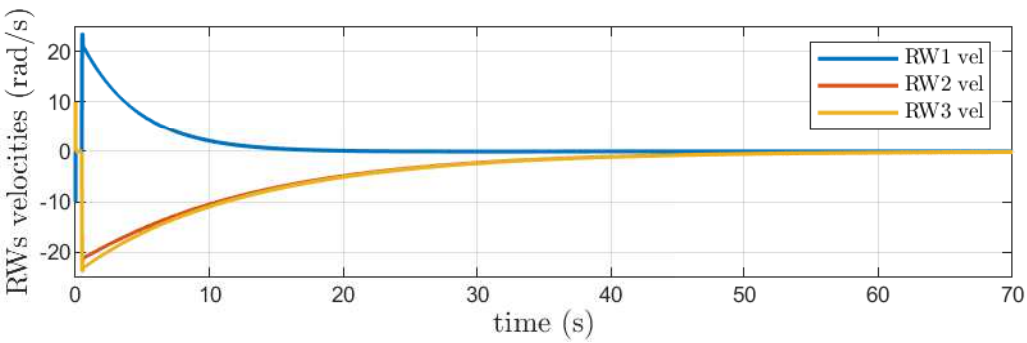


Figure 3.9: Velocities of the RWs during the docking maneuver.

4 | Absolute dynamics control of orbital multibody systems

4.1. Novel dynamics formulation of an orbital multi-body system

Satellites can be represented as orbital multibody systems by combining the dynamics of their body with that of their RWs within a single set of EoM. Since the RWs affect the rotation of the satellite, a new equation for computing the torques acting on the system is formulated. In particular, the external torque acting on the satellite τ_b is expressed through the following equation, which represents an extension of Euler's equation defined in (3.6):

$$\tau_b = I\dot{\omega} + I_wA\ddot{\theta} + \omega \times (I\omega + I_wA\dot{\theta}) \quad (4.1)$$

where \hat{m} defines the total mass, and I is the moment of inertia (MoI) of the multibody system. Specifically, the latter is expressed as

$$I = I_s + A^T I_w A \quad (4.2)$$

being I_s, I_w the MoI of the spacecraft base and RWs, respectively, and A the RWs mapping matrix, defined in equation (3.17). In parallel, the torques the RWs are exerting at a given time are described by the following dynamics formulation:

$$\tau_w = A^T I_w A\ddot{\theta} + A^T I_w \dot{\omega}. \quad (4.3)$$

Therefore, equations (4.1) and (4.3) are coupled to define the multibody dynamics in the following matrix form:

$$\begin{bmatrix} \begin{bmatrix} \hat{m} & 0 \\ 0 & I \\ 0 & A^T I_w \end{bmatrix} & \begin{bmatrix} 0 \\ I_w A \\ A^T I_w A \end{bmatrix} \end{bmatrix} \begin{bmatrix} \begin{bmatrix} \dot{v} \\ \dot{\omega} \\ \ddot{\theta} \end{bmatrix} \end{bmatrix} + \begin{bmatrix} \begin{bmatrix} \omega \times \hat{m} & 0 \\ 0 & \omega \times I \\ 0 & 0 \end{bmatrix} & \begin{bmatrix} 0 \\ \omega \times I_w A \\ 0 \end{bmatrix} \end{bmatrix} \begin{bmatrix} \begin{bmatrix} v \\ \omega \\ \dot{\theta} \end{bmatrix} \end{bmatrix} = \begin{bmatrix} \begin{bmatrix} f_b \\ \tau_b \\ \tau_w \end{bmatrix} \end{bmatrix} \quad (4.4)$$

In particular, it is possible to relate the EoM to the standard Hamel's equations formulation, defined by

$$\tilde{M}(g_b) \begin{bmatrix} \dot{V}_b \\ \ddot{\theta} \end{bmatrix} + \tilde{C}(g_b, \dot{g}_b) \begin{bmatrix} V_b \\ \dot{\theta} \end{bmatrix} = \begin{bmatrix} F_b \\ \tau_w \end{bmatrix}$$

where g_b is the body pose, $\tilde{M} = \begin{bmatrix} \tilde{M}_b & \tilde{M}_{b\theta} \\ \tilde{M}_{b\theta}^T & \tilde{M}_\theta \end{bmatrix}$ is the coupled inertia, and \tilde{C} is the non-unique CC matrix. However, the current dynamic formulation contains intrinsic complexity, mainly determined by the couplings inside the inertia matrix. In fact, this condition is detrimental toward the definition of a simple and effective control law. Therefore, the objective is to discover a variable transformation that can effectively decouple the inertial effects in the EoM of the floating-base robot. That is, achieving a mathematical representation of the system characterized by a block diagonal inertia matrix.

Hence, a new set of parameters (μ, θ) is introduced, representing the angular locked and shape-space system velocities, respectively. Specifically, the locked velocity is computed as a function of the total angular momentum of the system H_ω , expressed as

$$H_\omega = I\omega + I_w A \dot{\theta}.$$

The new velocity coordinate is then formulated as follows:

$$\begin{aligned} \mu &= I^{-1} H_\omega \\ &= \omega + \underbrace{(I^{-1} I_w A)}_{\Lambda} \dot{\theta}. \end{aligned} \quad (4.5)$$

Particularly, the coupling term, represented by the matrix product Λ , is known as the local mechanical connection in the context of differential geometry and as the dynamic-coupling factor within the field of orbital robotics [29].

Afterward, the change of coordinate is performed through the introduction of equation (4.5) into the simple dynamics (4.4). Namely, by applying the following transformation matrix:

$$T = \begin{bmatrix} I_3 & 0_3 & 0_{3,n} \\ 0_3 & I_3 & \Lambda \\ 0_{n,3} & 0_{n,3} & I_n \end{bmatrix} \quad s.t. \quad \zeta = T(g_b)V$$

where $V = [\mathbf{v} \ \boldsymbol{\omega} \ \dot{\theta}]^T \in \mathbb{R}^{6+n}$, and $\zeta = [\mathbf{v} \ \boldsymbol{\mu} \ \dot{\theta}]^T \in \mathbb{R}^{6+n}$. Being $n = 3$ the number of actuated RWs, which determines the dimension of the variable θ . Hence, $\Lambda \in \mathbb{R}^{3 \times 3}$. As a result of this transformation, a new expression for the external torque acting on the spacecraft is defined:

$$\tau_b = I\dot{\mu} - (I\Lambda + I_w A)\ddot{\theta} + \omega \times (I\mu) - \omega \times (\Lambda\dot{\theta}) + \omega \times (I_w A\dot{\theta}).$$

Moreover, by noticing that the equation $I\Lambda = I(I^{-1}I_w A) = I_w A$ holds, and by exploiting the cross-product properties, the angular locked system is reformulated as

$$\begin{aligned} \tau_b &= I\dot{\mu} + \omega \times (I\mu) \\ &= I\dot{\mu} + \mu \times (I\mu) - \Lambda\dot{\theta} \times (I\mu) \\ &= I\dot{\mu} + (\mu \times I)\mu + (I\mu \times \Lambda)\theta. \end{aligned} \tag{4.6}$$

Finally, the shape-space system is modeled as the difference between the RWs and the satellite torques. Specifically,

$$\begin{aligned} \tau_w - \Lambda^T \tau_b &= A^T I_w A \ddot{\theta} + A^T I_w \dot{\mu} - A^T I_w \Lambda \ddot{\theta} - \Lambda^T [I\dot{\mu} + (\mu \times I)\mu - \Lambda\dot{\theta} \times (I\mu)] \\ &= (A^T I_w A - A^T I_w \Lambda)\ddot{\theta} + (A^T I_w - \Lambda^T I)\dot{\mu} - (\Lambda^T \mu \times I)\mu + \Lambda^T \Lambda \dot{\theta} \times (I\mu) \\ &= (A^T I_w A - A^T I_w \Lambda)\ddot{\theta} - (\Lambda^T \mu \times I)\mu - (I\mu) \times \dot{\theta}. \end{aligned} \tag{4.7}$$

Consequently, equation (4.6) is coupled with equation (4.7) to generate the new mathematical model of the multibody system, defined as

$$\begin{bmatrix} \hat{m} & 0 & 0 \\ 0 & I & 0 \\ 0 & 0 & A^T I_w (A - \Lambda) \end{bmatrix} \begin{bmatrix} \dot{\mathbf{v}} \\ \dot{\mu} \\ \ddot{\theta} \end{bmatrix} + \begin{bmatrix} (\mu - \Lambda\dot{\theta}) \times \hat{m} & 0 & 0 \\ 0 & \mu \times I & I\mu \times \Lambda \\ 0 & -\Lambda^T \mu \times I & -(I\mu) \times \end{bmatrix} \begin{bmatrix} \mathbf{v} \\ \mu \\ \dot{\theta} \end{bmatrix} = \begin{bmatrix} f_b \\ \tau_b \\ \tau_w - \Lambda^T \tau_b \end{bmatrix}.$$

In fact, the EoM are now fully inertially decoupled, thus, they satisfy the block diagonal inertia matrix condition. Moreover, the compatibility of the current model with the

following matrix form is achieved:

$$\begin{bmatrix} M_l & 0 & 0 \\ 0 & M_r & 0 \\ 0 & 0 & M_\theta \end{bmatrix} \dot{\zeta} + \begin{bmatrix} C_{ll} & C_{lr} & C_{l\theta} \\ -C_{lr}^T & C_{rr} & C_{r\theta} \\ -C_{l\theta}^T & -C_{r\theta}^T & C_{\theta\theta} \end{bmatrix} \zeta = \begin{bmatrix} F_b \\ \tau_w - \Lambda^T \tau_b \end{bmatrix}. \quad (4.8)$$

This demonstrates the alignment of the results from [29] with the system, granting a formulation of the mathematical model characterized by its simplicity and effectiveness.

4.2. Stability of the multibody system

In order to prove the stability of the multibody system formed by the servicer satellite and the RWs, it is necessary to find a Lyapunov function candidate that is able to satisfy the three requirements of the direct method. The function describing the total energy of the system in terms of the new set of velocities ζ is selected:

$$W = \frac{1}{2}\mu^T I \mu + \frac{1}{2}\dot{\theta}^T (A^T I_w (A - \Lambda)) \dot{\theta} + \frac{1}{2}\nu^T \hat{m} \nu + \frac{1}{2} \text{tr}(K_p(I_3 - R_e)) + \frac{1}{2} \Delta x^T K_p \Delta x. \quad (4.9)$$

Proving that the proposed candidate is positive definite is trivial for the most part. However, demonstrating this for the RWs inertia requires the utilization of the Schur's complement. This Lemma proves that given a square positive matrix $Q = \begin{bmatrix} A & B \\ B^T & C \end{bmatrix}$, then $C - B^T A^{-1} B > 0$. Noticeably, the RWs inertia can be obtained through the presented formula, considering the inertia matrix expressed in its initial form, observable in equation (4.4), as Q . Hence, the Lyapunov candidate derivative is written as

$$\dot{W} = \mu^T I \dot{\mu} + \dot{\theta}^T (A^T I_w A - A^T I_w \Lambda) \ddot{\theta} + (\text{skew}(K_p R_e)^\vee)^T \omega + \nu^T \hat{m} \dot{\nu} + \Delta x^T K_p \nu. \quad (4.10)$$

For the sake of simplicity, the angular potential is defined by the following compact notation:

$$\gamma = \text{skew}(K_p R_e)^\vee. \quad (4.11)$$

Hence, the Lyapunov derivative is rewritten as

$$\begin{aligned} \dot{W} &= \mu^T I \dot{\mu} + \dot{\theta}^T (A^T I_w A - A^T I_w \Lambda) \ddot{\theta} + \gamma^T (\mu - \Lambda \dot{\theta}) + \nu^T (\hat{m} \dot{\nu} + K_p \Delta x) \\ &= \mu^T (I \dot{\mu} + \gamma) + \dot{\theta}^T (A^T I_w A \ddot{\theta} - A^T I_w \Lambda \ddot{\theta} - \Lambda^T \gamma) + \nu^T (\hat{m} \dot{\nu} + K_p \Delta x). \end{aligned}$$

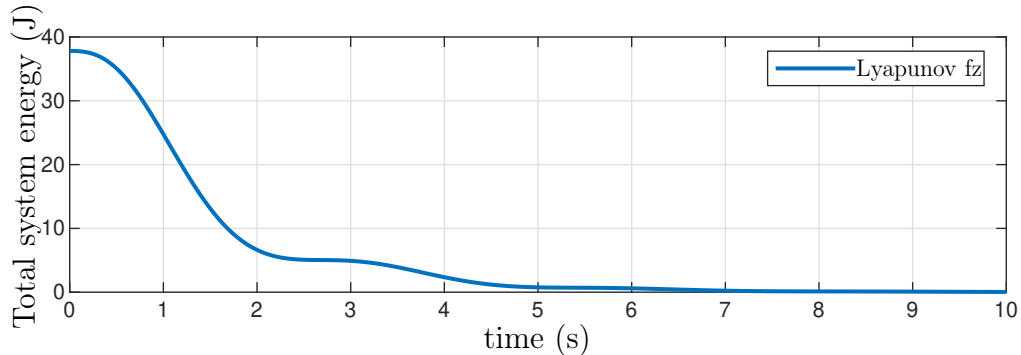


Figure 4.1: Multibody system's Lyapunov function over time.

It should be noted that the asymptotic stability of the translational dynamics has already been addressed in section 3.3.2, through the use of a PD control, shown in equation (3.7). Thus, it is worth focusing on the attitude stabilization problem, for which it is possible to define three different scenarios.

4.2.1. Free-floating control

The free-floating case considers the multibody system as underactuated. In fact, the torques produced by the RWs are internal forces, which do not produce a change in the generalized angular momentum. Therefore, this scenario is characterized by a null angular momentum, that translates into a null locked velocity μ . This implies that the internal force produced by the RWs is necessary and sufficient to stabilize the system to a desired configuration. Hence, the Lyapunov function terms containing μ can be discarded, leading to the following formulation of the candidate derivative:

$$\dot{W} = \dot{\theta}^T (A^T I_w A \ddot{\theta} - A^T I_w \Lambda \ddot{\theta} - \Lambda^T \gamma). \quad (4.12)$$

Therefore, it is possible to introduce the RWs feedback torque control, which assumes the following form:

$$\tau_w = \underbrace{(A^T I_w A - A^T I_w \Lambda)}_{\text{Dynamics}} \ddot{\theta} = \underbrace{\Lambda^T \gamma - K_d \dot{\theta}}_{\text{Control action}} \quad (4.13)$$

where K_d is a positive parameter identifying the derivative gain, whereas, the proportional gain is included in the function γ , as presented in equation (4.11). Thus, replacing equation (4.13) inside (4.12), the candidate derivative can be rewritten as the following negative semi-definite function:

$$\dot{W} = -\dot{\theta}^T K_d \dot{\theta}$$

which finally proves the stability in the sense of Lyapunov of the free-floating satellite system, actuated by RWs. In addition, such a function assumes zero values only when the equilibrium configuration is achieved: the system is therefore asymptotically stable.

Specifically, the Lyapunov function plotted over time can be observed in Figure 4.1. The stability is indeed confirmed in simulation by the consistently decreasing trend of the system's energy, confirming the semi-negative nature of its derivative. Notably, consistent results are achieved in the following cases.

All proposed control models are tested in simulation, enabling a comprehensive analysis of their differences, and facilitating a data-driven decision regarding the most suitable control model to apply in specific conditions. All cases show the stability of the system, considering an offset from the equilibrium condition of about five degrees in the three main directions. Following, the data obtained with the current free-floating control law.

In particular, Figure 4.2 shows the trend of the torques produced by the RWs, their velocities, which peak at about 600 *rpm*, and the rotational error, which takes 140 s circa to converge to zero.

4.2.2. Inertia shaping on reaction wheels

Simulation results prove that the current free-floating control is not sufficiently effective to be implemented in a mission scenario. In fact, the control proposed in equation (4.18) generates a torque value that is not adequate to satisfy a realistic value of the nominal velocity of RWs. This inherent control problem is caused by the presence of the inertia-proportional matrix $\Lambda = I^{-1}I_wA$, whose magnitude is extremely low due to the significant difference in the inertia values of the two components building the current multibody systems. Furthermore, this problem cannot be effectively overcome by simple gain tuning. In fact, very high gains do not provide a satisfactory behavior of the system. Moreover, they would extensively amplify the noise, making the controller ineffective.

Therefore, considering the advantages that inertia shaping (IS) has delivered in robotics in terms of control design freedom [35], a modification of the RWs controller through this technique is investigated. The detailed benefits of IS are presented by Albu-Schäffer et al., who applied this method to flexible joint robots [36]. In their work, the fast actuation dynamics is decoupled from the multibody base, as shown for a spacecraft in this thesis. Hence, the torque feedback control is modeled to achieve an IS of the motors' kinetic energy, making the overall robot's actuation quicker and more efficient.

Specifically, IS consists of feedback linearization and is here applied to the rotor dynamics

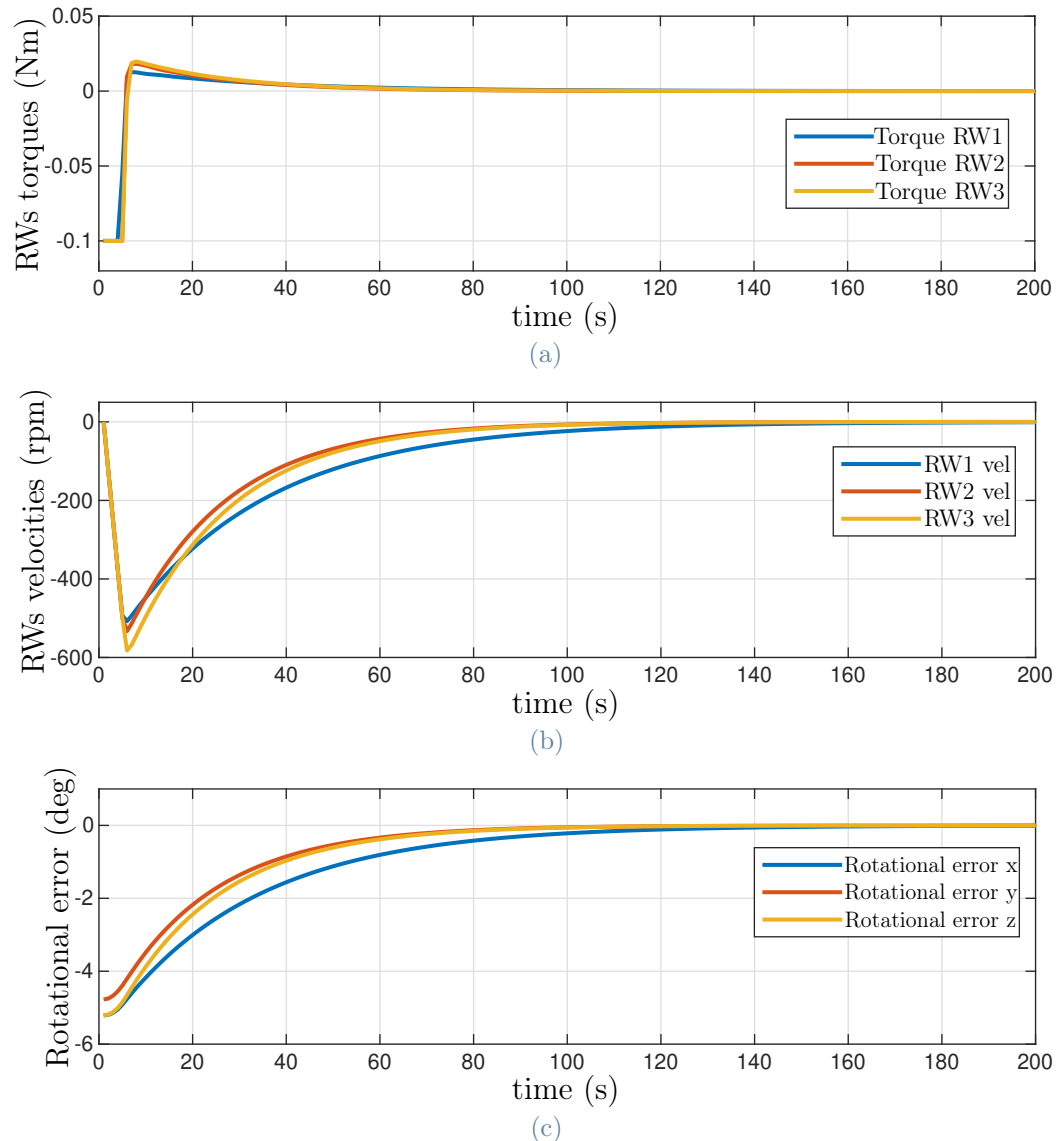


Figure 4.2: Free-floating control results: RWs torques (a), RWs velocities (b), and rotational error (c).

only. Notably, the inertia of the actuators is artificially reduced. Considering that for the considered case, the mapping matrix A equals identity, the scaling term is suggested by the dynamics itself, and is equal to Λ^T . Hence, the new RWs dynamics is rewritten as

$$\Lambda^T(\tau_w - \Lambda^T\tau_b) = \Lambda^T M_\theta \ddot{\theta} + \Lambda^T C_\theta \dot{\theta}. \quad (4.14)$$

Afterward, the Lyapunov candidate for this new system is defined as

$$W_\theta = \frac{1}{2}\dot{\theta}^T(\Lambda^T M_\theta)\dot{\theta} + \frac{1}{2}\text{tr}(K_p(I_3 - R_e)).$$

Particularly, in the proposed function, the positive definite inertia matrix M_θ multiplies the shaping term Λ^T , constituted of two diagonal inertia matrices and a mapping matrix. Since in the selected configuration of RWs, the mapping matrix A equals identity, the shaping term is also a positive diagonal matrix, proving the current Lyapunov candidate as positive definite. Furthermore, the function's derivative is

$$\dot{W}_\theta = \dot{\theta}^T(\Lambda^T M_\theta - \gamma)\ddot{\theta}.$$

Consequently, it is now possible to apply a simple feedback law of the type:

$$\tau_w = \underbrace{\Lambda^T M_\theta \ddot{\theta}}_{\text{Dynamics}} = \underbrace{\gamma - K_d \dot{\theta}}_{\text{Control action}}$$

which leads to the recurrent form of the Lyapunov derivative:

$$\dot{W}_\theta = -\dot{\theta}^T K_d \dot{\theta}.$$

In conclusion, the inertia-shaped system meets the criteria for asymptotic stability. This approach changes the way the momentum is transferred within the system: the RWs now behave as if they possessed a lower inertia, thus largely increasing their responsiveness. Therefore, they are able to apply a more substantial torque contribution.

The benefits of IS are reflected in the results (Figure 4.3): the torques produced by the actuators are higher, leading to a peak velocity of about 1300 rpm, almost 220 % higher than the case without IS, and promptly damped out in order to achieve a fast and stable convergence of the rotational error to zero. Specifically, the equilibrium is now reached in about 40 s only, leading to a reduction of the error curve's settling time of more than 70 %.

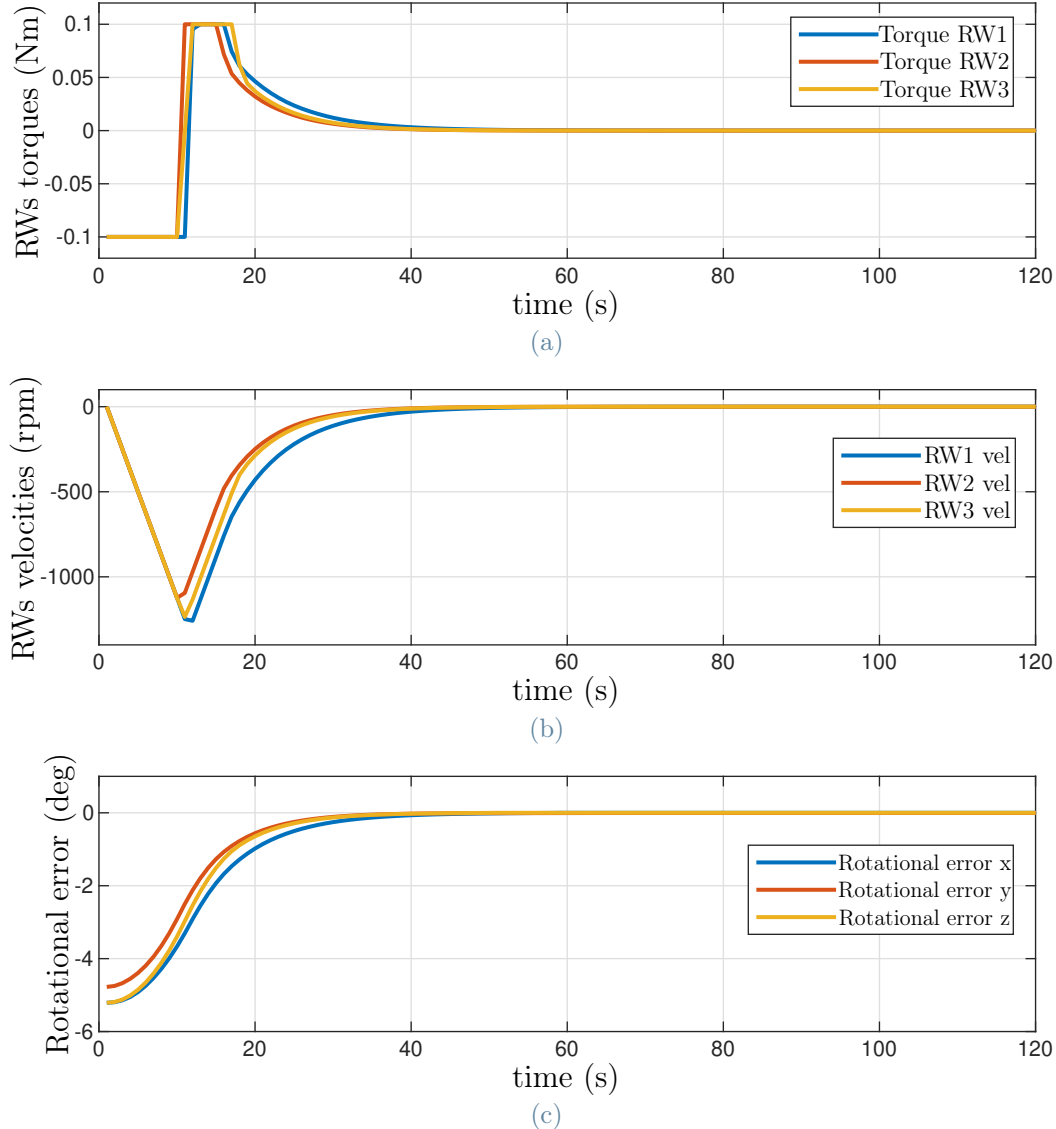


Figure 4.3: Free-floating control results with inertia shaping: RWs torques (a), RWs velocities (b), and rotational error (c).

4.2.3. Free-flying control

In contrast to the free-floating case, this scenario is characterized by a non-zero angular momentum. Accordingly, the Lyapunov function derivative for this operation conditions is expressed in (4.10), considering the shaped-inertia kinetic energy. As a consequence, a second feedback law, controlling the external torques, is introduced:

$$\tau_b = \underbrace{I\dot{\mu} + (\mu \times I)\mu + (I\mu \times \Lambda)\dot{\theta}}_{Dynamics} = \underbrace{-\gamma - K_d^b\mu + (I\mu \times \Lambda)\dot{\theta}}_{Control\ action} \quad (4.15)$$

Whereas, the RWs dynamics, defined as in (4.7), is regulated through the following expression:

$$\tau_w - \Lambda^T \tau_b = \underbrace{\gamma - K_d^w \dot{\theta} + \Lambda^T (-\Lambda^T \mu \times I) \mu + \Lambda^T (-I \mu) \times \dot{\theta}}_{\text{Control action}}. \quad (4.16)$$

Notably, in this case, the CC couplings must be canceled within the control laws due to the inertia shaped rotors. Moreover, the RWs control law includes the CC term multiplying their velocity, because the presence of the shaping term Λ^T breaks the skew-symmetry structure of such matrix, and the assumption $\mu = 0$ is no longer valid. Afterward, a new form of the Lyapunov derivative is obtained by coupling its base form, expressed in equation (4.10), with the proposed torque feedback laws:

$$\begin{aligned} \dot{W} &= -\mu^T K_d^b \mu - \dot{\theta}^T K_d^w \dot{\theta} - \mu^T (I \mu \times \Lambda) \dot{\theta} + \dot{\theta}^T (\Lambda^T \mu \times I) \mu \\ &= -\mu^T K_d^b \mu - \dot{\theta}^T K_d^w \dot{\theta}. \end{aligned} \quad (4.17)$$

Since the derivative gains K_d^b, K_d^w are strictly positive parameters, the Lyapunov derivative is once again a negative definite function for any value that the velocity $\zeta = [\mathbf{v} \ \mu \ \dot{\theta}]^T$ can assume, except for the equilibrium point, where the function is null. The asymptotic stability of the free-flying multibody system is demonstrated.

Data extrapolated from the simulation performed with free-flying control show some obvious differences from the previous method. In fact, RWs are no longer employed uniquely in the action of providing stability to the system. Thus, their average rotational velocities are slightly lower, as can be observed in Figure 4.4b. Moreover, they do not converge perfectly to zero. This is due to the use of the realistic model of thrusters, which does not allow for a perfect cancellation of the total momentum in the system. Accordingly, the error does not converge perfectly to zero but reaches a stationary condition at around $-1 \deg$ (Figure 4.4c). Finally, this peculiarity of the system is well represented by the comparison between the ideal torques and those that are actually implemented by the thrusters during the simulation, shown in Figure 4.4d. These actuators are modeled with a minimum deliverable torque of about 1.5 Nm , which clearly does not allow the torque need of the system, represented by their ideal values, to be brought perfectly to zero. Particularly, some torque residuals of 1 Nm remain.

4.2.4. Hierarchical control

Lastly, the attitude problem is tackled by organizing the two main control tasks into a structured hierarchy. In particular, this method ensures the optimal cooperation of the whole set of actuators, aiming at the full exploitation of the RWs stabilization capabilities,

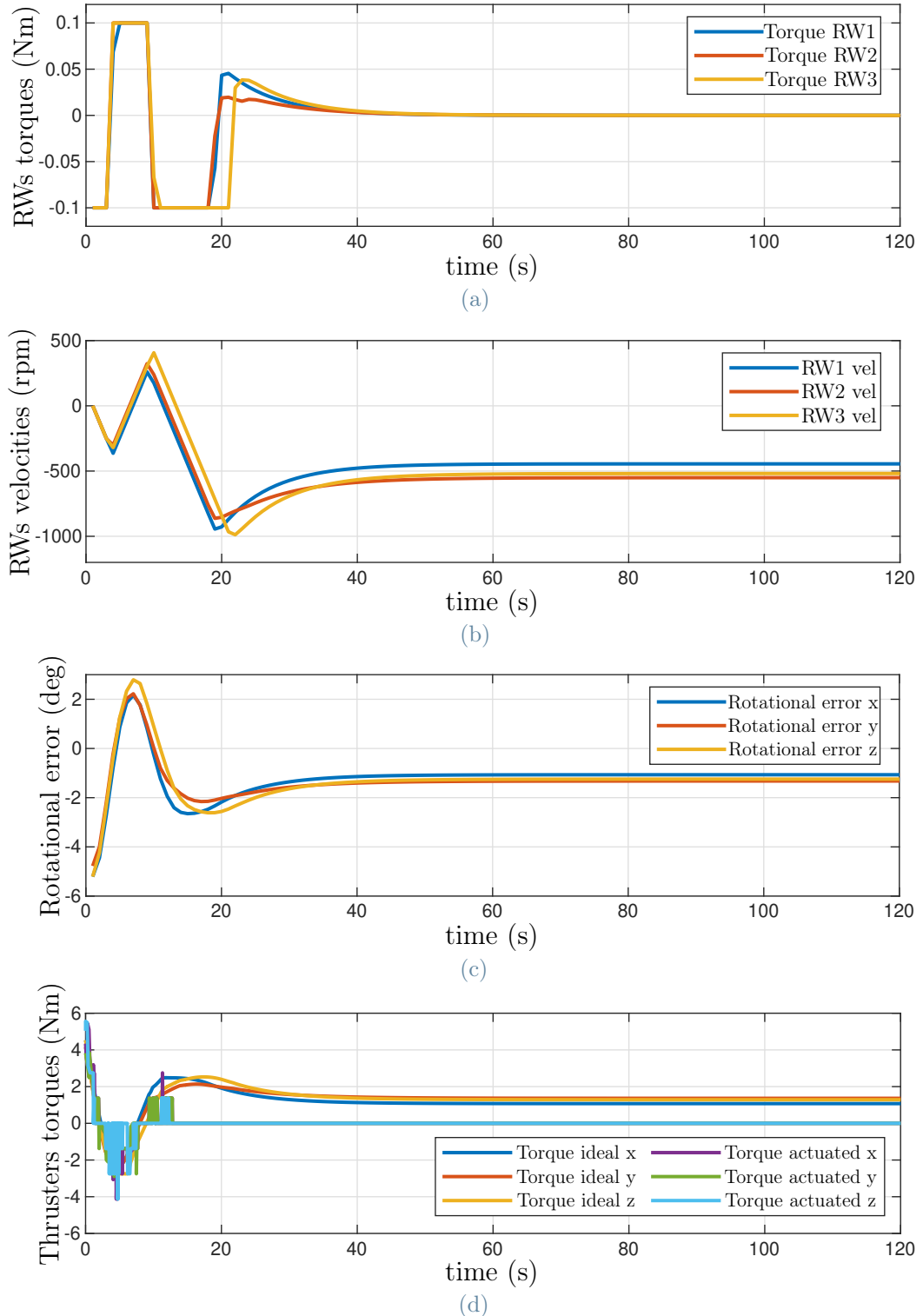


Figure 4.4: Free-flying control results: RWs torques (a), RWs velocities (b), rotational error (c), and ideal torques vs torques actuated by the thrusters model (d).

to eventually improve the overall performance of the system. Specifically, the docking objective is subdivided into two tasks. In the presence of initial spacecraft spinning, the thrusters are employed to counteract this motion and stabilize the system via an external torque. Afterward, once the cancellation of any residual momentum is accomplished, the RWs are utilized to execute the rotational control of the satellite.

As a result, two different Lyapunov functions, corresponding to the two separate operations, must be expressed and analyzed. Initially, the function candidate related to the spinning stabilization is defined as

$$W_1 = \frac{1}{2} \mu^T I \mu.$$

whose derivative assumes the following form:

$$\dot{W}_1 = \mu^T I \dot{\mu}.$$

Therefore, the system is brought to a static condition in a stable fashion, by the following control feedback law:

$$\tau_b = \underbrace{I \dot{\mu} + (I \mu \times \Lambda) \dot{\theta}}_{\text{Dynamics}} = \underbrace{-K_d^b \mu + (I \mu \times \Lambda) \dot{\theta}}_{\text{Control action}}$$

At this stage, a null angular momentum of the system is ensured, which allows to safely apply the assumption $\mu = 0$. Hence, the second Lyapunov derivative is defined as

$$W_2 = \frac{1}{2} \dot{\theta}^T \Lambda^T (A^T I_w A - A^T I_w \Lambda) \dot{\theta} + \frac{1}{2} \text{tr}(K_p^w (I_3 - R_e))$$

whose derivative is:

$$\dot{W}_2 = \dot{\theta}^T \Lambda^T M_\theta \ddot{\theta} + \gamma^T (\mu - \Lambda \dot{\theta}).$$

Finally, by introducing the actuators' internal torque:

$$\tau_w = \underbrace{\Lambda^T M_\theta \ddot{\theta}}_{\text{Dynamics}} = \underbrace{\gamma - K_d^w \dot{\theta}}_{\text{Control action}} \quad (4.18)$$

the standard notation of the stable Lyapunov derivative, $\dot{W}_2 = -\dot{\theta}^T K_d^w \dot{\theta}$, is achieved. Accordingly, by following the mathematical steps explained for the previous control cases, the asymptotic stability of the system is proved. This type of control combines the previous two methods, optimizing the use of thrusters and exploiting the full potential of RWs. In particular, once the system is stabilized by pre-existing spinning, the control ideally relies solely on RWs, behaving exactly like a free-floating control.

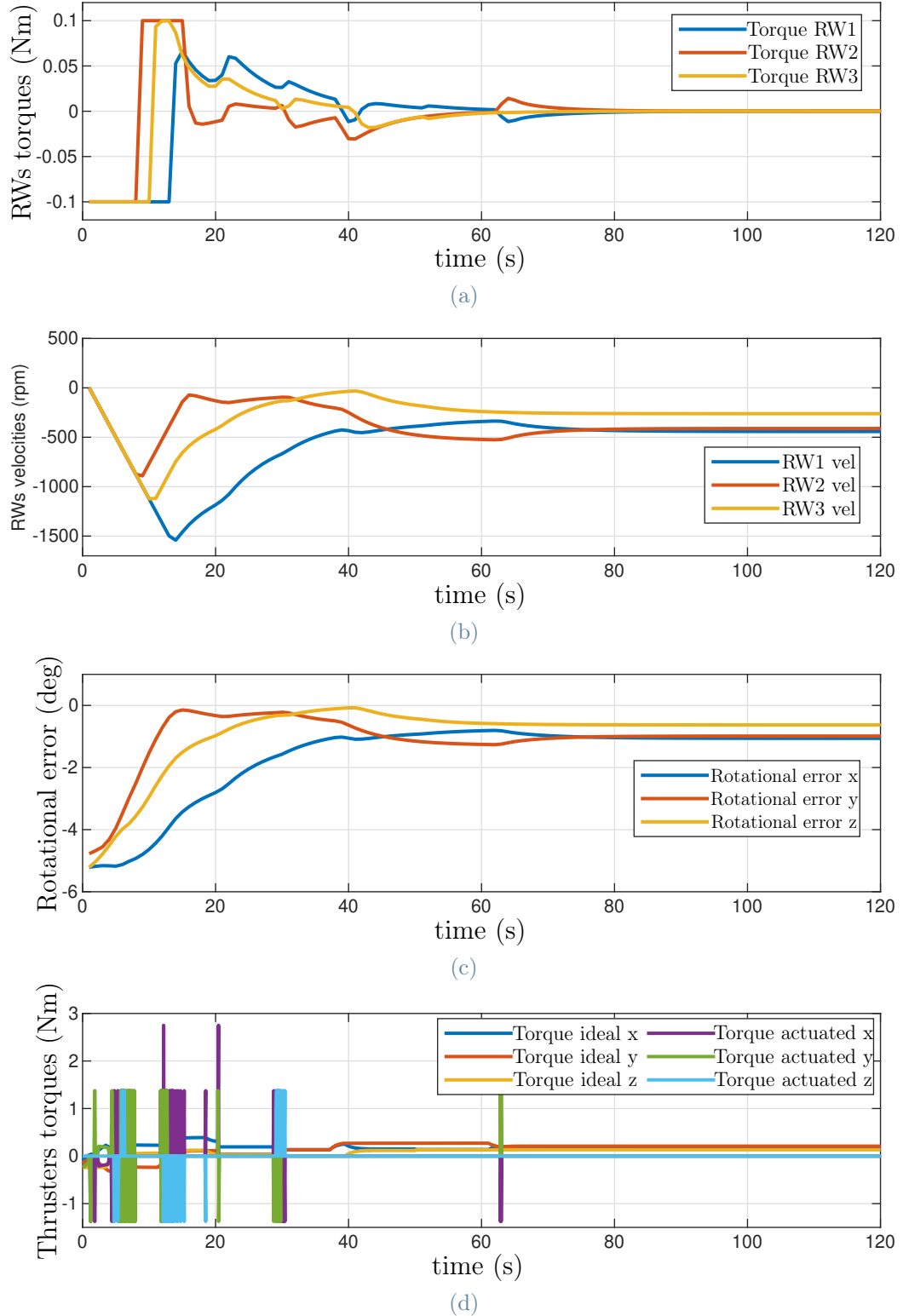


Figure 4.5: Hierarchical control results: RWs torques (a), RWs velocities (b), rotational error (c), and ideal torques vs torques actuated by the thrusters model (d).

In particular, from Figure 4.5, it can be noted that the use of RWs is prioritized to perform the required task. In fact, their speeds reach a peak of 1500 rpm , 50 % higher compared to the free-flying mode. Furthermore, the steady-state error in the rotation is reduced to 0.5 deg , making the control more precise by the 50 %. However, it is inherently slower: a settling time of 80 s is registered, hence, 30 % more time is required to achieve stability. Finally, from the thruster's torque graph in Figure 4.5, a consistent torque delivery is observed in the first part of the simulation, aiming to cancel out the system's momentum. Much of this goal is successfully achieved, however, as in the previous case, residual momentum remains, again causing the rotational error and RWs velocity to not converge perfectly to zero, respecting the natural behavior of a non-ideal system. Particularly, the ideal torques residuals have a magnitude of about 0.25 Nm , 75 % lower compared to the free-flying approach.

4.2.5. Comparison between the proposed control methods

In summary, when considering all the potential scenarios and their impact on the system in question, it is evident that the RWs are able to effectively stabilize the spacecraft when the satellite is not tumbling in space, resulting in a null total angular momentum. In contrast, if the satellite is already spinning, relying only on RWs is not sufficient to perform operations of re-orientation or stabilization. Indeed, the saturation level of the actuators would be reached. Consequently, an additional external source of torque is required for this purpose. For instance, thrusters can fulfil this requirement.

However, it is important to take into account the fuel availability and consumption, which represent a major constraint for thrusters' actuation, particularly given their primary implementation toward the stabilization of the satellite translational motion in space. Specifically, the average fuel mass consumption per thruster is calculated as

$$M_p = M_{SC0} \frac{\left(1 - e^{-\frac{\Delta V}{g \cdot I_{sp}}}\right)}{\left(2 - e^{-\frac{\Delta V}{g \cdot I_{sp}}}\right)}$$

where M_{SC0} is the initial spacecraft mass, g the gravity constant, ΔV the change in velocity, and I_{sp} the specific impulse, defined in Table 3.1

Accordingly to the design of the control approaches, data from Figure 4.6 prove that the hierarchical is 25 % more efficient than the free-flying control, in terms of fuel consumption.

In conclusion, three different types of controllers are presented: from the most basic to the most comprehensive. Free-flying control is preferred when particular quickness in the reorientation maneuver is required, whereas, hierarchical in case the requirements

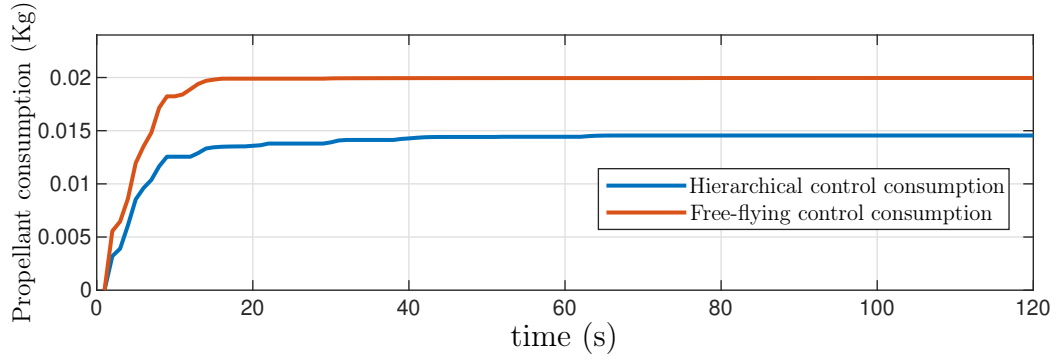


Figure 4.6: Average fuel mass consumed by a thruster in hierarchical and free-flying operational modes.

include high accuracy, or in case fuel economy is desired. Considering that in space missions significant precision and fuel availability are often prioritized over maneuver time, hierarchical control is arguably the more robust solution in many scenarios. Nevertheless, in general, the choice of the controller to be implemented should be carefully tailored to the needs and restrictions that the space operation holds.

5 | Relative dynamics control of orbital multibody systems

5.1. Introduction to the simulation scenario

The design of the relative motion controller for two or more active multibodies, such as two satellites docking while simultaneously moving in space, is explored. This condition adds complexity to the simulation, demanding a more robust control algorithm compared to the more basic cases, previously explored in the thesis.

Hence, the servicer satellite, after achieving the appropriate proximity for docking, must maintain alignment with the client, following its trajectory and matching its velocity. Consequently, once the two spacecraft synchronize and connect, they form a new and distinct multibody system. Moreover, both satellites effectively change their reference frames during the maneuver. This introduces the need for additional coordinate transformations and adjustments in the control formulation.

At the same time, this scenario offers advantages by providing a more realistic and challenging environment for assessing the performance and validating the control against actual mission data, ultimately developing a more robust, adaptable and effective solution for satellites docking, and, more generally, for the coordinated movement of floating-base robots.

5.2. Main concept of the proposed dynamics formulation

The concept utilized in the description of the relative dynamics of multiple agents is based on the passive decomposition of the group dynamics into two new inertia-decoupled systems, called shape and locked, as proposed in [27]. The former represents the shape formation within the group, i.e. the relative dynamics, and the latter describes the overall group maneuver, i.e. the total dynamics. Both new systems can be controlled individually,

or simultaneously, facilitating the achievement of multiple configurations and tasks, such as docking, formation flight, and collision avoidance.

The concept behind the creation of the two new systems can be presented using a simple example. Consider two 1 dof bodies having mass m_1, m_2 moving along the x -axis. Their dynamics is described as $f_1 = m_1\ddot{x}_1$ and $f_2 = m_2\ddot{x}_2$, under the assumption of the two agents being observed in the same reference frame. Consequently, their internal group formation could then be written via a simple equation $x_E = x_1 - x_2$, and their group maneuver as $x_L = \frac{1}{2}(x_1 + x_2)$. The new total system is then described by the following set of equations:

$$M(x_{12}) \begin{bmatrix} \ddot{x}_L \\ \ddot{x}_E \end{bmatrix} + C(x_{12}, \dot{x}_{12}) \begin{bmatrix} \dot{x}_L \\ \dot{x}_E \end{bmatrix} = \begin{bmatrix} F_L \\ F_E \end{bmatrix}. \quad (5.1)$$

However, they are characterized by consistent couplings in both the inertia and CC matrices. As a result, the expansion of this problem into the 6 dof would lead to extreme complexity in the design of a control and poor robustness in its performance.

Consequently, [27] proposes a different formulation of the new systems. Notably, the shape system velocity is modeled as $\dot{x}_E = \dot{x}_2 - \dot{x}_1$, whereas, the locked system's parameter as $\dot{x}_L = (m_1 + m_2)^{-1}h$, being $h = m_1\dot{x}_1 + m_2\dot{x}_2$ the total momentum of the system.

Through such a formulation, the shape and lock system dynamics remain in a standard form, similar to that of a single mechanical system. Hence, the Lagrangian structure of the individual systems is preserved [37]. Additionally, the two newly created systems are passively decoupled from an energy perspective. This means that the total energy of the bodies is conserved in the energies of the shape and locked systems, without the need for an input of net energy.

Specifically, by deriving the new set of equations in the form of (5.1) with this approach, it is possible to prove that the total inertia matrix has a block-diagonal form and that the couplings in the CC matrix do not alter the conservation of the total energy of the system. As a result, contrary to the work proposed in [1], this system can be controlled without the need for acceleration measurements, exceptionally increasing the control's adaptability and resilience.

Therefore, the dynamics is expanded to the multiple 6 dof multibody systems scenario in the following section.

5.3. Novel inertia-decoupled relative dynamics formulation

Consider two spacecraft actuated by thrusters and RWs. Their EoM are defined separately as follows:

$$M_i(g_i) \begin{bmatrix} \dot{v}_i \\ \dot{\mu}_i \\ \ddot{\theta}_i \end{bmatrix} + C_i(g_i, \dot{g}_i) \begin{bmatrix} v_i \\ \mu_i \\ \dot{\theta}_i \end{bmatrix} = \begin{bmatrix} f_i \\ \tau_i \\ \tau_{w_i} - \Lambda^T \tau_i \end{bmatrix} \quad \forall i = 1, 2. \quad (5.2)$$

Recalling that $\xi_i = [v_i \ \mu_i]^T$, and that g_{12} is the relative pose between the two bodies, the two sets of equations can be grouped together in the following fashion:

$$\underbrace{\begin{bmatrix} M_1 & 0 & 0 & 0 \\ 0 & M_2 & 0 & 0 \\ 0 & 0 & M_{\theta_1} & 0 \\ 0 & 0 & 0 & M_{\theta_2} \end{bmatrix}}_{M_{1,2}(g_{12})} \underbrace{\begin{bmatrix} \dot{\xi}_1 \\ \dot{\xi}_2 \\ \ddot{\theta}_1 \\ \ddot{\theta}_2 \end{bmatrix}}_{C_{1,2}(g_{12}, \dot{g}_{12})} + \underbrace{\begin{bmatrix} C_{11} & 0 & C_{1\theta_1} & 0 \\ 0 & C_{22} & 0 & C_{2\theta_2} \\ -C_{1\theta_1}^T & 0 & C_{\theta_1} & 0 \\ 0 & -C_{2\theta_2}^T & 0 & C_{\theta_2} \end{bmatrix}}_{C_{1,2}(g_{12}, \dot{g}_{12})} \begin{bmatrix} \xi_1 \\ \xi_2 \\ \dot{\theta}_1 \\ \dot{\theta}_2 \end{bmatrix} = \begin{bmatrix} F_1 \\ F_2 \\ \tau_{w_1} - \Lambda^T \tau_1 \\ \tau_{w_2} - \Lambda^T \tau_2 \end{bmatrix}. \quad (5.3)$$

This dynamics formulation is then exploited to artificially construct the two new (shape and locked) systems presented in the previous section. Hence, the total momentum H of the satellites is stated as

$$H = M_1 \xi_1 + Ad_{g_{12}}^{-T} M_2 \xi_2 \quad (5.4)$$

where the adjoint action of a transformation matrix g is defined in equation (3.5), and satisfies the following conditions:

$$\begin{cases} \hat{V}_b = Ad_{g_{ab}} V_b = g_{ab} V_b g_{ab}^{-1} \\ \hat{F}_b = Ad_{g_{ba}}^* F_b. \end{cases}$$

Henceforth, the notation $\hat{\cdot}$ is used to define velocities and forces of a body that are computed in the frame of the second other system involved, e.g. \hat{V}_b represents the velocity of body b in frame a . Thus, the new velocity parameters of the locked and shape dynamics

are, respectively:

$$\begin{cases} V_L = M_{tot}^{-1} H \\ V_E = \xi_2 - Ad_{g12}^{-1} \xi_1 \end{cases}$$

where the total inertia of the system is described as

$$M_{tot} = M_1 + Ad_{g12}^{-T} M_2 A d_{g12}^{-1}$$

being M_1, M_2 the inertia matrices of systems 1 and 2, in their own frame. Therefore, the shape velocity V_E is introduced into equation (5.4), to formulate a momentum definition that highlights the presence of the total inertia:

$$\begin{aligned} H &= M_1 \xi_1 + Ad_{g12}^{-T} M_2 (V_E + Ad_{g12}^{-1} \xi_1) \\ &= (M_1 + Ad_{g12}^{-T} M_2 A d_{g12}^{-1}) \xi_1 + Ad_{g12}^{-T} M_2 V_E \\ &= M_{tot} \xi_1 + Ad_{g12}^{-T} M_2 V_E \end{aligned}$$

leading to the complete state of the locked system velocity V_L :

$$\begin{aligned} V_L &= M_{tot}^{-1} H \\ &= \xi_1 + \underbrace{M_{tot}^{-1} Ad_{g12}^{-T} M_2 V_E}_{A^*} \\ &= (I_6 - A^* Ad_{g12}^{-1}) \xi_1 + A^* \xi_2. \end{aligned} \tag{5.5}$$

Following, the transformation matrix $S \in \mathbb{R}^{18 \times 18}$, which facilitates the transition from the initial set of grouped equations defined in (5.3) to the newly structured system, is characterized by the following notation:

$$\begin{bmatrix} V_L \\ V_E \\ \dot{\theta}_1 \\ \dot{\theta}_2 \end{bmatrix} = \underbrace{\begin{bmatrix} I_6 - A^* Ad_{g12}^{-1} & A^* & 0 & 0 \\ -Ad_{g12}^{-1} & I_6 & 0 & 0 \\ 0 & 0 & I_3 & 0 \\ 0 & 0 & 0 & I_3 \end{bmatrix}}_S \begin{bmatrix} \xi_1 \\ \xi_2 \\ \dot{\theta}_1 \\ \dot{\theta}_2 \end{bmatrix} \tag{5.6}$$

such that $V_L = [\nu_L \ \mu_L]^T \in \mathbb{R}^6$, and $V_E = [\nu_E \ \mu_E]^T \in \mathbb{R}^6$. Noticeably, the locked system is described in the coordinate frame attached to body 1, which serves as a reference, and the shape system in the frame attached to agent 2. In parallel, the RWs coordinate frames remain consistent with the body they belong to.

Afterward, the new dynamics in its matrix form is achieved and observed as

$$\underbrace{\begin{bmatrix} M_L & 0 & 0 & 0 \\ 0 & M_E & 0 & 0 \\ 0 & 0 & M_{\theta_1} & 0 \\ 0 & 0 & 0 & M_{\theta_2} \end{bmatrix}}_{M^*(g_{12})} \underbrace{\begin{bmatrix} \dot{V}_L \\ \dot{V}_E \\ \ddot{\theta}_1 \\ \ddot{\theta}_2 \end{bmatrix}}_{\dot{C}^*(g_{12}, \dot{g}_{12})} + \underbrace{\begin{bmatrix} C_{LL} & C_{LE} & C_{L\theta_1} & C_{L\theta_2} \\ C_{EL} & C_{EE} & C_{E\theta_1} & C_{E\theta_2} \\ -C_{L\theta_1}^T & -C_{E\theta_1}^T & C_{\theta_1} & 0 \\ -C_{L\theta_2}^T & -C_{E\theta_2}^T & 0 & C_{\theta_2} \end{bmatrix}}_{C^*(g_{12}, \dot{g}_{12})} \underbrace{\begin{bmatrix} V_L \\ V_E \\ \dot{\theta}_1 \\ \dot{\theta}_2 \end{bmatrix}}_{\dot{C}^*(g_{12}, \dot{g}_{12})} = \begin{bmatrix} F_L \\ F_E \\ \tau_{w_1} - \Lambda^T \tau_1 \\ \tau_{w_2} - \Lambda^T \tau_2 \end{bmatrix}. \quad (5.7)$$

As it can be noted, the mathematical form of the two new systems resembles that of a single agent. Moreover, the block-diagonal property of the total inertia matrix $M^*(g_{12})$ holds, and the couplings in the total CC matrix $C^*(g_{12}, \dot{g}_{12})$ are consistent with the form highlighted in equation (4.8), enabling a straight-forward controller design.

Afterward, the new matrices are extensively computed through the following equations:

$$\begin{cases} M^* = S^{-T} M_{1,2} S^{-1} \\ C^* = S^{-T} C_{1,2} S^{-1} + S^{-T} M_{1,2} \frac{d}{dt} S^{-1} \end{cases} \quad (5.8)$$

where the matrix S is defined in equation (5.6), and $M_{1,2}, C_{1,2}$ in equation (5.3). Upon performing the necessary calculations, the overall inertia matrix is expressed as

$$M^*(q) = \begin{bmatrix} M_1 + \hat{M}_2 & 0 & 0 & 0 \\ 0 & \hat{M}_{tot}^{-1}(\hat{M}_1 M_2) & 0 & 0 \\ 0 & 0 & A_1^T I_{w1}(A_1 - \Lambda_1) & 0 \\ 0 & 0 & 0 & A_2^T I_{w2}(A_2 - \Lambda_2) \end{bmatrix}.$$

Hence, the inertia of the locked system simply equals the sum of those of the two agents, while, the shape system, describing the relative motion between system 1 and 2, is characterized by a reduced inertia form. Those of the RWs are not affected by the transformation.

Finally, the mathematical steps required to solve the updated Coriolis matrix reserve some complexities, due to the presence of the S -matrix time derivative. Indeed, the formulation (5.6) is time-dependent on account of the inclusion of the big adjoint operators.

Therefore, its derivative is computed as

$$\dot{S} = \begin{bmatrix} -\frac{d}{dt}(A^* Ad_{g12}^{-1}) & \frac{d}{dt} A^* & 0 & 0 \\ -\frac{d}{dt}(Ad_{g12}^{-1}) & 0 & 0 & 0 \\ 0 & 0 & 0 & 0 \\ 0 & 0 & 0 & 0 \end{bmatrix}.$$

Specifically, it is important to recall the following relationship:

$$\frac{d}{dt}Y^{-1} = -Y^{-1}\dot{Y}Y^{-1} \quad (5.9)$$

where Y is a square matrix. Thus, the big adjoint derivative is obtained by applying the definition (3.4). Additionally, the term A^* , introduced in equation (5.5), is derived as follows:

$$\begin{aligned} \frac{d}{dt}A^* &= \frac{d}{dt}(M_{tot}^{-1})Ad_{g12}^{-T}M_2 + M_{tot}^{-1}\frac{d}{dt}(Ad_{g12}^{-T}M_2) \\ &= -(M_{tot}^{-1}\dot{M}_{tot}M_{tot}^{-1})Ad_{g12}^{-T}M_2 - M_{tot}^{-1}Ad_{g12}^{-T}ad_{v12}^TM_2, \end{aligned}$$

where finally:

$$\dot{M}_{tot} = -Ad_{g12}^{-T}(ad_{v12}^TM_2 + M_2ad_{v12})Ad_{g12}^{-1}.$$

Hence, the problem statement investigated by [27] is successfully extended to the case study of two multibody systems. Furthermore, as it will be demonstrated in the following chapter, this formulation is tailored for testing the relative dynamics in on-ground validation environments. Specifically, it requires the real-time computer of the simulator to integrate only two dynamics simultaneously, namely the locked and shape motions. This results in a reduced computational cost compared to the relative dynamics previously implemented on the OOS-SIM, which required the integration of four different dynamics: the nominal and controlled motions for both the servicer and the client [1].

5.4. Stability of the locked and shape systems

To assess the stability of the system, defined in equation (5.7), the Lyapunov method is once again selected. Hence, the Lyapunov candidate function is expressed as the total energy of the four sub-systems constituting the dynamics. Namely,

$$\begin{aligned} W &= \frac{1}{2}V_L^T M_L V_L + \frac{1}{2}V_E^T M_E V_E + \frac{1}{2}\dot{\theta}_1^T M_{\theta_1} \dot{\theta}_1 + \frac{1}{2}\dot{\theta}_2^T M_{\theta_2} \dot{\theta}_2 + \frac{1}{2}tr(K_p^E(I_3 - R_{e_E})) \\ &\quad + \frac{1}{2}tr(K_p^L(I_3 - R_{e_L})) + \frac{1}{2}\Delta x_L^T K_p^L \Delta x_L + \frac{1}{2}\Delta x_E^T K_p^E \Delta x_E \end{aligned}$$

where Δx_L is computed with respect to the inertial frame, and Δx_E in the master frame. The candidate's time-derivative is then calculated as

$$\begin{aligned}\dot{W} = & V_L^T M_L \dot{V}_L + V_E^T M_E \dot{V}_E + \dot{\theta}_1^T M_{\theta_1} \ddot{\theta}_1 + \dot{\theta}_2^T M_{\theta_2} \ddot{\theta}_2 + (skew(K_p^E R_{e_E}))^T \omega_E \\ & + (skew(K_p^L R_{e_L}))^T \omega_L + \Delta x_L^T K_p^L R_1^T \mathbf{v}_L + \Delta x_E^T K_p^E R_{21} \mathbf{v}_E.\end{aligned}$$

This function can be rewritten by redefining the potentials in a compact form, as following:

$$\begin{aligned}\dot{W} = & V_L^T M_L \dot{V}_L + V_E^T M_E \dot{V}_E + \dot{\theta}_1^T M_{\theta_1} \ddot{\theta}_1 + \dot{\theta}_2^T M_{\theta_2} \ddot{\theta}_2 \\ & + \begin{bmatrix} (R_1 K_p^L \Delta x_L)^T & \gamma_L^T \end{bmatrix} \begin{bmatrix} \mathbf{v}_L \\ \omega_L \end{bmatrix} + \begin{bmatrix} (R_{21}^T K_p^E \Delta x_E)^T & \gamma_E^T \end{bmatrix} \begin{bmatrix} \mathbf{v}_E \\ \omega_E \end{bmatrix}.\end{aligned}$$

Hence, by employing equations (5.6) and (4.5), the angular velocities ω_L , ω_E are expressed as functions of μ_1 , μ_2 and $\dot{\theta}_1$, $\dot{\theta}_2$. Consequently, the Lyapunov derivative becomes:

$$\begin{aligned}\dot{W} = & V_L^T M_L \dot{V}_L + V_E^T M_E \dot{V}_E + \dot{\theta}_1^T M_{\theta_1} \ddot{\theta}_1 + \dot{\theta}_2^T M_{\theta_2} \ddot{\theta}_2 \\ & + \begin{bmatrix} (R_1 K_p^L \Delta x_L)^T & \gamma_L^T \end{bmatrix} \left[(I_6 - A^* A d_{g_{12}}^{-1}) \begin{bmatrix} \mathbf{v}_1 \\ \mu_1 - \Lambda_1 \dot{\theta}_1 \end{bmatrix} + A^* \begin{bmatrix} \mathbf{v}_2 \\ \mu_2 - \Lambda_2 \dot{\theta}_2 \end{bmatrix} \right] \\ & + \begin{bmatrix} (R_{21}^T K_p^E \Delta x_E)^T & \gamma_E^T \end{bmatrix} \left[-A d_{g_{12}}^{-1} \begin{bmatrix} \mathbf{v}_1 \\ \mu_1 - \Lambda_1 \dot{\theta}_1 \end{bmatrix} + \begin{bmatrix} \mathbf{v}_2 \\ \mu_2 - \Lambda_2 \dot{\theta}_2 \end{bmatrix} \right].\end{aligned}$$

Thus, a step of calculations leads to the following form:

$$\begin{aligned}\dot{W} = & V_L^T M_L \dot{V}_L + V_E^T M_E \dot{V}_E + \dot{\theta}_1^T M_{\theta_1} \ddot{\theta}_1 + \dot{\theta}_2^T M_{\theta_2} \ddot{\theta}_2 \\ & + \begin{bmatrix} (R_1 K_p^L \Delta x_L)^T & \gamma_L^T \end{bmatrix} \begin{bmatrix} \mathbf{v}_L - \eta_1 \Lambda_1 \dot{\theta}_1 - \eta_2 \Lambda_2 \dot{\theta}_2 \\ \mu_L - \eta_3 \Lambda_1 \dot{\theta}_1 - \eta_4 \Lambda_2 \dot{\theta}_2 \end{bmatrix} \\ & + \begin{bmatrix} (R_{21}^T K_p^E \Delta x_E)^T & \gamma_E^T \end{bmatrix} \begin{bmatrix} \mathbf{v}_E + [p_{21}]_x R_{21} \Lambda_1 \dot{\theta}_1 \\ \mu_E + R_{21} \Lambda_1 \dot{\theta}_1 - \Lambda_2 \dot{\theta}_2 \end{bmatrix}\end{aligned}$$

where $\eta_{1:4}$ are parameters obtained from the proposed derivation. Thus, the three control methods, introduced in section 4.2, are briefly presented again, and adapted to the current scenario.

5.4.1. Coordinated control

The error can be directly defined by the pose difference, through the exploitation of the notation proposed in [38]. Hence, the achieved form is the following:

$$g_{des}^{-1} g_b = \underbrace{(R_{des}^T(p_b - p_{des}),}_{r_b} \underbrace{R_{des}^T R_b)}_{R_{e_b}}$$

where the positions are expressed with respect to the inertial frame. Moreover, it is important to notice that the pose error of the locked system is simply expressed as the error of the reference system, in this case, frame 1, with respect to a desired position and orientation. Thus:

$$r_L = R_{des_1}^T(p_1 - p_{des_1}) ; \quad R_{e_L} = R_{des_1}^T R_1.$$

Particularly, since the RWs do not affect the translation of the multibody systems, the control strategy for the system's linear motion is consistent across all three proposed methods, that are here addressed.

1. Free-floating control

Exploring the scenario of two satellites moving in space, the simple free-floating control has little practical application. Nevertheless, its development is proposed as it serves as a first step toward the subsequent, more nuanced approaches. Considering the absence of initial angular momentum for the two agents, both angular momentum-based velocities μ_1 and μ_2 are null. As a consequence, the formulation of the control law remains similar to what is presented for a single multibody system. The torque control, integrating the inertia shaping approach (presented in detail in section 4.2.2) for both sets of RWs, is therefore defined as

$$\begin{cases} \tau_{w_1} = -K_d^1 \dot{\theta}_1 - R_{21}^T \gamma_E + \eta_3^T \gamma_L - (R_{21}^T [p_{21}]_x^T)(R_{21}^T K_p^E \Delta x_E) + \eta_1^T (R_1 K_p^L \Delta x_L) \\ \tau_{w_2} = -K_d^2 \dot{\theta}_2 + \gamma_E + \eta_4^T \gamma_L + \eta_2^T (R_1 K_p^L \Delta x_L). \end{cases} \quad (5.10)$$

Whereas, the linear control is designed as follows:

$$\begin{cases} f_L = -\bar{K}_d^L v_L - R_{e_L}^T \bar{K}_p^L r_L \\ f_e = -\bar{K}_d^E v_E - R_{e_E}^T \bar{K}_p^E r_E \end{cases}$$

where the terms K_d and K_p indicate positive derivative and proportional gains, respectively, and the angular potentials of the locked and shape systems, (γ_L, γ_E) , are computed

as in equation (4.11). The stability in the sense of Lyapunov is then verified by simply following the steps presented for the single multibody system, in section 4.2.1.

2. Free-flying control

Henceforth, both thrusters and RWs are actuated for the attitude control of the spacecraft. Therefore, stability is achieved by applying the following control laws, gathering both linear and angular contributions:

$$\left\{ \begin{array}{l} F_L = \begin{bmatrix} f_L \\ \tau_L \end{bmatrix} = \begin{bmatrix} -\bar{K}_d^L \mathbf{v}_L - R_{e_L}^T \bar{K}_p^L r_L \\ -K_d^L \boldsymbol{\mu}_L - (\text{skew}(K_p^L R_{e_L})^\vee)^T + Q_{L\theta_1} \dot{\theta}_1 + Q_{L\theta_2} \dot{\theta}_2 \end{bmatrix} + C_{LE} V_E \\ F_E = \begin{bmatrix} f_E \\ \tau_E \end{bmatrix} = \begin{bmatrix} -\bar{K}_d^E \mathbf{v}_E - R_{e_E}^T \bar{K}_p^E r_E \\ -K_d^E \boldsymbol{\mu}_E - (\text{skew}(K_p^E R_{e_E})^\vee)^T + Q_{E\theta_1} \dot{\theta}_1 + Q_{E\theta_2} \dot{\theta}_2 \end{bmatrix} + C_{EL} V_L \\ \tau_{w_1} = -K_d^1 \dot{\theta}_1 - R_{21}^T \gamma_E + \eta_3^T \gamma_L + \Lambda_1 C_{\theta_1 L} V_L + \Lambda_1 C_{\theta_1 E} V_E + \Lambda_1 C_{\theta_1} \dot{\theta}_1 \\ \quad - (R_{21}^T [p_{21}]_x^T) (R_{21}^T K_p^E \Delta x_E) + \eta_1^T (R_1 K_p^L \Delta x_L) \\ \tau_{w_2} = -K_d^2 \dot{\theta}_2 + \gamma_E + \eta_4^T \gamma_L + \Lambda_2 C_{\theta_2 L} V_L + \Lambda_2 C_{\theta_2 E} V_E + \Lambda_2 C_{\theta_2} \dot{\theta}_2 + \eta_2^T (R_1 K_p^L \Delta x_L). \end{array} \right. \quad (5.11)$$

In particular, the notation $Q \in \mathbb{R}^{3 \times 3}$ indicates the angular part of the CC couplings $C \in \mathbb{R}^{6 \times 3}$, between the artificial systems and the two sets of RWs. Noticeably, the force feedforward (FF) terms, constituted by the passive couplings between the locked and shape systems, are introduced in the controller. In parallel, the couplings between the new systems and the two RWs are needed to maintain the advantages of IS in the rotors' actuation. Hence, the controller becomes an augmented PD, or PD+, where the couplings pre-compensate for expected centrifugal/Coriolis effects [35].

3. Hierarchical control

As presented in detail in section 4.2, the hierarchical approach is based on two main tasks, each associated with its respective new Lyapunov function. The first part of the control involves thrusters to nullify the total momentum of the system, thus making it static. The second subset is designed to cancel the pose errors and ensure stability in the new desired configuration.

The first Lyapunov candidate is expressed as the angular kinetic energy of the controlled systems:

$$W_1 = \frac{1}{2} \boldsymbol{\mu}_L^T M_L \boldsymbol{\mu}_L + \frac{1}{2} \boldsymbol{\mu}_E^T M_E \boldsymbol{\mu}_E$$

whose derivative is computed as

$$\dot{W}_1 = \boldsymbol{\mu}_L^T M_L \dot{\boldsymbol{\mu}}_L + \boldsymbol{\mu}_E^T M_E \dot{\boldsymbol{\mu}}_E.$$

Hence, since the locked and shape systems are coupled with each other and with each of the two sets of RWs, the control law required to cancel the overall momentum is:

$$\begin{cases} F_L = \begin{bmatrix} f_L \\ \boldsymbol{\tau}_L \end{bmatrix} = \begin{bmatrix} -\bar{K}_d^{L_l} \boldsymbol{v}_L - R_{e_L}^T \bar{K}_p^L r_L \\ -K_d^L \boldsymbol{\mu}_L + Q_{L\theta_1} \dot{\boldsymbol{\theta}}_1 + Q_{L\theta_2} \dot{\boldsymbol{\theta}}_2 \end{bmatrix} + C_{LE} V_E \\ F_E = \begin{bmatrix} f_E \\ \boldsymbol{\tau}_E \end{bmatrix} = \begin{bmatrix} -\bar{K}_d^{E_l} \boldsymbol{v}_E - R_{e_E}^T \bar{K}_p^E r_E \\ -K_d^E \boldsymbol{\mu}_E + Q_{E\theta_1} \dot{\boldsymbol{\theta}}_1 + Q_{E\theta_2} \dot{\boldsymbol{\theta}}_2 \end{bmatrix} + C_{EL} V_L. \end{cases}$$

As a consequence of the completion of the first control tasks, the momentum-linked angular velocities of locked and shape systems are null. Thus, the second Lyapunov function is presented:

$$W_2 = \frac{1}{2} \dot{\boldsymbol{\theta}}_1^T M_{\theta_1} \dot{\boldsymbol{\theta}}_1 + \frac{1}{2} \dot{\boldsymbol{\theta}}_2^T M_{\theta_2} \dot{\boldsymbol{\theta}}_2 + \frac{1}{2} \text{tr}(K_p^E(I_3 - R_{e_E})) + \frac{1}{2} \text{tr}(K_p^L(I_3 - R_{e_L})) M_{\theta_2} \dot{\boldsymbol{\theta}}_2$$

whose derivative is defined as

$$\dot{W}_2 = \dot{\boldsymbol{\theta}}_1^T M_{\theta_1} \ddot{\boldsymbol{\theta}}_1 + \dot{\boldsymbol{\theta}}_2^T M_{\theta_2} \ddot{\boldsymbol{\theta}}_2 + (\text{skew}(K_p^E R_{e_E})^\vee)^T \boldsymbol{\omega}_E + (\text{skew}(K_p^L R_{e_L})^\vee)^T \boldsymbol{\omega}_L.$$

Once again, IS is freely applied. Consequently, the RWs control torques are designed following the same formulation as the free-floating approach. This implies that the set of equations (5.10) can be employed to achieve the cancellation of the attitude errors.

5.4.2. Comments on the proposed control methods

The introduction of the FF terms in the controller that regulates the thrusters actuation significantly enhances the overall robustness of the control system. In parallel, the inertia-shaped RWs control provides a fundamental torque contribution, for accuracy purposes. However, it should be noted that FF and IS are normally in contrast to each other [39], representing two different methods to deal with couplings: either in the closed-loop dynamics (FF) or in the control law (IS) [35]. Nevertheless, the proposed dynamics formulation allows to apply simultaneously FF and IS, to two different sets of actuators.

Therefore, both the advantages of the two methods, namely robustness provided by FF and flexibility by IS, are exploited.

Hence, all the three proposed control methods, whose differences are outlined in section 4.2.5, offer the possibility to precisely command the internal group formation and the overall group maneuver both independently and synchronously. This feature offers numerous advantages, providing adaptability to a wide range of applications and sets of achievable configurations.

Particularly, in the case one of the two artificial systems is uncontrolled, its errors are undefined, thus treated as zero. Consider the scenario involving the docking between systems 1 and 2, in which the total group maneuver is not a concern: only the internal group shape is then governed. The null pose error of the locked system greatly simplifies the control laws by canceling all its potentials from the Lyapunov function. Moreover, its kinetic energy is removed from the candidate formulation, hence the locked forces and torques are not designed. As a consequence, the RWs torques must include the inertia-shaped couplings with the locked system, which are not canceled with their opposite transpose anymore.

Once the control is designed, a transformation that allows for a controlled redistribution of the forces between the multibody systems 1 and 2 is introduced. For instance, the required space gap for a successful docking maneuver can be bridged entirely by one of the systems, or actively by both, with an infinite number of solutions. Thus, the proposed formulation allows to decide on the proportion in which the multibodies should participate in the control of the relative motion. Once the desired proportion is set, the actuated forces are transformed back to the locked and shape states, and sent to the system's dynamics calculator: specifically, to the velocity integrator.

Particularly, the benefits of the FF term in terms of controller robustness are shown in Figure 5.1, which presents the results obtained with the use of the free-flying controller in continuous time. This means that the simulation is performed without the presence of discretization, generally introduced by the thrusters model. The proposed approach allows the observation of the pure convergence of the relative and total errors, in the presence of an initial momentum in both the locked and shape systems. Moreover, the contribution offered by the inertia-shaped RWs is presented in Figure 5.2.

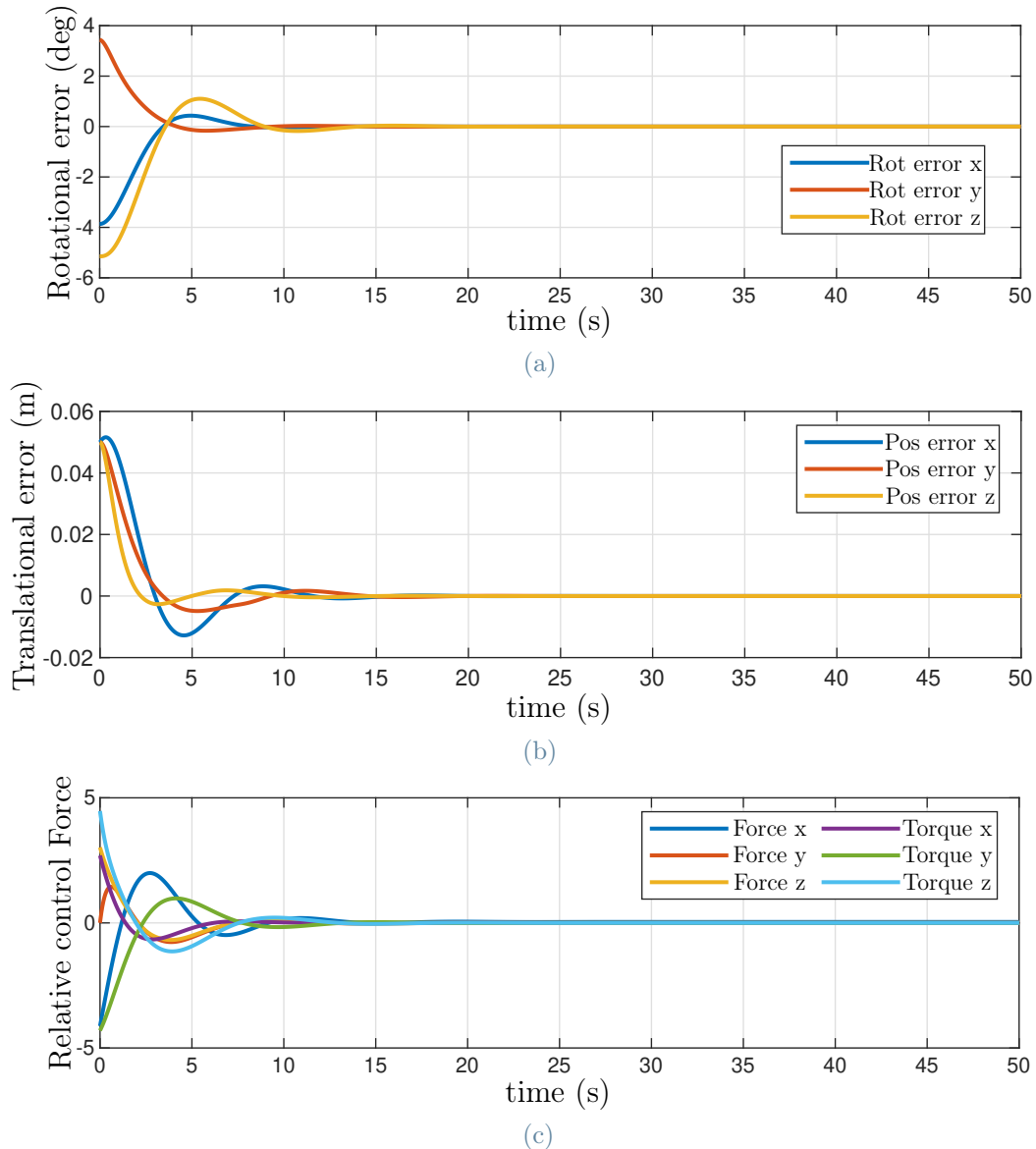


Figure 5.1: Relative control results in continuous time (free-flying case): rotational error (a), translational error (b), and continuos-time control forces and torques (c).

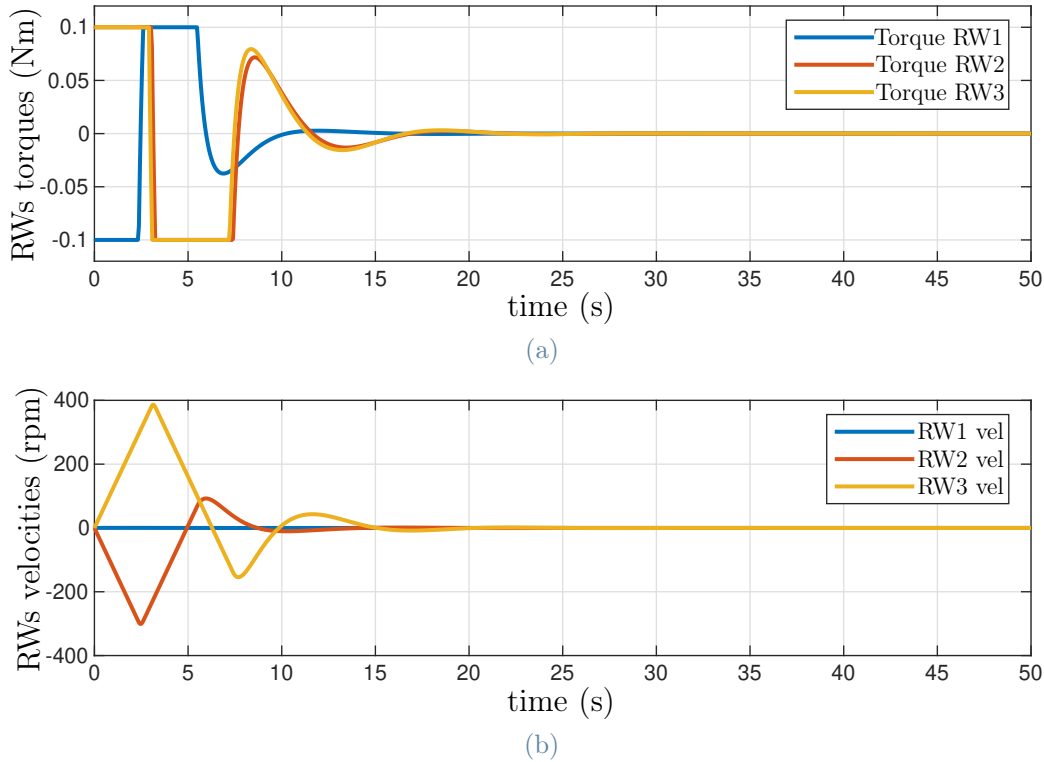


Figure 5.2: Relative control results in continuous time (free-flying case): RWs torques (a), and velocities (b).

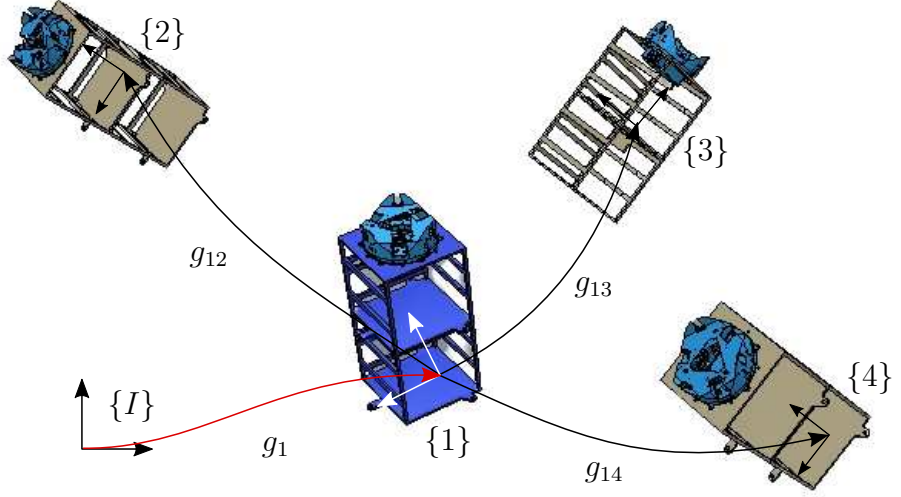


Figure 5.3: Flight formation between multiple fixed-inertia multibody satellites.

5.5. Formation flying principles

The proposed dynamics can be expanded to n multibody systems in a centralized controlled fashion. Figure 6.6 illustrates the group formation of multibody satellites, with $\{1\}$ as the master frame, defining the locked configuration, and g_{1i} denoting the shape for each satellite. Consider their single motion, expressed as

$$M_i(g_i) \begin{bmatrix} \dot{\mathbf{v}}_i \\ \dot{\boldsymbol{\mu}}_i \\ \dot{\boldsymbol{\theta}}_i \end{bmatrix} + C_i(g_i, \dot{g}_i) \begin{bmatrix} \mathbf{v}_i \\ \boldsymbol{\mu}_i \\ \boldsymbol{\theta}_i \end{bmatrix} = \begin{bmatrix} f_i \\ \boldsymbol{\tau}_i \\ \boldsymbol{\tau}_{w_i} - \boldsymbol{\Lambda}^T \boldsymbol{\tau}_i \end{bmatrix} \quad \forall i = 1 : n. \quad (5.12)$$

The new artificial total and shape velocities are defined in the following way:

$$\begin{cases} V_L = \boldsymbol{\xi}_1 + \sum_{i=1}^n M_{tot}^{-1} A d_{g_{1i}}^{-T} M_i V_{E_{i-1}} = (I - \sum_{i=2}^n A_i^* A d_{g_{1i}}^{-1}) \boldsymbol{\xi}_1 + \sum_{i=2}^n A_i^* \boldsymbol{\xi}_i \\ V_{E_{i-1}} = \boldsymbol{\xi}_i - A d_{g_{1i}}^{-1} \boldsymbol{\xi}_1. \end{cases}$$

where $A_i^* = M_{tot}^{-1} A d_{g_{1i}}^{-T} M_i$. In the proposed formulation, system 1 behaves as a reference for all the other agents. Thus, the total locked dynamics is derived in its frame, and $n - 1$ internal group shape systems can be controlled. Therefore, the transformation from the

initial state to the artificial one occurs as follows:

$$\begin{bmatrix} V_L \\ V_{E_1} \\ V_{E_2} \\ \vdots \\ V_{E_{n-1}} \end{bmatrix} = \underbrace{\begin{bmatrix} I - \sum_{i=2}^n A_i^* A d_{g_{1i}}^{-1} & A_2^* & A_3^* & \dots & A_n^* \\ -A d_{g_{12}}^{-1} & I & 0 & \dots & 0 \\ -A d_{g_{13}}^{-1} & 0 & I & \dots & 0 \\ \vdots & \vdots & & \ddots & \\ -A d_{g_{1n}}^{-1} & 0 & 0 & \dots & I \end{bmatrix}}_S \begin{bmatrix} \xi_1 \\ \xi_2 \\ \xi_3 \\ \vdots \\ \xi_n \end{bmatrix} \quad (5.13)$$

Noticeably, if only two systems are considered, i.e. $n = 2$, the set of equations derived in (5.6) is matched. The total dynamics is then computed consistently with what is expressed in equation (5.8), and a linear extension of the control methods exposed in section 5.4.1 can be performed. As a result, the proposed dynamics and control of n systems can be exploited to operate a flight formation control of a fleet of free-flying robots.

6 | HIL experimental validation on the OOS-SIM

6.1. Validation of the absolute dynamics

This first section presents the results obtained from the experiments concerning the integration and validation of the single multibody dynamics and its related free-flying control, discussed in Chapter 4. Particularly, it represented the first time thrusters and RWs models were tested on the OOS-SIM.

6.1.1. Set-up of the experiment

The OOS-SIM client satellite is chosen for testing the system in an absolute dynamics condition. This decision is taken considering that the client is equipped with a FTS, which allows for feedback measurements on applied external forces. Hence, the control is tested for both moving the satellite to a new configuration and assessing the robustness of the control, under the exertion of external stresses.

The dynamics of the system is implemented on the model that is read by the real-time computer of the OOS-SIM facility and is computed through an internal dynamics calculator of DLR, called LucaDynamics. This tool is a compact Matlab library that computes the rigid body quantities, i.e. the inertia and Coriolis matrices of a given system. In this scenario, LucaDynamics relies on the Unified Robot Description Format (URDF) file extracted from CoppeliaSim, describing a representative model of the satellite and its actuators. Moreover, the velocity calculated in the frame attached to the body is integrated and used as a feedback signal for the dynamics calculator. It should be noticed that the dynamics obtained via this tool truthfully reflects the behavior of the continuous-time equations derived by hand, previously presented in the thesis. The necessary mathematical steps to achieve the final form of the dynamics characterized by the block-diagonal inertia matrix are then manually integrated in Simulink.

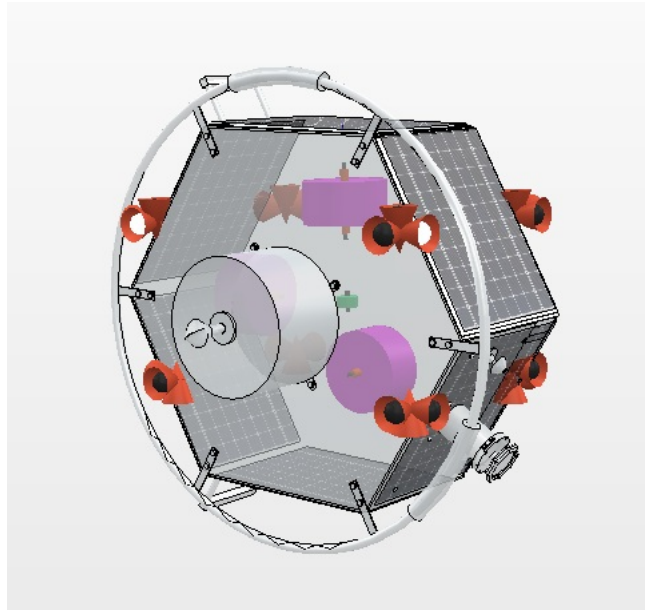


Figure 6.1: CoppeliaSim simulation environment synchronized with the HIL experiment, showing the client satellite.

Once again, the correct implementation of the whole system is verified through the conservation of the total momentum in the inertial frame and kinetic energy, under the absence of external forces. Specifically, the external forces can be applied on the OOS-SIM through a dedicated rope that, when pulled, enables an almost-pure translation of the client satellite on the negative z -axis.

Simultaneously with the activation of the OOS-SIM, a simulation is launched in CoppeliaSim, receiving real-time data from the Simulink model, based on the pose calculation of the robotic facility. In fact, the model commands the position of the industrial robot, which returns the real-time pose of its end-effector, together with the forces and torques sensed by the FTS. This allows to bridge the gap between software and hardware, ensuring an effective HIL simulation.

The CoppeliaSim simulation gives visual feedback on the presence and activation of the satellite actuators, becoming of fundamental importance in the comprehensive understanding of the multibody dynamics experiment. In particular, as it can be noted in Figure 6.1, the simulation software served as a graphic representation tool for the satellite motion, the speed of the RWs (highlighted in purple), and the firing of the thrusters (represented by the set of red lights).

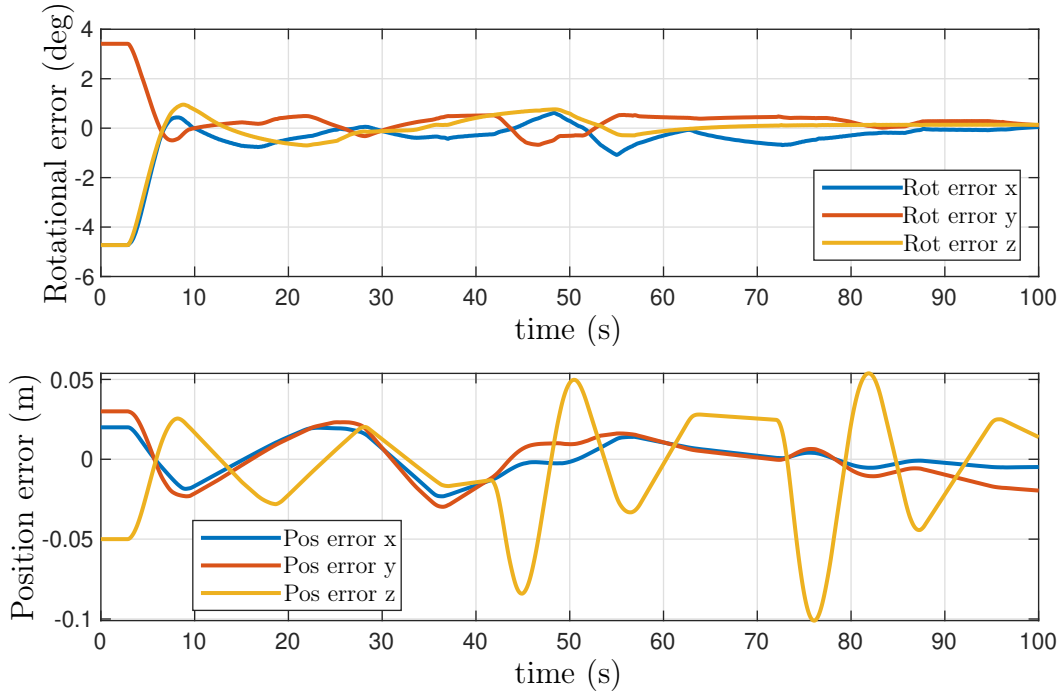


Figure 6.2: Rotational (top) and translational (bottom) errors over time, obtained from the HIL experiment.

6.1.2. Experiment development and results

The client is initially commanded to a new pose, denoted by a displacement of roughly 2.5 cm on the x and y axes, and of 5 cm on z , plus an angle offset $\delta\phi = [-5, 3.5, -5]\text{ deg}$. Furthermore, once the equilibrium position is achieved, the satellite receives two prompts from an external negative force along the z -axis, of about 10 N and 20 N , respectively. Following, the most relevant data extracted from the experiment.

Figure 6.2 demonstrates the stability of the system through the convergence of angular

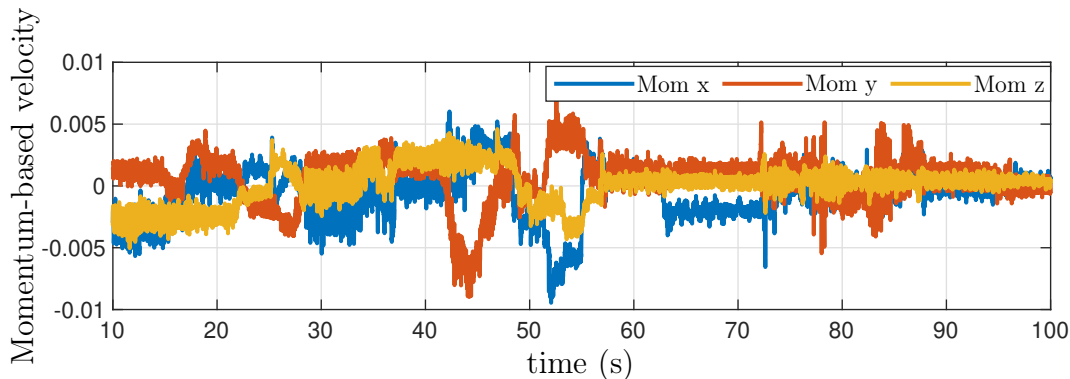


Figure 6.3: Total momentum over time, obtained from the HIL experiment.

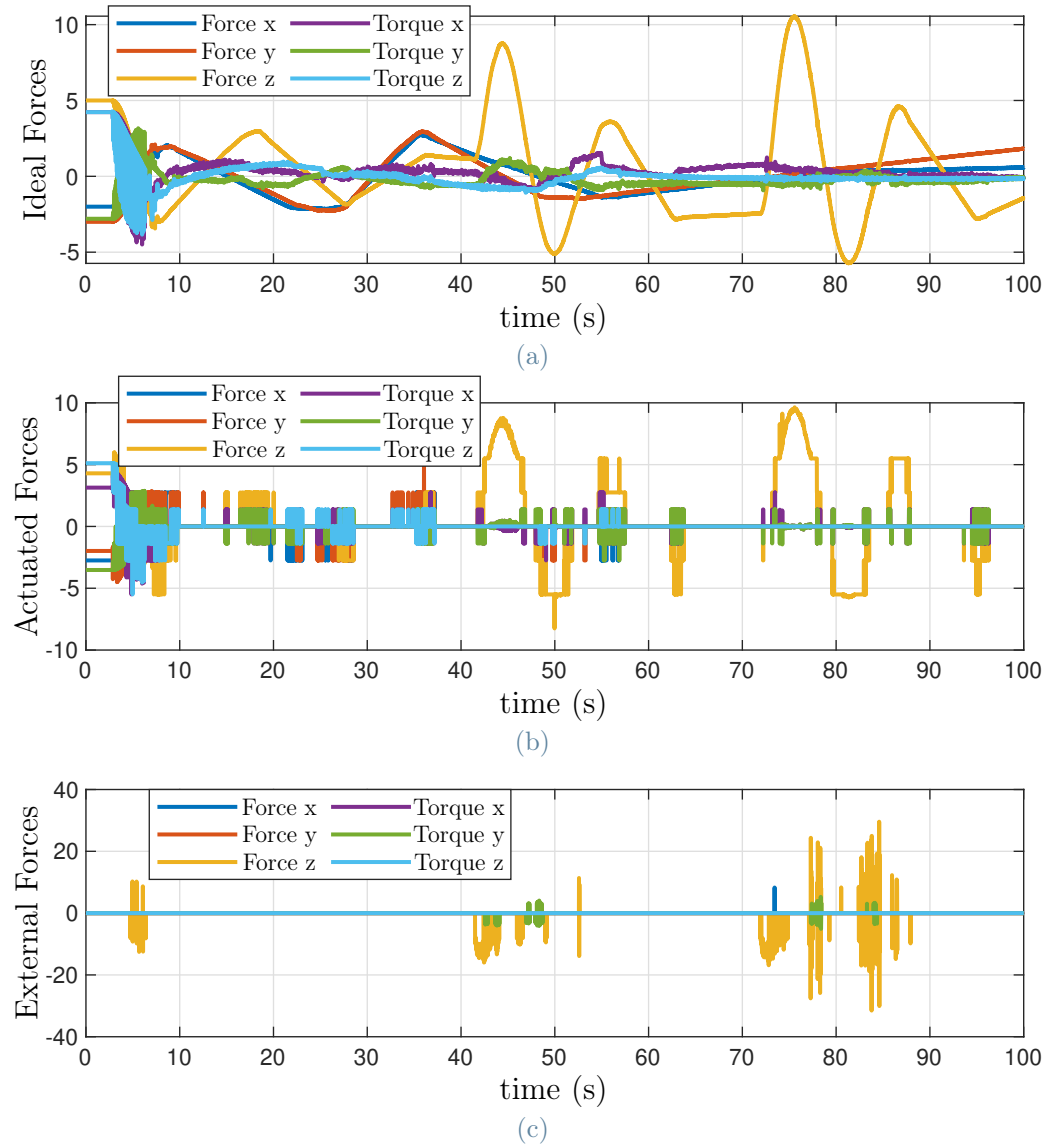


Figure 6.4: Forces ideal (a), actuated by the thrusters (b), and external (c) over time, obtained from the HIL experiment.

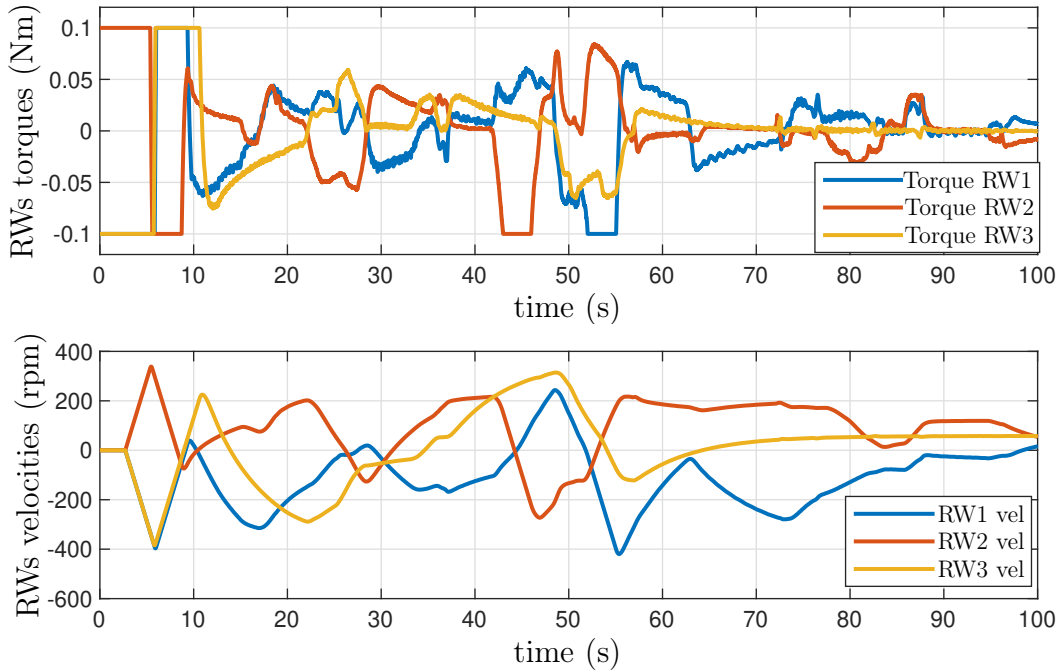


Figure 6.5: RWs torques (top), and velocities (bottom) over time, obtained from the HIL experiment.

and linear errors. A direct result of the applied external force is observed in the satellite's z -axis displacement, by the two distinct negative peaks. The experiment concluded successfully, achieving a precision of approximately half a degree for rotational control and two centimeters for translational control, as evident in the graphs within the figure. Moreover, Figure 6.3 illustrates the trend of the rotational velocity μ , derived in equation (4.5), therefore, of the momentum of the system. Due to the presence of control and external forces, the angular momentum of the system is naturally not conserved during the experiment. In contrast, the satellite actuators effectively minimize its value, bringing it close to zero and enabling the system to achieve a stable condition. The main forces involved in the experiment are shown in Figure 6.4. The top section represents the forces ideally generated by the controller, the middle section shows the forces generated by the thruster model, and the bottom one illustrates the external forces. Notably, the two disturbances mentioned earlier occur at approximately 45 s and 80 s. Lastly, Figure 6.5 displays the contribution of the RWs on the control of the system's attitude. In this free-flying control scenario, their use is only complementary to the thrusters, in fact, their maximum achieved speed is approximately 400 rpm. Nonetheless, the torques exerted by them play a crucial role in the achievement of the remarkable angular precision of half a degree.

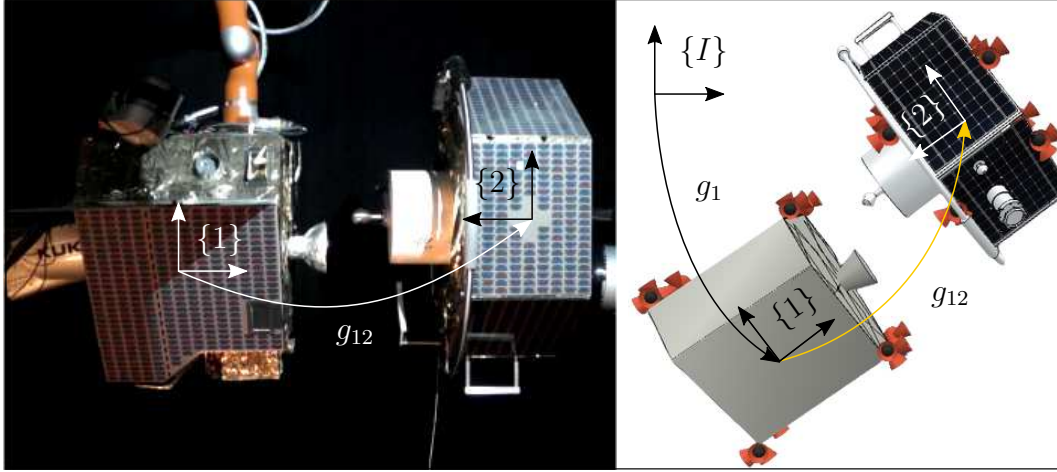


Figure 6.6: The relative motion replicated on the DLR OOS-SIM on the left, and the absolute motion shown in software on the right.

6.2. Validation of the relative dynamics

This section discusses the experiment performed on the OOS-SIM to test the relative dynamics formulation derived in Chapter 5, with its free-flying controller.

6.2.1. Set-up of the experiment and model integration

The simulation scenario involves two orbiting multibody systems. Thus, both the industrial robots of the OOS-SIM take part in the experiment. Particularly, the client satellite is again designated as the master system, representing system 1 in equations (5.6). Accordingly, the servicer satellite operates as system 2. More in detail, the proposed experiment considers two satellites that are synchronously spinning, with the master system executing an approach maneuver toward the other. Therefore, within the two artificial systems (locked and shape), only the motion of the latter is actively controlled. Meanwhile, the locked group, rigidly composed of the two bodies, spins freely without external constraints. Thus, only the master system, i.e. the client satellite, is actuated to perform the required relative dynamics task. Consequently, the motion of the client satellite impacts both the locked and shape systems, whereas the dynamic behavior of the servicer satellite affects only the locked motion.

The Simulink model of the experiment is built into a C++ code and transmitted to the real-time computer of the OOS-SIM. Figure 6.6 illustrates the validation scenario. The locked dynamics is kept in simulation, providing visualization of the total motion through the CoppeliaSim software. Meanwhile, the relative motion is commanded to the

position-controlled industrial robots of the OOS-SIM.

This integration between the simulation model (*software*) and the OOS-SIM (*hardware*) ensures the development of a HIL simulation. Notably, the Simulink model computes simultaneously the dynamics of the two artificial systems and incorporates hardware values to provide consistency between the real and the software motions. The relative pose and relative velocity values obtained from the OOS-SIM robots are transmitted to the controller block of the Simulink model. In parallel, the locked pose and velocity are entirely computed within the simulation. This approach retains the effects that the two artificial systems have on each other, arising from the CC couplings. As a result, the OOS-SIM replicates the relative motion among the two systems, incorporating the influence posed by the locked dynamics. This ensures the physical consistency of the HIL simulation with respect to the real mission behavior, which is accurately represented by the locked motion.

Hence, the block of the simulation model that calculates the dynamics contains two types of integrators. Firstly, the poses of the two satellites in their total motion are computed as

$$g_i = \int_{t_0}^t (g_i V_i^\wedge) dt \quad \forall i = 1, 2$$

where the operator \cdot^\wedge defines the generalized form of the velocity, as in equation (3.2). Moreover, since system 1 acts as the reference, the pose difference is computed in that frame, as $g_{12}(t) = g_1^{-1}g_2$. In parallel, the relative motion is commanded to the OOS-SIM robots as follows:

$$\begin{cases} g_{1_{HW}}(t) = g_{2_{HW}}(t)g_{12}(t)^{-1} \\ g_{2_{HW}}(t) = g_2(0) \end{cases}$$

where $g_{1_{HW}}(t)$ is the motion of the OOS-SIM client, constantly updated through the integration of the simulation model with the hardware measures, and $g_{2_{HW}}(t)$ is the pose of the OOS-SIM servicer, which remains static in the shape system's context. The delta commanded to the OOS-SIM client is then internally transmitted to the inverse kinematics of the industrial robot, which generates a motion in time. Secondly, the total set of velocities, $V_{tot} = [V_L \ V_E \ \dot{\theta}_1 \ \dot{\theta}_2]^T$, is integrated in the following way:

$$V_{tot} = \int_{t_0}^t (M^*)^{-1} (F_{control} - F_{external} - C^* V_{tot}) dt.$$

where C^* and M^* are the CC and inertia matrices, shown in equation (5.7), $F_{control}$ is computed as the relative control components of equation (5.11), and the external forces are sensed by the client FTS. Specifically, while the control force only affects the shape system, the external disturbances influence both the two artificial systems, further demonstrating

the HIL concept.

6.2.2. Experiment development and results

The motion of the two satellites is characterized by a non-zero initial momentum. In particular, they are initialized with a locked velocity of 0.02 rad/s on the y -axis, and a relative velocity of 0.01 m/s on the x -axis and of 0.02 rad/s on the y -axis. In the current experiment, only the relative motion is controlled: a setpoint that is $[5, 2, 2] \text{ cm}$ and $[2, 2, 0] \text{ deg}$ away from the initial pose difference is selected. Therefore, the client satellite is actuated toward the goal of reducing the pose gap with the servicer, resembling the approach action of a docking operation. The hardware experiment shows only this movement, whereas in their complete motion, they are spinning together around the y -axis. Moreover, at time $t = 130 \text{ s}$ and 160 s , two external forces of 10 N and 20 N respectively are applied along the negative z -axis, generating an external torque component acting around the y -axis.

Figure 6.7c shows the presence of two distinct force peaks, with the smaller signals within the plot being attributed to noise. It should be noted that the model is designed to treat all types of forces as internal. This is due to the fact that an on-orbit docking scenario is characterized by the absence of external agents: only the two systems are involved. Consequently, during the HIL experiment, any externally applied force on one body is read as a contact between the two agents, resulting in an equal and opposite force being reflected on the other.

In Figure 6.8 it is possible to observe the total simulated momentum, showing the spinning of the locked system, and the relative momentum, effectively brought to zero by the free-flying controller. The total kinetic energy is also presented. Figure 6.9 illustrates the robustness of the controller in guiding the relative system to a new pose and in promptly reacting to the voluntary displacement introduced twice. As explained above, the control task is entirely carried out by the master system, represented by the client satellite. Accordingly, Figure 6.7a and 6.7b show the force ideally requested by the client and the one it actuates through the use of thrusters, respectively. Particularly, the thruster actuation is heavily discretized. Hence, their nature prevents precise control of the spacecraft, introducing a steady-state error of $\pm 2 \text{ cm}$ in translation. In parallel, the rotational error is again lower than one degree. Figure 6.9 depicts both the errors, while Figure 6.10 shows the RWs key role in achieving attitude precision, in terms of torques and velocities.

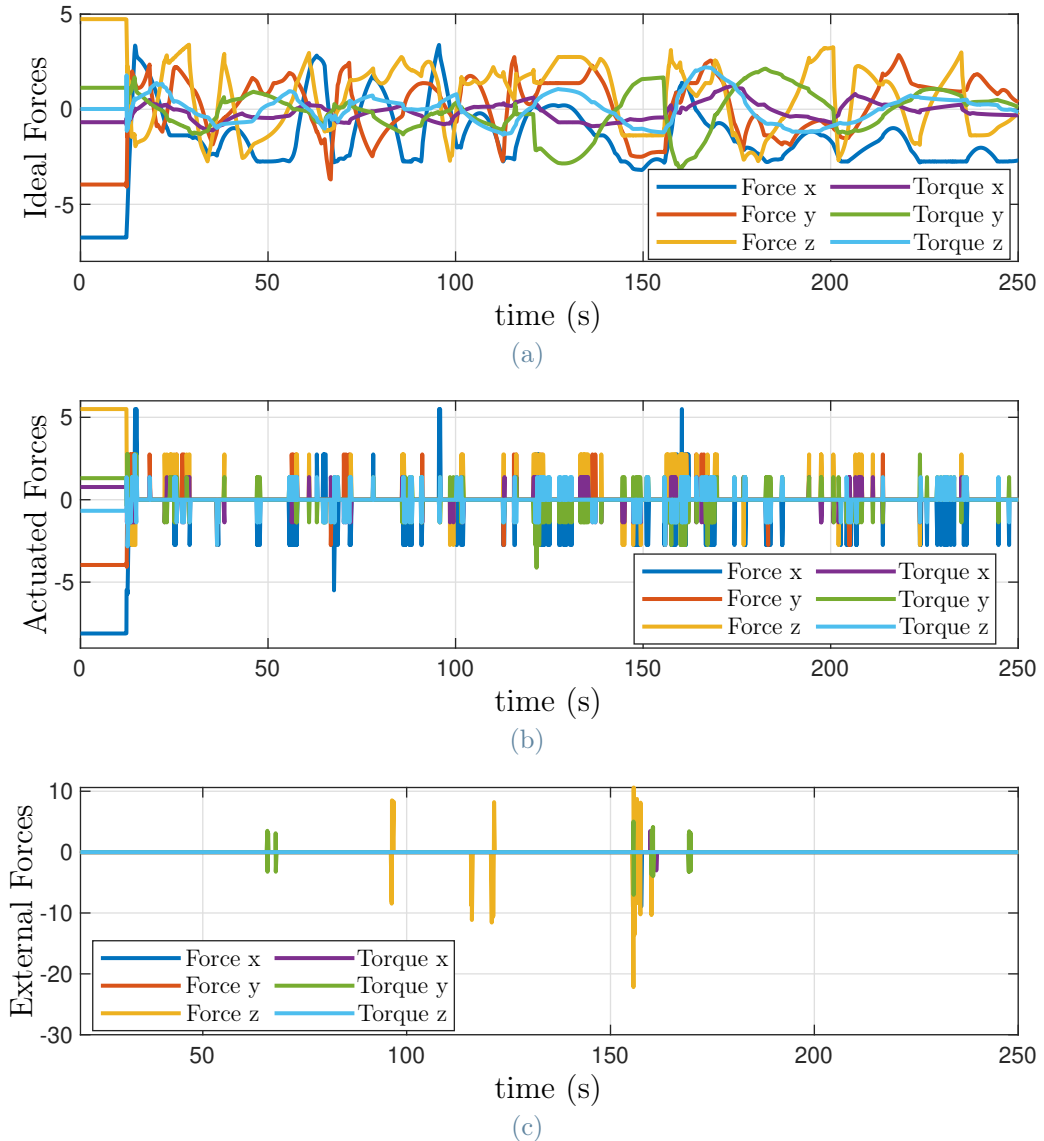


Figure 6.7: Client satellite forces: ideal (a), actuated by the thrusters (b), and external (c) over time, obtained from the HIL experiment.

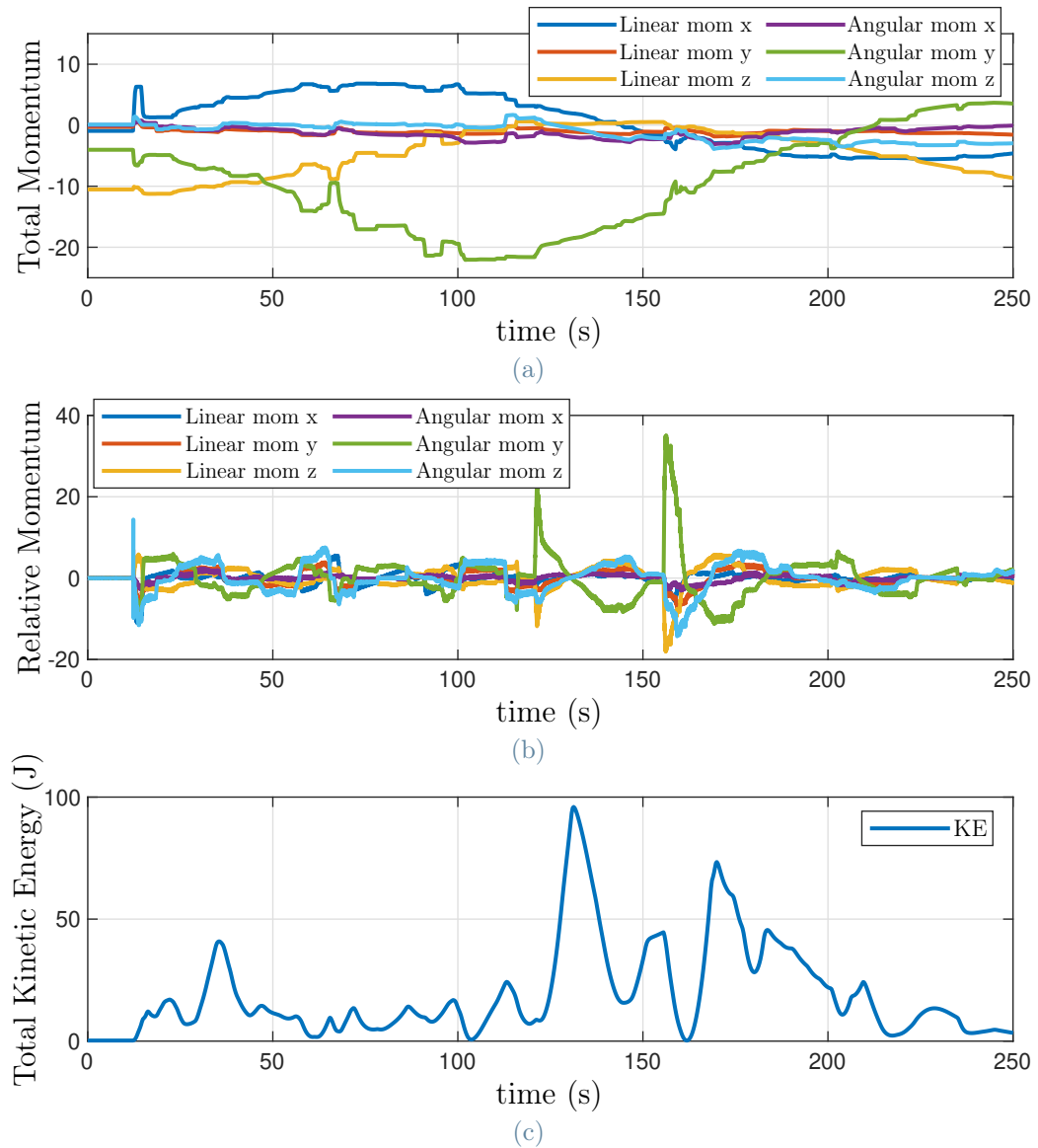


Figure 6.8: Total momentum (a), relative momentum (b), and kinetic energy (c) over time, obtained from the HIL experiment.

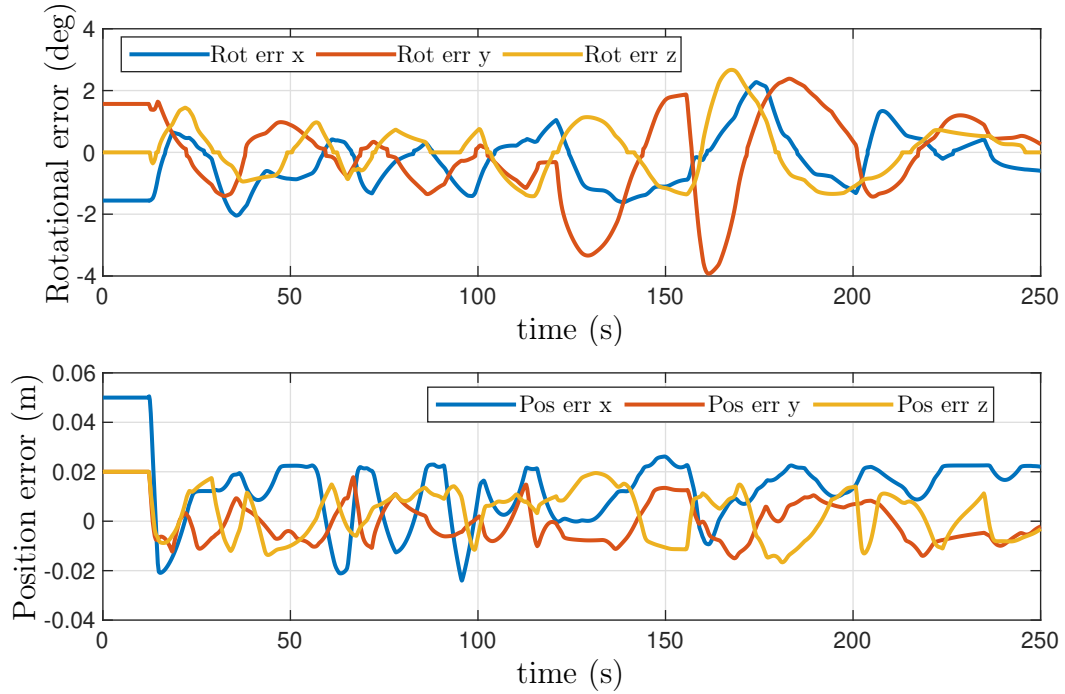


Figure 6.9: Relative rotational (top) and translational (bottom) errors over time, obtained from the HIL experiment.

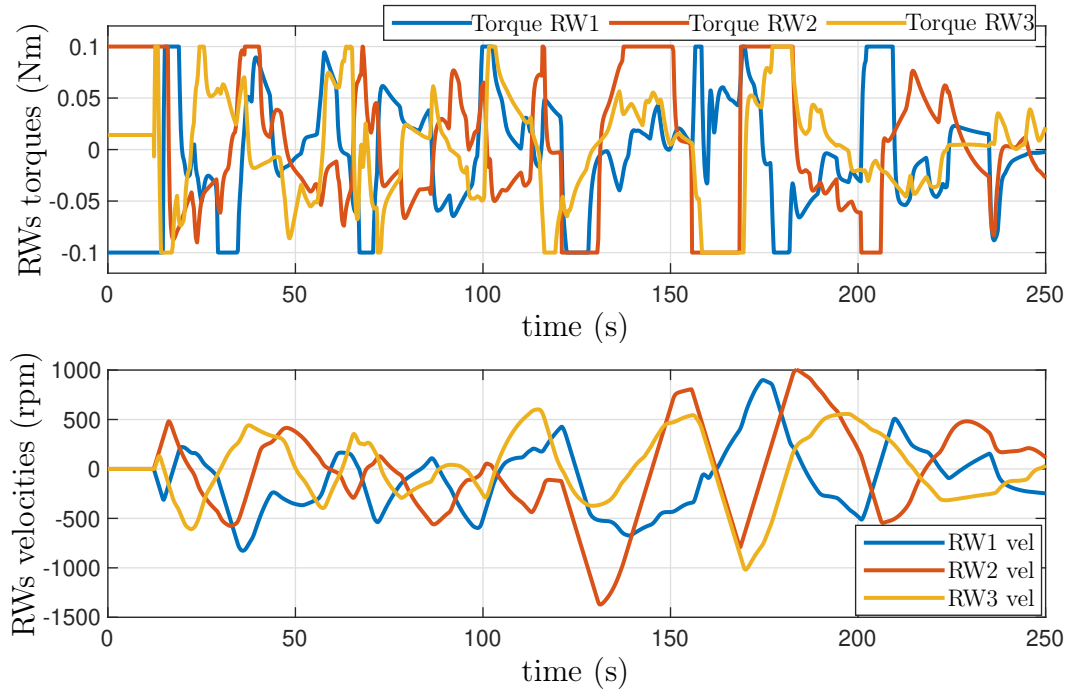


Figure 6.10: Client satellite RWs torques (top), and velocities (bottom) over time, obtained from the HIL experiment.

7 | Discussion and conclusion

7.1. Main contributions

This thesis proves the effectiveness of a novel control formulation for two orbital vehicles, each actuated by a set of thrusters and reaction wheels. In particular, the proposed dynamics enables the control of the motion of both agents coordinately, allowing them to achieve a wide range of configurations. This concept is particularly suitable for the context of On-Orbit Servicing, which is based on proximity interactions.

Hence, the contribution of this work is manifold. Firstly, the absolute dynamics of an actuated satellite is redesigned by applying the principles of multibody dynamics, eventually revealing a block-diagonalized inertia matrix. To accomplish this, a passive decomposition approach is applied to a multibody system consisting of a spacecraft and its RWs. As exposed in [27], the dynamics of the two distinct rigid bodies are redefined as a total motion, i.e. the locked system, and a relative motion, i.e. the shape system. This concept was applied in [29] to a spacecraft equipped with a robotic arm for grasping operations. In this thesis, the problem is reinterpreted as follows: the angular velocity of the multibody system is rewritten as a locked velocity, exploiting the total momentum formulation, while the shape dynamics is represented by the set of rotors.

Secondly, the passive decomposition method is exploited in the scenario involving two multibody systems. This allowed the achievement of an effective formulation of their relative motion. Particularly, the inertia couplings are entirely canceled, ultimately removing the need for acceleration measurements of the spacecraft.

Thirdly, three types of control laws are designed to achieve Lyapunov asymptotic stability. The first considers the systems as underactuated (or free-floating), hence capable of providing only internal forces through its RWs. This conveys stability only in the absence of initial momentum, which does not hold for a real scenario. Therefore, the free-flying and hierarchical control definitions are proposed, integrating both RWs and thrusters for actuation. The former is more time-effective, while the latter is oriented toward accuracy and fuel conservation. Moreover, all the presented controllers incorporate an inertia-shaping

approach that effectively increases the RWs torque contribution.

Lastly, the benefits of these mathematical representations are demonstrated through HIL experiments. Specifically, this approach allows for the testing of mission-like parameters such as significant velocities and dimensions, synchronizing the hardware experiment with a comprehensive visualization in software. The former showed the relative motion, and the latter their total dynamics. This concept was tested through an experiment simulating the approach phase between two 300 kg multibody satellites, simultaneously spinning at a high constant rate around one principal axis. The achieved physical consistency is rarely experienced in HIL experiments. Hence, the obtained results proved a pivotal importance toward on-ground validation of space robotic systems.

However, this formulation requires the integration of two complementary dynamics at the same time. Hence, the simulator must be equipped with a real-time computer able to sustain the requisites of computational power. Nonetheless, the requirements were reduced with respect to the relative dynamics model previously integrated on the OOS-SIM [1].

Furthermore, the enhanced performance of the proposed coordinated controller comes with trade-offs. Since the dynamics describes the motion of multiple systems, there is an increased level of mathematical complexity involved in its stability analysis. Moreover, potential measurement errors as well as actuation and sensor delays would propagate through the numerous couplings within the systems, compromising the overall accuracy. Thus, implementing this controller in a mission scenario would require the integration of failure detection and recovery systems.

Additionally, the work is based on some assumptions. For instance, the spacecraft base is modeled as a rigid body, which is commonly accepted in the robotics community. Also, the RWs dynamics does not consider any frictions, which normally reduce their torque contribution and are potentially detrimental toward the precision of the control, if not compensated correctly. Moreover, both the spacecraft's internal disturbances, such as vibrations, fuel sloshing and various uncertainties, and the numerous small LEO external torques are neglected. Lastly, the actual discretized dynamics of the thrusters is considered only numerically, by exploiting a black-box model in use at DLR. Hence, they are not included in the mathematical definition of the multibody. Particularly, the control accuracy is highly dependent on this model. Hence, it should be noted that, in the case of very stringent error-range values for precise docking operations, a different set of thrusters should be employed. Noticeably, actuators capable of generating a lower minimum torque for guiding the robot's motion with higher accuracy should be modeled.

Nevertheless, it is safe to assert that these assumptions simplify the analysis without

altering the validity of the proposed work.

Finally, some considerations can be made regarding the fact that two interacting satellites are just one example among the many binary systems found in the solar system. For instance, duality is fairly common among planets, stars, and asteroids. Even interstellar traveling spacecraft come in pairs: NASA's Voyager 1 and 2. Among these examples, the dynamics of asteroid pairs have often been analyzed using geometric mechanics, under the rigid body assumption, as in [40] - [41]. Hence, the proposed formulation is helpful for describing their dynamical evolution before the effects causing their possible escape arise.

7.2. Future work and research areas

Further development could involve relaxing the assumptions utilized during the work, to enrich it with some of the complexity that space missions hold. However, it may be more appealing to focus on research areas that align with the concepts presented in this letter.

In order to create a full HIL-efficient dynamics that covers all the simulations performed on the OOS-SIM, the proposed representations need the integration of the robotic arm dynamics. Particularly, the current dynamics formulation already involves two multibody systems in the loop. However, the servicer satellite kinematic chain is not included. This further step would allow for the simulation of grasping maneuvers, leading to a comprehensive improvement with respect to the formulation proposed in [1], currently employed on the DLR's facility. Noticeably, this integration would substantially increase the mathematical complexity of the dynamics. Moreover, the major difficulty can be identified in the fact that the servicer inertia matrix becomes a function of the arm configuration.

In addition, the detailed passive decomposition approach can be exploited to control Astrobees in a coordinated fashion. In fact, these robots not only provide a 0-g testing environment but also assist astronauts in performing chores, such as simple maintenance and monitoring tasks. For this purpose, they often operate in a group, representing an ideal scenario to investigate the performance of the proposed control and compare it with the currently employed approaches.

Furthermore, as exposed in section 5.5, the developed control can be easily extended to an indefinite number of bodies for centralized flight formations where a master system guides the group. Evidently, in the case of aerial vehicles such as drones, external forces as gravity and aerodynamic drag must be integrated into the dynamics model.

In conclusion, even fixed-based robots could benefit from this formulation. For instance, robotic arms that operate synchronized tasks, such as manipulation and assembly, could be controlled by imposing the required trajectory to the Cartesian space of the master system and commanding the other robots' relative motions with respect to it. Noticeably, inverse kinematics complexities would enrich this research topic.

Bibliography

- [1] M. De Stefano, H. Mishra, A. M. Giordano, R. Lampariello, and C. Ott, “A relative dynamics formulation for hardware- in-the-loop simulation of on-orbit robotic missions,” *IEEE Robotics and Automation Letters*, 2021.
- [2] D. J. Kessler and B. G. Cour-Palais, “Collision frequency of artificial satellites: The creation of a debris belt,” *Journal of Geophysical Research: Space Physics*, 1978.
- [3] NASA, “On-orbit satellite servicing study,” *Project Report - Goddard Space Flight Center*, Oct. 2010.
- [4] M. G. Bualat, T. Smith, E. E. Smith, T. Fong, and D. Wheeler, “Astrobe: A new tool for iss operations,” *2018 SpaceOps Conference*, 2018.
- [5] A. Flores-Abad, O. Ma, K. Pham, and S. Ulrich, “A review of space robotics technologies for on-orbit servicing,” *Progress in aerospace sciences*, 2014.
- [6] R. G. Reid, L. Roveda, I. A. Nesnas, and M. Pavone, “Contact dynamics of internally-actuated platforms for the exploration of small solar system bodies,” *International Symposium on Artificial Intelligence, Robotics and Automation in Space (i-SAIRAS)*, 2014.
- [7] H.-E. Park, S.-Y. Park, S.-W. Kim, and C. Park, “Integrated orbit and attitude hardware-in-the-loop simulations for autonomous satellite formation flying,” *Advances in Space Research*, 2013.
- [8] D. P. Scharf and P. R. Lawson, “Tpf-i technology milestone n.2 report: Formation control performance demonstration,” *JPL Publication*, 2008.
- [9] J. Scharnagl and K. Schilling, “New hardware-in-the-loop testing concept for small satellite formation control based on mobile robot platforms,” *IFAC-PapersOnLine*, 2016.
- [10] M. Wilde, B. Kaplinger, T. Go, H. Gutierrez, and D. Kirk, “Orion: A simulation environment for spacecraft formation flight, capture, and orbital robotics,” *2016 IEEE Aerospace Conference*, 2016.

- [11] M. Zwick, I. Huertas, L. Gerdes, and G. Ortega, “Orgl–esa’s test facility for approach and contact operations in orbital and planetary environments,” *International Symposium on Artificial Intelligence, Robotics and Automation in Space (i-SAIRAS)*, 2018.
- [12] C. Cruzen, R. Dabney, and J. Lomas, “Test results for the automated rendezvous and capture system,” *Guidance and Control Conference*, 1999.
- [13] R. Bell, J. Collins, J. Wertz, and L. J. Hansen, “Hardware-in-the loop tests of an autonomous gn&tc system for on-orbit servicing,” *AIAA Space 2003 Conference & Exposition*, 2003.
- [14] C. Carignan, N. Scott, and S. Roderick, “Hardware-in-the-loop simulation of satellite capture on a ground-based robotic testbed,” *International Symposium on Artificial Intelligence, Robotics and Automation in Space (i-SAIRAS)*, 2014.
- [15] C. D’Souza, Z. Milenkovich, Z. Wilson, D. Huich, J. R. Bendle, and A. Kibler, “The space operations simulation center (sosc) and closed-loop hardware testing for orion rendezvous system design,” *AIAA Guidance, Navigation, and Control Conference*, 2012.
- [16] V. Muralidharan, M. R. Makhdoomi, K. R. Barad, L. M. Amaya-Mejía, K. C. Howell, C. Martinez, and M. Olivares-Mendez, “Rendezvous in cislunar halo orbits: Hardware-in-the-loop simulation with coupled orbit and attitude dynamics,” *Acta Astronautica*, 2023.
- [17] T. H. Park, J. Bosse, and S. D’Amico, “Robotic testbed for rendezvous and optical navigation: Multi-source calibration and machine learning use cases,” *arXiv:2108.05529*, 2021.
- [18] O. Ma, A. Flores-Abad, and T. Boge, “Use of industrial robots for hardware-in-the-loop simulation of satellite rendezvous and docking,” *Acta Astronautica*, 2012.
- [19] H. Benninghoff, F. Rems, E.-A. Risze, P. Irmisch, I. Ernst, B. Brunner, M. Stelzer, R. Lampariello, R. Krenn, M. Reiner *et al.*, “Ricados-rendezvous, inspection, capturing and detumbling by orbital servicing,” *7th International Conference on Astrodynamics Tools and Techniques (ICATT)*, 2018.
- [20] M. De Stefano, R. Balachandran, and C. Secchi, “A passivity-based approach for simulating satellite dynamics with robots: Discrete-time integration and time-delay compensation,” *IEEE Transactions on Robotics*, 2020.
- [21] J. Artigas, M. De Stefano, W. Rackl, R. Lampariello, B. Brunner, W. Bertleff,

- R. Burger, O. Porges, A. Giordano, C. Borst *et al.*, “The oos-sim: An on-ground simulation facility for on-orbit servicing robotic operations,” *2015 IEEE International Conference on Robotics and Automation (ICRA)*, 2015.
- [22] R. Lampariello, H. Mishra, N. Oumer, P. Schmidt, M. De Stefano, and A. Albu-Schäffer, “Tracking control for the grasping of a tumbling satellite with a free-floating robot,” *IEEE Robotics and Automation Letters*, 2018.
- [23] J. Artigas, R. Balachandran, M. De Stefano, M. Panzirsch, R. Lampariello, A. Albu-Schaeffer, J. Harder, and J. Letschnik, “Teleoperation for on-orbit servicing missions through the astra geostationary satellite,” *2016 IEEE Aerospace Conference*, 2016.
- [24] F. Aghili and M. Namvar, “Scaling inertia properties of a manipulator payload for 0-g emulation of spacecraft,” *The International Journal of Robotics Research*, 2009.
- [25] R. Takahashi, H. Ise, A. Konno, M. Uchiyama, and D. Sato, “Hybrid simulation of a dual-arm space robot colliding with a floating object,” *2008 IEEE International Conference on Robotics and Automation*, 2008.
- [26] A. Ogundele, B. Fernandez, J. Virgili-Llop, and M. Romano, “A tip-tilt hardware-in-the-loop air-bearing test bed with physical emulation of the relative orbital dynamics,” *Adv Astronaut Sci*, 2019.
- [27] D. Lee and P. Y. Li, “Passive decomposition approach to formation and maneuver control of multiple rigid bodies,” *Journal of Dynamic Systems Measurement and Control-transactions of The Asme*, 2007.
- [28] G. Garofalo, B. Henze, J. Englsberger, and C. Ott, “On the inertially decoupled structure of the floating base robot dynamics,” *IFAC-PapersOnLine*, 2015.
- [29] H. Mishra, A. M. Giordano, M. De Stefano, R. Lampariello, and C. Ott, “Inertia-decoupled equations for hardware-in-the-loop simulation of an orbital robot with external forces,” *IEEE/RSJ International Conference on Intelligent Robots and Systems (IROS)*, 2020.
- [30] J. Kim, “Lie group formulation of articulated rigid body dynamics,” *Carnegie Mellon University*, 2012.
- [31] F. Bullo and R. M. Murray, “Tracking for fully actuated mechanical systems: a geometric framework,” *Automatica*, 1999.
- [32] M. Macdonald and V. Badescu, *The international handbook of space technology*. Springer, 2014.

- [33] R. J. Caverly, S. Di Cairano, and A. Weiss, “On-off quantization of an mpc policy for coupled station keeping, attitude control, and momentum management of geo satellites,” *IEEE European Control Conference (ECC)*, 2018.
- [34] A. Rahimi, “Chapter 9 - controlling satellites with reaction wheels,” in *Learning Control*, D. Zhang and B. Wei, Eds. Elsevier, 2021.
- [35] A. Dietrich, X. Wu, K. Bussmann, M. Harder, M. Iskandar, J. Englsberger, C. Ott, and A. Albu-Schäffer, “Practical consequences of inertia shaping for interaction and tracking in robot control,” *Control Engineering Practice*, 2021.
- [36] A. Albu-Schäffer, C. Ott, and G. Hirzinger, “A unified passivity-based control framework for position, torque and impedance control of flexible joint robots,” *The international journal of robotics research*, 2007.
- [37] D. Lee and P. Y. Li, “Passive decomposition of mechanical systems with coordination requirement,” *IEEE Transactions on Automatic Control*, 2013.
- [38] H. Mishra, M. De Stefano, A. M. Giordano, R. Lampariello, and C. Ott, “A geometric controller for fully-actuated robotic capture of a tumbling target,” *2020 American Control Conference (ACC)*, 2020.
- [39] S. Fahmi and T. Hulin, “Inertial properties in haptic devices: Non-linear inertia shaping vs. force feedforward,” *IFAC-PapersOnLine*, 2018.
- [40] H. Cendra and J. E. Marsden, “Geometric mechanics and the dynamics of asteroid pairs,” *Dynamical Systems*, 2005.
- [41] D. Scheeres, “Stability of binary asteroids,” *Icarus*, 2002.

A | Appendix

A.1. Stability of linear systems

Consider a linear time-invariant (LTI) system of the form: $\dot{x} = Ax$, with $x(0) = x_0$:

- the system is said to be stable if all the eigenvalues Λ_i of the stability matrix A lie in the left half of the complex plane. Since $\Lambda_i = \alpha_i + i\beta_i$, the stability condition can be written as $\alpha_i \leq 0$;
- the system is said to be asymptotically stable if all the eigenvalues of A have strictly negative real part: $\alpha_i < 0$.

A system of the form $\dot{x} = Ax + Bu$, $y = Cx + Du$ is said to be BIBO stable iff, for every bounded input of the system, its step response is bounded. In a closed-loop continuous-time case, it is verified if all the poles of the transfer function have strictly negative real parts.

A.2. Stability of non-linear systems

In the case of non-linear systems, stability can be assessed through the Lyapunov method. It has to be remarked that stability does not imply convergence. Thus, a clear distinction between Lyapunov stability and asymptotic stability has to be made.

Considering a non-linear mechanical system: $\dot{x} = f(x(t))$, with $x(0) = x_0$ and an equilibrium point \bar{x} such that $f(\bar{x}) = 0$:

- The equilibrium is said to be locally Lyapunov stable, if solutions starting at a finite distance δ from the equilibrium remain sufficiently close to the equilibrium forever, i.e. within a second finite boundary ϵ . This has to be true for every positive value of ϵ .
 - Mathematically, $\forall \epsilon > 0, \exists \delta > 0 : \text{if } \|x_0 - \bar{x}\| < \delta \implies \|x(t) - \bar{x}\| < \epsilon, \forall t \geq 0$;
 - This means that it must be possible to arbitrarily bound the solution in the

neighbourhood of \bar{x} by suitably bounding the perturbation.

- The equilibrium is said to be locally asymptotically stable if it is stable in the sense of Lyapunov, and the solution converges to \bar{x} for initial conditions x_0 sufficiently close to the equilibrium.
 - Mathematically, $\exists \beta > 0 : \|x_0 - \bar{x}\| < \beta \implies \lim_{t \rightarrow \infty} \|x(t) - \bar{x}\| = 0$;
 - It can be said that x_0 must belong to the spherical neighborhood of \bar{x} of radius β , also called basin of attraction.
- The equilibrium is said to be locally exponentially stable if solutions starting at a finite distance ϵ from the equilibrium, converge to it with at least exponential speed.
 - Mathematically, $\exists \epsilon > 0 : \|x_0 - \bar{x}\| < \epsilon \implies \|x(t) - \bar{x}\| \leq Ce^{-\alpha t}, \forall t > 0$, with C and exponential convergence rate $\alpha > 0$.
 - Exponential stability implies asymptotic stability, not vice-versa.
- Local asymptotic and exponential stability are global when the domain of attraction coincides with \mathbb{R}^n , i.e. they are valid for any initial state of the system.
- The equilibrium is unstable if it is not stable in the sense of Lyapunov.

A.3. Lyapunov stability through functional analysis

The stability of a non-linear system can be assessed mathematically through Lyapunov's direct method. In particular, considering the system $\dot{x} = f(x)$, with $f(x)$ continuous, and the region \mathbb{B} around the origin, composed of real values, it is necessary to define a continuously-differentiable function $w(x)$, called Lyapunov function.

In order to declare the stability of the system that is being analyzed, its Lyapunov function has to meet the following conditions:

1. $w(x) > 0, \forall x \in \mathbb{B} \setminus \{0\}$
2. $\underline{A} < w(x) < \overline{A}$
3. $\dot{w}(x) = \frac{\partial V}{\partial x} f(x) \leq 0, \forall x \in \mathbb{B} \setminus \{0\}$

In particular, the second condition verifies the presence of a lower and an upper bound for the function, considering \underline{A} and \overline{A} as positive values.

The Lyapunov function of a system is not unique and can be arbitrarily chosen: often the total energy of the system is a good candidate for mechanical systems and can be written as the sum of the kinetic energy and the potential energy of the error.

Finally, the system is locally asymptotically stable if it is stable in the sense of Lyapunov, and the derivative of the Lyapunov function is negative definite: $\dot{w}(x) = \frac{\partial V}{\partial x} f(x) < 0, \forall x \in \mathbb{B} \setminus \{0\}$. Indeed, if a system loses energy in time, yielding $\dot{w}(x) < 0$, the state eventually stops at the origin, verifying the convergence stated by the asymptotic stability.

A.4. LaSalle's invariance principle

LaSalle's principle is useful to perform a deeper analysis on the stability of a system, in cases in which the chosen Lyapunov function is only negative semi-definite. Indeed, the invariant set theorem says that, considering a system $\dot{x} = f(x)$, whose L. function is $w(x) : \dot{w}(x) \leq 0$ in a bounded region Ω_a , and defining P as the set of points of Ω_a where $\dot{w} = 0$, then, any trajectory of the system that starts in Ω_a tends asymptotically to M, the largest invariant set contained in P.

Moreover, the corollary of the theorem states that a system is asymptotically stable if its L. function is positive definite, its derivative is negative semi-definite, and the subset where $\dot{w}(x) = 0$ consists of the equilibrium point $x = \bar{x}$ only. The latter concept can be equally rephrased as, the only system trajectory for which $\dot{w}(x) = 0$ is the equilibrium trajectory.

However, invariant set theorems only apply to time-invariant systems. Therefore, the Barbalat Lemma is introduced for time-varying systems. In particular, it implies that if the Lyapunov function $w(x, t)$ is lower bounded, and its derivative $\dot{w}(x)$ is negative semi-definite and uniformly continuous (or $\ddot{w}(x)$ is bounded), then $\dot{w}(x)$ converges to zero along the trajectories of the system.

A.5. Application of LaSalle

It is now possible to apply the previous concepts and study the asymptotic stability of the 1 dof example, whose positive definite L. function is $w(x) = \frac{1}{2}mv^2 + \frac{1}{2}K\Delta x^2$. The set of points for which $\dot{w}(x) = -Dv^2 = 0$ are defined by a velocity that tends to zero. Consequently, the dynamic equation of the system $m\dot{v} = -K\Delta x - Dv$, leads to the unique solution $\Delta x = 0$. Hence, the subset M in P consists only of the equilibrium point, and the system is asymptotically stable.

A.6. Energy conservation and skew-symmetry proof of $\dot{M} - 2C$

Considering the system's equation of motion in the form $M(q)\ddot{q} + C(q, \dot{q})\dot{q} = \tau$, it is possible to define the Lyapunov function candidate of the robot as the total energy:

$$w(x) = \frac{1}{2}\dot{q}^T M(q)\dot{q} + U(q)$$

Hence, its derivative is:

$$\begin{aligned}\dot{w}(x) &= \dot{q}^T M \ddot{q} + \frac{1}{2} \dot{q}^T M \dot{M} \dot{q} + \frac{\partial U}{\partial q} \dot{q} \\ &= \dot{q}^T (\tau - C \dot{q}) + \frac{1}{2} \dot{q}^T \dot{M} \dot{q} \\ &= \dot{q}^T \tau + \frac{1}{2} \dot{q}^T (\dot{M} - 2C) \dot{q}\end{aligned}$$

Taking into account the condition where $N(q, \dot{q}) = \dot{M} - 2C$ demonstrates skew-symmetry ($N^T = -N$), it can be demonstrated that for any $(n \times 1)$ vector ω , the equation $\omega^T N(q, \dot{q}) \omega = 0$ is verified. This observation becomes particularly significant when ω is set equal to \dot{q} :

$$\dot{q}^T N(q, \dot{q}) \dot{q} = 0$$

. The principle of the conservation of the total energy of the system can be then exploited to demonstrate the previous statement. In fact, in case of the absence of non-conservative generalized forces, $\tau = 0$, the value of the total energy does not vary in time and the derivative of the total energy must be null, $\dot{w}(x) = 0$. This condition is verified only in the case of skew-symmetry of $\dot{M} - 2C$, which is hence proved.

List of Abbreviations

0-g	zero-gravity
CoM	Center of Mass
CC	Centrifugal/Coriolis
DLR	German Aerospace Center
dof	Degrees of Freedom
e.g.	<i>exempli gratia</i> (for example)
EoM	Equations of Motion
FF	Force Feedforward
FTS	Force-Torque Sensor
GN&C	Guidance Navigation and Control
HIL	Hardware-in-the-Loop
i.e.	<i>id est</i> (that is)
IS	Inertia Shaping
ISS	International Space Station
LEO	Low Earth Orbit
MoI	Moment of Inertia
OOS	On-Orbit Servicing
OOS-SIM	On-Orbit Servicing Simulator
RWs	Reaction Wheels

List of Symbols

- A Mapping Matrix for the RWs
- C Centrifugal/Coriolis Matrix
- F Force-Torque Vector
- f Force
- τ Torque
- g Transformation Matrix
- H Generalized Momentum
- I Inertia
- K_d Derivative Gain
- K_p Proportional Gain
- M Inertia Matrix
- m Mass
- p Position
- R Rotation Matrix
- V Generalized Velocity
- v Linear Velocity
- ω Angular Velocity
- W Lyapunov Function

List of Figures

1.1	ESA ClearSpace-1 robotic mission render (<i>Credits</i> : ClearSpace).	2
1.2	The Astrobee system concept (<i>Credits</i> : NASA).	3
2.1	EPOS 2.0 robotic facility (<i>Credits</i> : DLR).	7
2.2	OOS-SIM robotic facility (<i>Credits</i> : DLR RMC).	8
3.1	Transformation of a rigid body's velocity in different reference frames.	12
3.2	Conservation of the momentum in the inertial frame (left) and of the kinetic energy (right), over time.	17
3.3	Hydrazine thruster 8 – 25 N (<i>Credits</i> : ArianeGroup).	26
3.4	RWs main configurations	28
3.5	Client satellite on the left and servicer satellite, with the RW model implemented, on the right.	29
3.6	Servicer satellite translational errors over time.	31
3.7	Servicer satellite ideal and actuated forces, during the docking maneuver.	32
3.8	Servicer satellite rotational errors over time.	32
3.9	Velocities of the RWs during the docking maneuver.	32
4.1	Multibody system's Lyapunov function over time.	37
4.2	Free-floating control results: RWs torques (a), RWs velocities (b), and rotational error (c).	39
4.3	Free-floating control results with inertia shaping: RWs torques (a), RWs velocities (b), and rotational error (c).	41
4.4	Free-flying control results: RWs torques (a), RWs velocities (b), rotational error (c), and ideal torques vs torques actuated by the thrusters model (d).	43
4.5	Hierarchical control results: RWs torques (a), RWs velocities (b), rotational error (c), and ideal torques vs torques actuated by the thrusters model (d).	45
4.6	Average fuel mass consumed by a thruster in hierarchical and free-flying operational modes.	47

5.1	Relative control results in continuous time (free-flying case): rotational error (a), translational error (b), and continuos-time control forces and torques (c).	59
5.2	Relative control results in continuous time (free-flying case): RWs torques (a), and velocities (b).	60
5.3	Flight formation between multiple fixed-inertia multibody satellites.	61
6.1	CoppeliaSim simulation environment synchronized with the HIL experiment, showing the client satellite.	64
6.2	Rotational (top) and translational (bottom) errors over time, obtained from the HIL experiment.	65
6.3	Total momentum over time, obtained from the HIL experiment.	65
6.4	Forces ideal (a), actuated by the thrusters (b), and external (c) over time, obtained from the HIL experiment.	66
6.5	RWs torques (top), and velocities (bottom) over time, obtained from the HIL experiment.	67
6.6	The relative motion replicated on the DLR OOS-SIM on the left, and the absolute motion shown in software on the right.	68
6.7	Client satellite forces: ideal (a), actuated by the thrusters (b), and external (c) over time, obtained from the HIL experiment.	71
6.8	Total momentum (a), relative momentum (b), and kinetic energy (c) over time, obtained from the HIL experiment.	72
6.9	Relative rotational (top) and translational (bottom) errors over time, obtained from the HIL experiment.	73
6.10	Client satellite RWs torques (top), and velocities (bottom) over time, obtained from the HIL experiment.	73

List of Tables

3.1 Thrusters model parameters.	27
3.2 Reaction wheels model parameters (<i>Credits: Astrofein</i>).	29

Acknowledgements

I would like to thank Prof. Francesco Braghin for supporting me with complete availability and interest throughout the development of this thesis.

Moreover, I would like to express my gratitude to the German Aerospace Center (DLR) and the community of its Robotics and Mechatronics Center for providing me the opportunity to work on advanced topics, with cutting-edge facilities, and alongside many bright individuals.

Therefore, I wish to thank the OOS-SIM team, especially Dr. Marco De Stefano, Dr. Roberto Lampariello, and Dr. Ribin Balachandran, for sharing their knowledge and passion for their work with me.

A special mention goes to Hrishik Mishra, who mentored and supervised me thoroughly during the months of research. Thank you for sharing your enthusiasm for impactful research and your precious advice. Each discussion led to many new ideas and routes to explore. Also, thanks for keeping the spirit up during the countless adjoints calculations and debugging sessions (L&N is no walk in the park).

Furthermore, I am grateful to my friends, with whom I have shared the best memories for over ten years. I also wish to thank the fellows I met during my university path for being great journey buddies, and the universities I attended, which have shaped a significant part of my character.

Finally, I express my deepest gratitude to my family for wholeheartedly supporting me, encouraging critical thinking, and consistently placing their trust in me.